Medical Isotope Production of Actinium-225 By Linear Accelerator Photon Irradiation of Radium-226

Paul D. VanSant

Thesis submitted to the faculty of the Virginia Polytechnic Institute and State University in partial fulfillment of the requirements for the degree of

Master of Science
In
Mechanical Engineering

Mark A. Pierson - Chair
Alireza Haghighat
Timothy A. Policke

April 30, 2013
Blacksburg, VA

Keywords: Radium-226, Actinium-225, Medical Isotopes, Linear Accelerator (LINAC), Photonuclear Cross-section

Medical Isotope Production of Actinium-225 By Linear Accelerator Photon Irradiation of Radium-226

Paul D. VanSant

Abstract

There is a present and future need for the medical isotope Actinium-225, currently in short supply worldwide. Only a couple manufacturers produce it in very low quantities. In roughly the past 10 years the medical community has explored the use of Ac-225 and its daughter Bismuth-213 for targeting a number of differing cancers by way of Targeted Alpha Therapy (TAT). This method utilizes the alpha-decay of both Ac-225 (half-life 10 days) and Bi-213 (half-life 46 min) to kill cancerous cells on a localized basis. Maximum energy is delivered to the cancer cells thereby greatly minimizing healthy tissue damage.

This research proposes a production method using a high-energy photon spectrum (generated by a linear accelerator or LINAC) to irradiate a sample of Radium-226 (half-life 1600yrs). The photo-neutron reaction liberates neutrons from Ra-226 atoms leaving behind Radium-225 (half-life 14.7 days). Ra-225 decays naturally through beta emission to Ac-225. Previous research demonstrated it is possible to produce Ac-225 using a LINAC; however, very low yields resulted which questioned the feasibility of this production method. This research proposes a number of LINAC and radium sample modifications that could be greatly increase yield amounts for practical use.

Additionally, photo-neutron cross-section data for Ra-226 was used, which led to improved yield calculations for Ra-225. A MATLAB® model was also created, which enables users to perform quick yield estimates given several key model parameter inputs. Obtaining a sufficient supply of radium material is also of critical importance to this research. Therefore information was gathered regarding availability and inventory of Radium-226. This production method would serve as a way to not only eliminate many hazardous radium sources destined for interim storage, but provide a substantial supply of Ac-225 for future cancer treatment.

Acknowledgements

I would first like to thank Virginia Tech for starting a nuclear program that was co-joined within the school of Mechanical Engineering, providing students the ability to study in this most important and interesting field of engineering. I was able to apply a select number of nuclear courses into the pursuit of a Masters in Mechanical Engineering, for a Nuclear Engineering Graduate Certificate. Most of all I would like to thank Dr. Pierson for providing several meaningful research topics from which to choose, and graciously allowing me to select one of interest to pursue. His extensive experience, knowledge, and expertise allowed for productive and helpful meetings that greatly assisted progress over these last several months of research. I would additionally like to thank my present employer The Babcock & Wilcox Co, as they were gracious enough to allow me to break away from the busy engineering projects there, and take on a full-time pursuit of a Master's degree, all the while holding my present position and supporting my efforts. For all of this I am grateful.

Dedications

Finally, I dedicate this work to my Mother and Father who always offered prayers, a haven of encouragement and a driving will to accomplish something more. To my loving wife Rebekah, who has been by my side through this entire endeavor; her prayers, support, and love have provided the additional motivation to complete this mission at hand.

Table of Contents

Table of Figures

List of Tables

Units & Conversions

Units & Conversions	
1 cm	10^4 μm
1 barn	10^{-24} cm^2
1 mb (millibarn)	10^{-27} cm^2
1 MeV	10^6 eV
1 eV (electron volt)	1.6022 x 10^{-19} J (Joules)
1 Ampere	1 Coulomb/s
1 electron charge	1.602x10^{-19} C (Coulombs)
1 R (Roentgen)	2.58 x 10^{-4} C/kg air [Exposure]
1 Ci (curie)	3.7 x 10^{10} disintegrations/s [*Activity*]
1 Bq (Becquerel)	1 dis/sec [*Activity*]
1 Gy (gray)	1 J/kg = 100 rad [*Absorbed Dose*]
1 Sv (Sievert)	100 rem (Roentgen equivalent man) [Dose equivalent]

1. Introduction

Production methods for Actinium-225 (Ac-225) have only recently been explored due to its high demand in cancer research and clinical trials using targeted alpha therapy. A report from Idaho National Lab (INL) mentions three facilities around the world that currently produce Ac-225 from a dwindling supply of Thorium-229 (Th-229). The remaining amount of Th-229 used in current production is speculated to be less than 2 grams. However, the amounts of Ac-225 produced are too small for any practical use, which greatly hinders the medical community in furthering their clinical trials. The level of work involved in obtaining Ac-225 by current methods is quite significant, therefore a more robust and effective method of production is needed. In 2006 a researcher (Melville) explored a new production method by way of linear accelerator that appears to be promising [1] [2] [3]. This research expands upon Melville's work in a number of key areas, adding a series of bounded production yield estimates based upon a physical model of Radium-226 cross-section data, and radium attenuation considerations. The fundamental principles governing this production method will first be covered, and will include a brief discussion of some background to Melville's work to set the stage for the research presented herein.

1.1. Fundamentals of Ac-225 Production Methods

Prior to covering the many aspects of this research, it is first important to discuss some fundamentals and key concepts supporting this work, and provide the motivation for it.

Linear accelerators or LINACs are used widely through the medical world in various forms of radiation therapy and imaging. Medical LINACs produce a high-energy spectrum of photon radiation which is of interest here. LINACs of mega-voltage potential produce a spectrum of photons by accelerating electrons to high energies, typically between 4 and 25 MV. A mono-energetic pulsed electron beam is formed that then strikes a target (usually tungsten), where the electrons interact with target nuclei giving up energy in the form of Bremsstrahlung or "breaking radiation". The photons in this Bremsstrahlung spectrum are distributed over the full range of energies from zero to the maximum electron beam energy, which for the LINAC analyzed herein is 18 MeV. A photon energy spectrum generally takes the form of a positively skewed distribution (Fig 7 and Fig 9). The peak photon rate in a

given LINAC Bremsstrahlung spectrum generally resides within the 1 to 2 MeV energy range. This skewed photon distribution is unfortunate because the vast majority of photons are below the 6.4 MeV single-neutron separation energy (or binding energy) needed for photo-neutron reactions with Ra-226. Photons are then incident upon a Ra-226 target, where there is a probability of photon interaction with a Ra-226 nucleus at a given energy, commonly referred to as the material's photo-neutron cross-section.

There are a number of ways to produce Ac-225. However the paths leading to its production are all man-made in some way. It is created in the decay chain of U-233 (Fig 1), where in nuclear reactors Thorium-232 (Th-232) is bombarded with neutrons producing Uranium-233 (U-233) [4] [5]. It can also be produced in cyclotrons by direct proton bombardment of Ra-226, thereby kicking off two-neutrons and leaving Ac-225. The production method being explored in this research is by a photo-neutron reaction with Ra-226.

$$^{226}_{88}Ra + \gamma \rightarrow {}^{225}_{88}Ra + {}^{1}_{0}n \tag{1.1}$$

A photon of significant energy (>6.4 MeV) liberates a neutron from Ra-226 leaving a Ra-225 atom. Ra-225 then undergoes natural radioactive beta decay (half-life 14.9 days) to Ac-225.

$$^{225}_{88}Ra \rightarrow {}^{225}_{89}Ac + {}^{0}_{-1}e \tag{1.2}$$

This level of photon energy is commonly available with most medical LINACs used at hospitals and research labs for radiation treatment. This type of standard LINAC will most likely be used for preliminary experiments, as they are readily accessible. Initial experiments will demonstrate proof of concept and provide valuable feedback for the eventual design of a custom LINAC.

The inherent benefits of an alpha emitter are that it has a high linear energy transfer (LET) in most materials, thereby delivering nearly all the alpha particle's energy within a very short distance (approximately 35 – 55 microns), killing the targeted cancer cell (2 – 120 microns), see Table 6. This greatly reduces the surrounding healthy tissue damage, compared to present methods of radiation treatment that emit more penetrating and damaging forms of beta and gamma radiation. This is why Ac-225 and its daughter Bi-213 are well suited for targeting micro-metastatic disease (or cancers that spread) in addition to blood-

borne cancers like leukemia [4]. There is still much work being performed by the medical community in developing the best targeting agents (enzymes and antibodies) that would carry the medical isotopes to the desired cancer cells [6]. Clinical trials using Ac-225 and Bi-213 are underway for several types of cancer with much success in a number of patients [6], but the supply of Ac-225 is very small, greatly limiting research opportunities in this area.

Another reason why these isotopes are favorable for cancer therapy is that both have short, but not too short a half-life. This allows them to be manufactured, refined, and shipped on a reasonable time line. In addition, they ultimately decay to Bi-209 (stable) which is not harmful to the human body as it is found in Pepto-Bismol. Alpha particles given off by the Ac-225 decay chain, range in energy from 4 MeV to 7 MeV (Fig 1). Many current methods of cancer treatment use radiation therapy with a beam of photons directed at a particular area of the patient's body (typically a cancerous area or cancerous tumor). Medical LINACs have the flexibility to tailor a photon beam by flattening filters and computer controlled collimators, shaping it to the patient's tumor. This custom beam shaping technology greatly reduces radiation dose to the surrounding healthy tissue. However, targeted alpha therapy improves upon current radiation treatment methods by actively seeking out and destroying cancer on a cellular basis.

1.2. Background

The LINAC-based Actinium-225 production method was pursued by Melville from 2005 – 2007. His work was fully documented in his dissertation along with two published articles further detailing this work [1] [2] [3]. Yield calculations of Ac-225 were performed with photo-neutron cross-section data that approximated that of Ra-226. A theoretical yield model was also created in both MATLAB® and C++ to estimate the Ra-225 yields, using cross-section data for Bi-209 and Th-232 as a substitute for Ra-226. It was assumed that since the Bi-209 and Th-232 cross-section parameters were comparable, Ra-226 also would be, hence Bi-209 data was chosen for the calculations. The Bi-209 cross-section parameters were used with a particle resonance equation (see Chapter 4) on a per energy basis to generate an estimated photo-neutron cross-section curve. The yield was calculated using photon rate data provided by Varian (18 MeV LINAC used in Melville's experiments), with photo-neutron cross-section data for Bi-209. Both the photon rate and cross-section data are

energy dependent parameters, therefore convolution integration over the full photon energy range was used to calculate the Ra-225 yield.

Melville additionally explored the LINAC Bremsstrahlung efficiency at 18 MeV, and evaluated three different methods for obtaining Bremsstrahlung efficiency values at different photon energies. The high-energy approximation formula was chosen for use which provided an estimated efficiency for photon energies at 18 MeV and beyond, without surpassing 100% efficiency at higher energies, as several other methods demonstrated at lower energies.

Two irradiation experiments were also performed by Melville using radium needles once used for cancer treatment. A Varian 2100C 18 MeV medical LINAC was utilized for those experiments. The radium needles used were approximately 20 mCi and 15 mCi, or 20 mg and 15 mg, of Ra-226 respectively. A comparison was performed with both experiments to examine the difference between Ra-225 yields. First, a 40 mCi sample (two 20 mCi needles) was irradiated 49 cm below the tungsten LINAC target (below the flattening filter). The second irradiated a 15 mCi sample 12 cm below the tungsten LINAC target (above the flattening filter). The results showed that by simply moving the sample closer to the tungsten target, the Ra-225 yield increased from 64 µCi to 88 µCi. However, considering the difference in sample activity and the difference in irradiation times, there was actually a six-fold increase in the Ra-225 production rate by moving the sample closer, as will be discussed in more depth in chapter 7.

A High Purity Germanium (HPGe)-Spectrometer was used during each experiment to measure the count rate of each sample before and after irradiation to detect the gamma spectrum peaks of Ra-225 and Ac-225. Given the very small yields in each of Melville's experiments it was difficult to resolve prominent gamma peaks for Ac-225. However, a noticeable increase in the Ra-225 (40 keV) peak was observed over a number of weeks. The Ac-225 peaks were very difficult to distinguish, partially due to the high Ra-226 background (with its daughters), and also due to Ac-225 not having prominent peaks. Ac-225 has many peaks spread out over a number of energies. However if a higher yield was achieved, the 99.91, 150, and 188 keV peaks should be observable [2]. Without conducting chemical separation of Ac-225 from the Ra-226, there is significant uncertainty in the yield results from these experiments.

In an effort to increase yield to considerable amounts, the LINAC beam parameters could be modified. To evaluate this potential, Melville performed a yield calculation that incorporated a doubling in the average electron beam current, pulse frequency, and pulse length, (see section 7.1). These LINAC modifications would potentially lead to an 8-fold increase in yield. However, as Melville mentioned, the LINAC power would also need to be increased by 8 times to increase the average beam current [3]. Increasing the irradiation time is an additional factor to directly increase production amounts.

This research expands upon Melville's work, providing a series of yield calculations with best predictions of cross-section data for Ra-226, in addition to an alternative yield equation that accounts for photon attenuation in much thicker samples that would be used for actual production. This work also provided a Microsoft Excel and MATLAB® yield model and tool for follow-on researchers, to enable quick calculations of estimated Ra-225 and Ac-225 yields, given a set of LINAC and radium sample parameters. This allows for a parametric analysis to determine the best parameters to optimize the production yield in any given scenario.

1.3. Objectives

The first goal of this research was to create a Microsoft Excel and MATLAB® model and tool to provide yield calculations, by using photon spectrum data and Ra-226 cross-section data. A number of other key parameters for the LINAC and sample will be made adjustable within the model for quick analysis of differing scenarios. This will be done by creating a curve-fitting model within MATLAB® for fitting of the Bremsstrahlung photon spectrum and cross-section data. This model will provide future researchers a means to optimize yield estimates, given a set of photon spectrum data and sample characteristics.

The second goal was performing an attenuation study of both photon/sample interaction and alpha particle attenuation within body tissue. Understanding the attenuation characteristics of photons in a given radium sample will aid in optimizing sample dimensions and yield. Providing an understanding of alpha attenuation in matter will also show the effectiveness of targeted alpha therapy.

The third goal was providing background information on radium-226, its radiation characteristics, its availability, and source inventory estimates. The availability of Ra-226

material is necessary for future experiments in this area, not to mention a potential production-worthy radium supply if a viable method of production is established.

Finally, this research will present a path forward for other researchers with a number of future objectives to explore. A number of ideas are proposed herein for future confirmation experiments and design for a custom LINAC that can maximize Ac-225 production yield.

The ultimate goal was to provide sufficient information to form a business case analysis expressing the economic feasibility for pursuing this method of medical isotope production of Ac-225/Bi-213.

1.4. Types of Radiation

Alpha radiation—Alpha particles are heavy charged particles consisting of a stable helium nucleus. They are emitted through the natural decay of various isotopes, and typically are emitted by radioactive isotopes above Lead (Z>82). The track of an alpha particle through matter is mostly a straight path [7]. They lose their energy continuously along their path by many Coulomb force interactions with negatively charged particles in the surrounding material. Alphas give up the majority of their energy in the form of delta rays or high energy electrons. As the depth of penetration increases in a particular absorber, they give up an increasing amount of energy leading to sudden absorption within the surrounding material. The typical alpha particle energy emitted in radioactive decay is between 4 – 8 MeV, but can be stopped by a single sheet of paper, ranging in thickness from about 100 – 300 microns. Alphas do not pose a threat to humans externally, because the average epidermis (skin) layer is 0.5 mm. However when located within the body among living cells, it is easy to see how this amount of energy deposited in such a short distance would be advantageous in destroying specific cancer cells. This is the fundamental principle behind the use of Ac-225 and Bi-213.

Beta radiation—Beta particles are simply positive (positron) or negatively charged electrons, given off by certain radionuclides whose neutron to proton ratio is too high (β^- decay) or too low (β^+ decay). In the case of β^- decay, a neutron is converted to a proton accompanied by an electron which is emitted from the nucleus in a spectrum of energies. A beta particle can interact in matter by either coulomb forces or by radiative methods [7].

Compared to alpha particles, beta particles follow a much more random path and lose their energy over longer distances causing them to be more penetrating, and therefore more harmful to the body. Their radiative interactions in matter result in the emission of Bremsstrahlung radiation (see Section 2). This is the interaction within LINACs that make this production method possible. By imparting a mono-energetic beam of high-energy electrons onto a high-Z target material, Bremsstrahlung (photons) is produced. Beta particles exist over a broad range of energies but are typically derived from sources such as pure beta emitting isotopes or mono-energetic particle accelerators as will be utilized in this research.

Gamma radiation—Gamma rays are high energy photons emitted from atomic nuclei. They cover a broad energy range and interact in materials through three main mechanisms: photoelectric absorption (low energies), Compton scattering (medium energies), and pair production (high energies) [8]. These are not charged particles as discussed earlier and therefore do not slow down continuously by Coulomb interactions along their path. This allows them to travel much greater distances through matter. Their energy along with the atom density of material being traversed, will determine the range traveled in the absorber. Gamma rays are far more damaging to the human body, because they can penetrate deeply and cause a number of subsequent radiation effects by their interaction with the atoms of the body in undesirable locations. High-Z materials such as lead are more effective at stopping gammas due to having high atom densities.

1.5. Present Ac-225 Production Method

There are several ways of producing actinium-225 (Ac-225). Currently the most popular method is by separating minute amounts of Ac-225 from its parent Th-229, whose parent is U-233, see Figure 1.

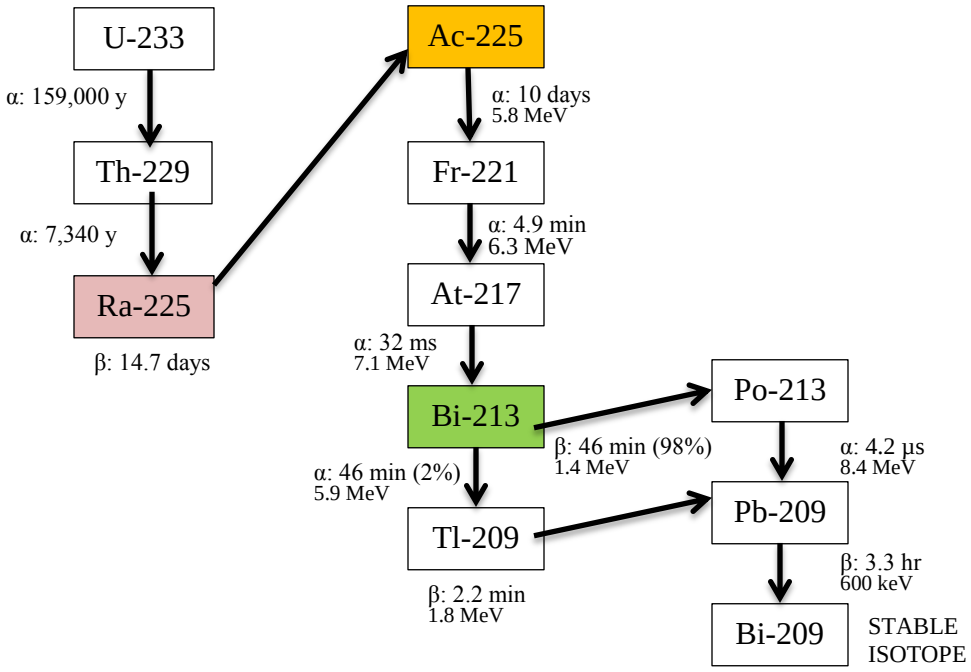

Figure 1 Decay Chain of U-233
Created with nuclide information from the Public Domain, NNDC **[9]**.

Over the years U-233 has been produced by a number of breeder and research reactors, such as those at Idaho National Lab (INL) and Oak Ridge National Lab (ORNL). The U-233 waste at these sites has decayed over time to produce small amounts of Ac-225. This leaves separation methods to yield an appreciable amount for use. Since the half-lives of U-233 and Th-229 are 159,000 years and 7340 years, respectively, it is easy to see how little Ac-225 would be extractable from Th-229. Nevertheless, this is the current primary method for producing Ac-225. Additionally, there was a design effort in the United States through the Department of Energy (DOE) and by INL to build a highly efficient separation system called Medical Actinium for Therapeutic Treatment (MATT) [4]. MATT was developed to resolve the growing need for Ac-225 within the United States by utilizing the aging stockpiles of U-233 at a number of labs as just discussed. MATT would separate the Ac-225 from many tons of U-233 source material, with the ability to separate Ac-225 at 1 part per 165 billion. The DOE estimates that roughly 140 g of parent Th-229 material is present between INL and ORNL locations. This equates to approximately 30 Ci of Ac-225 present in secular equilibrium with Th-229, or 0.52 mg of Ac-225 (see calculation below). The National Institutes of Health (NIH) estimated that by 2009 the worldwide demand for Ac-225 would

be 7,500 mCi, per year, with world production at less than 600 mCi per year [4]. However, if a large supply of Ac-225 became available, it is anticipated that the world demand would significantly increase above these predicted amounts. The MATT program estimates that their production capabilities will increase current world production rates by 100-150 times (60 – 90 Ci per year) at full capacity [4]. However, it is uncertain what the current funding and production status is of this program. As a comparative production quantity to another medical isotope in high demand, Molybdenum-99 (Mo-99) is projected to be produced at a rate of approximately 20 grams per year, which would account for more than half the US demand. Mo-99 (half-life 66 hrs) undergoes beta decay to the medical isotope Technetium-99m (Tc-99m), a metastable-state having a 6 hour half-life. If Ac-225 demand eventually reaches similar Mo-99 levels, more production capacity would be required. Under these conditions the LINAC production method may have the potential to provide a significant enough production rate to meet those demands.

2. LINAC-based Ac-225 Production Method

The production method being explored in this research involves the direct irradiation of Ra-226 via a LINAC. The LINAC provides a steady source of high-energy photons in the form of Bremsstrahlung (or breaking radiation). This is done by accelerating a mono-energetic beam of electrons through a series of wave-guides striking a metallic target (usually high-Z materials such as tungsten). As the electrons interact in the tungsten target, strong coulomb forces between the tungsten atom nuclei and electrons redirect their path, thereby giving up energy in the form of photons. These photons are emitted from the target in a full spectrum of energies ranging from zero to the maximum electron energy of the LINAC, such as 15 MeV or 18 MeV. As photons bombard a Ra-226 sample, all photons above 6.4 MeV (neutron-separation threshold energy E_s of Ra-226) have a probability of interacting to separate a single neutron from a radium nucleus. Once again the photonuclear reaction seen here ${}^{226}_{88}Ra + \gamma \rightarrow {}^{225}_{88}Ra + {}^{1}_{0}n$ demonstrates this. The neutron binding energy is given by [8]:

$$E_s = \left[m_n + m\left({}^{A-1}Z\right) - m\left({}^{A}Z\right)\right] \cdot 931.5\ MeV/amu \tag{2.1}$$

Where, m_n is the neutron mass in amu $m(^{A-1}Z)$ is the resultant Ra-225 atomic mass, and $m(^{A}Z)$ is the atomic mass of Ra-226.

Following a sufficient irradiation time of a radium sample, the Ra-225 produced beta decays following its 14.9 day half-life to Ac-225. At approximately 18 days following sample irradiation, Ac-225 (having built to its peak activity) would be ready for separation. The Ac-225 would be separated from all remaining Ra-226 and Ra-225, allowing the Ra-226 to be used again in future irradiation cycles. The Ac-225 would most likely be shipped to a medical facility in an Ac-Bi generator, where the Ac-225 could be used directly or Bi-213 could be eluted for use.

2.1. Linear Accelerator (LINAC) Details

To produce a beam of electrons, an electron gun emits a steady stream of electrons from a cathode into a drift tube, where they are attracted toward the anode at the other end of a long accelerator tube (Fig 2).

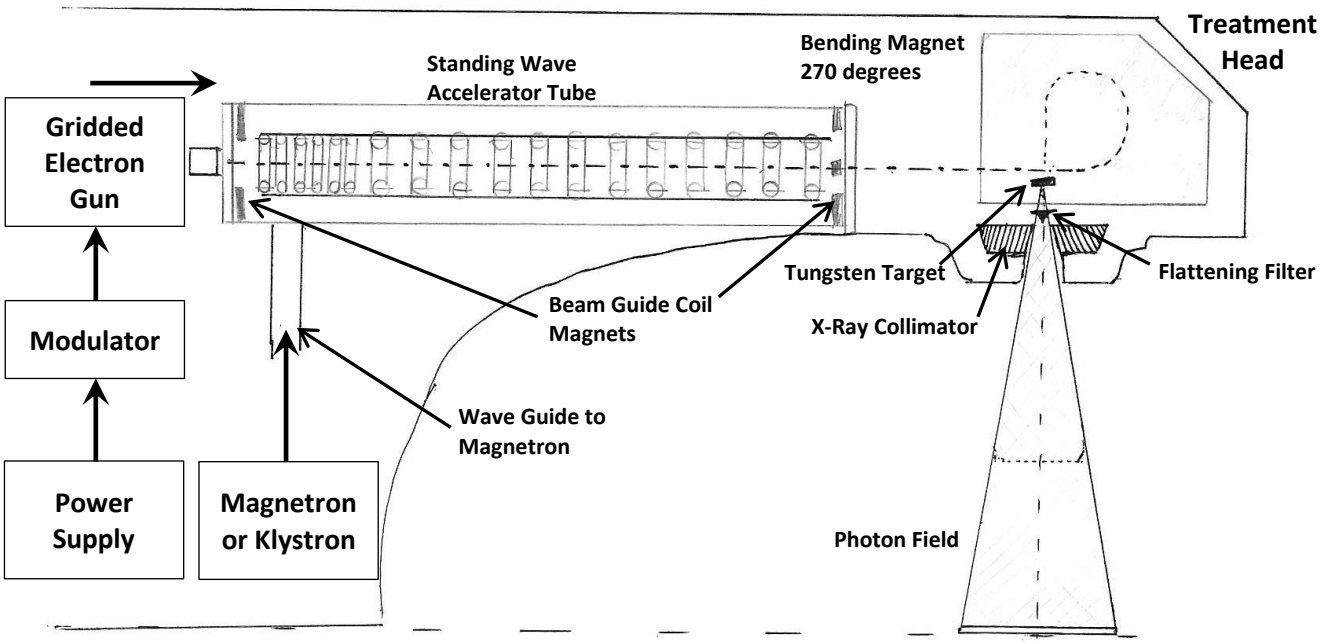

Figure 2 Typical Medical LINAC Schematic
Used for irradiation therapy, with all major components identified. Adapted from *(http://www.pedsoncologyeducation.com/RadiotherapyBasicsWhatisXRT.asp, 2008.)* [10].

The freed electrons then pass through a set of forming coil magnets guiding electrons down the long axis of the accelerator tube through a series of standing wave accelerator guides. The initial closely packed wave-guide cavities accelerate the electrons to relativistic speeds, leaving the remainder of the cavities to increase the electrons' effective mass to higher energies. A magnetron or klystron generates a RF frequency field used to accelerate the electrons down the central axis of the tube (Fig 2). As electrons travel along each wave formation, RF waves produce electron groups continually being accelerated through the full length of the accelerator tube. These groups of electrons constitute a pulse of current, and the frequency of pulses is controlled by the RF source. As the accelerated beam exits the tube an additional set of magnetic coils are used to maintain beam direction. The beam is generally re-directed 90° to strike a tungsten target for photon spectrum generation. This beam bending is performed by either a 270° set of parallel bending magnets or a series of three magnet pairs called slalom magnets. Both do a good job of redirecting and refocusing the electron beam before it strikes the tungsten target in the treatment head (Fig 2). However, if a custom LINAC were built for this production method, a tungsten target could simply be placed in-line with the electron beam, to greatly simplify design and cost. More information on election beams and their characteristics can be obtained from the following source [11]. As the beam strikes the high-Z material (usually tungsten or tantalum) Bremsstrahlung radiation is generated in the form of a photon spectrum. Medical LINACs have a series of parts located at the photon beam output that shape (Fig. 3), and attenuate the photon spectrum for precision radiation therapy as discussed earlier. This research is not concerned with precision beam shaping, but rather to have as many high energy photons as possible delivered to a given radium sample. Therefore, when a production LINAC is built for this task, much simplicity can be maintained in the LINAC head design by removal of collimators and bending magnets.

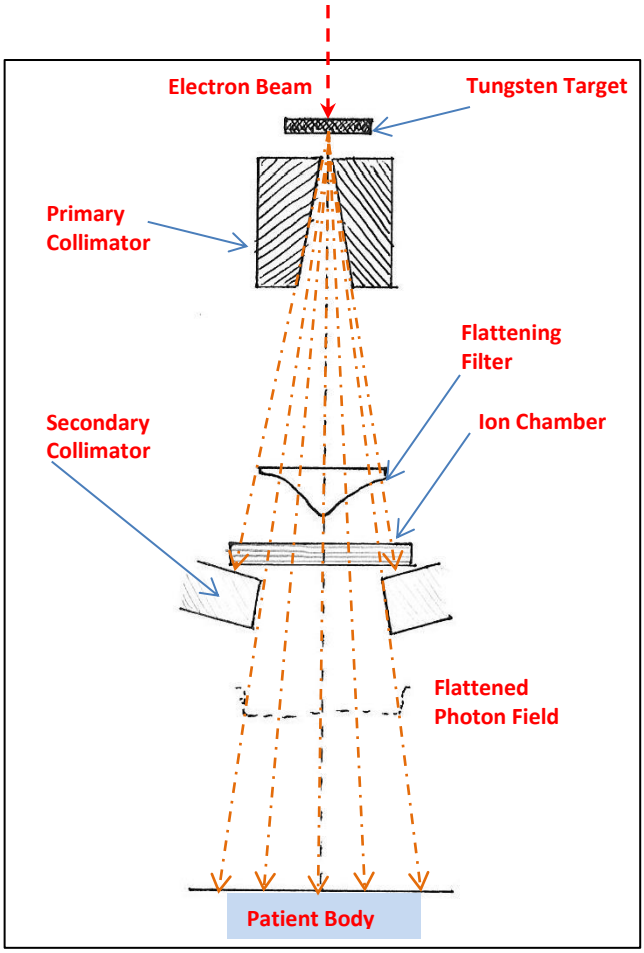

Figure 3 Treatment Head for a Modern LINAC
Figure drawn and Adapted from *(Khan FM: The physics of radiation therapy, ed 3, Philadelphia, 2003, Lippincott Williams & Wilkins, p 46.)*.

2.2. Bremsstrahlung Efficiency

Several Bremsstrahlung efficiency calculation methods were explored by Melville [2]. After further examination of each, Melville chose the high energy approximation formula shown by Equation 2.2 used by Turner [8]. This equation was chosen because it can more accurately account for Bremsstrahlung efficiency at higher electron beam energies without exceeding 100% efficiency, as observed in other methods.

$$\eta = \frac{6\times10^{-4}ZE_{\beta}}{1+6\times10^{-4}ZE_{\beta}}, \quad E_{\beta}\ beam\ energy\ in\ MeV \tag{2.2}$$

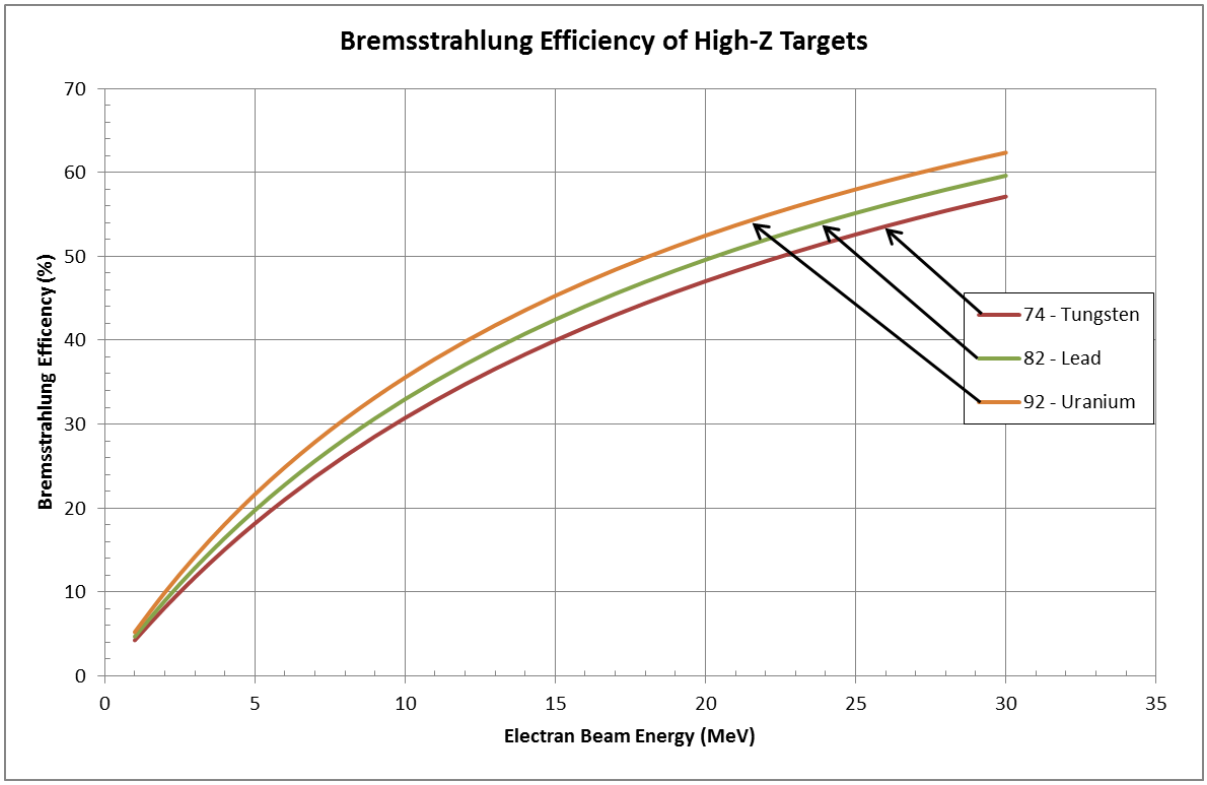

Figure 4 Bremsstrahlung Efficiency
Comparison calculated by the high-energy approximation formula within Microsoft Excel, for select high-Z nuclides.

Melville calculated 44.4% efficiency for the 18 MeV LINAC beam energy used. However, 40% was chosen as a conservative number for use in model calculations. It is apparent that using a material of higher-Z than tungsten (Z=74) could improve Bremsstrahlung efficiency and photon production rate by approximately 6% at 18 MeV (Fig 4). However, the thermal properties of the target material (such as lead or uranium) may be stressed at higher LINAC currents. Tungsten is of course a clear winner when it comes to its robust thermal properties. In an effort to perform several yield model comparisons, the 40% bremsstrahlung efficiency will be used for the photon rate data for the base case. The impact of using other efficiency values is also analyzed in different scenarios presented in section 7.

2.3. Ra-225 Yield Rate Equations

The total atom yield rate for Ra-225 in (*atoms/s*) was calculated using Equation 2.3 (below) in Melville's model [3]. This equation is the typical equation used in calculating

photonuclear reaction yields in a number of different applications; however, the format and units of variables used in this equation vary from source to source. This variation in form and use can be better understood from the equation explanations found in Appendix C for two such uses [12] [13]. Equation 2.3 calculates atom yield by the convolution of two energy dependent parameters, the photon rate $\phi(E)$ produced in the Bremsstrahlung spectrum ,and the cross-section $\sigma(E)$ for the particular reaction being studied.

$$Y = N \cdot t \cdot \int_{6.4}^{18} \phi(E) \cdot \sigma(E) \cdot dE, \qquad (2.3)$$

$$Y = N\left(\frac{atoms}{cm^3}\right) \cdot t(cm) \cdot \int_{6.4}^{18} \phi\left(\frac{Photons}{s}\right) \cdot \sigma(cm^2) \cdot dE$$

Where, Y = Ra-225 yield (atoms/s)

N = atom density of Ra-226 (atoms/cm^3)

t = radium target thickness (cm)

σ = photo-neutron (γ,n) cross-section (cm^2) for Ra-226

ϕ = photon rate in spectrum (photons/s)

In addition, the sample atom density *N* and sample thickness *t* are multiplied to this convolution integral to obtain a yield in units of atoms per second. Typically the photon rate term ϕ would be a spatially dependent term, integrated over the sample thickness, as shown below.

$$Y = N \cdot \int_0^t \int_{6.4}^{18} \phi(E, x) \cdot \sigma(E)\, dE\, dx$$

$$Y = N \cdot \int_0^t dx \int_{6.4}^{18} \phi(E) \cdot \sigma(E)\, dE$$

However, for thin targets it is assumed ϕ does not change with *x* which results in the second simplified equation above that results in the final form of Equation 2.3. In Melville's work, it is believed that the thickness term was deemed negligible due to the small

thicknesses of the samples being evaluation, i.e., the 20 mCi and 15 mCi radium needles, whose active thickness is approximately 1 mm. At a thickness of 1 mm, it can be shown by Figure 5 that the fraction of un-attenuated photons passing through this thickness is approximately 98%, in the energy range of interest 6-18 MeV. By using the linear attenuation coefficient, μ, over this energy range as presented in Figure 5, from the values in Table 7 of section 6.2, this percentage can be calculated as follows:

$$e^{-\mu t} = e^{-\mu(1mm)} = 98\% \rightarrow \phi(E,x) \approx \phi(E)$$

Therefore, the thickness integral was evaluated and left as *t*, to be multiplied by the sample atom density *N*, which in essence calculates the number of atoms per cm^2 that are normal to the incident photon field. While this equation accounts for sample thickness, and accounts for the probability of a photo-neutron reaction with the cross-section term, it does not account for the photon attenuation of a thicker sample. The 98% of un-attenuated photons as discussed above means that only 2% have interacted by Compton scattering and pair-production, leaving the remaining 98% to potentially undergo a photo-neutron reaction. This 2% reduction in available photons is negligible for the experiments carried out by Melville.

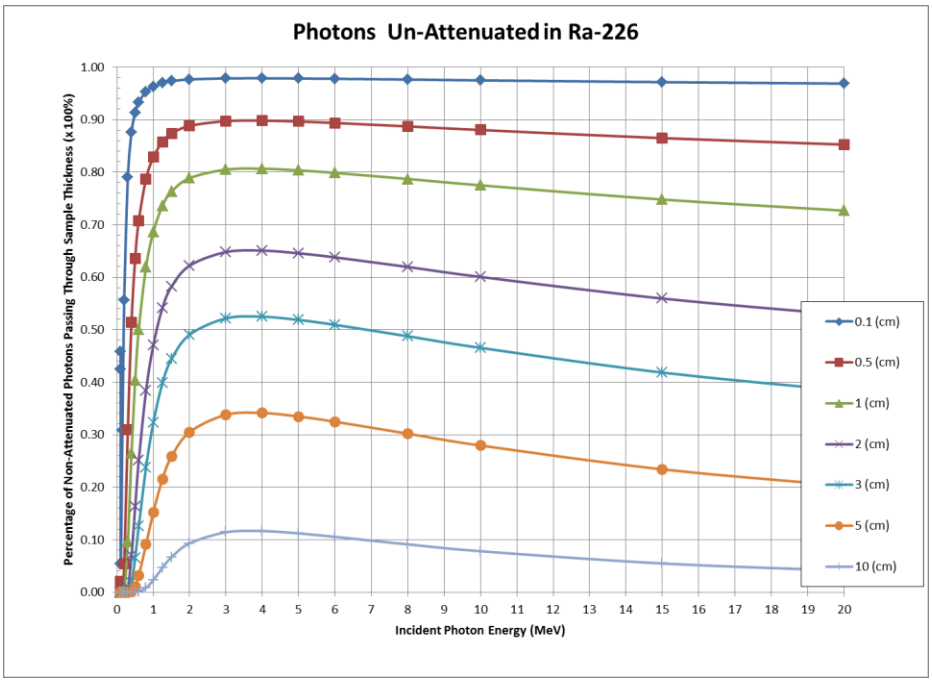

Figure 5 Fractions of Un-Attenuated Photons in Radium
Fractions of Un-Attenuated Photons in Radium through Varying Ra-226 Sample Thicknesses, Over Energies of 0.1 to 20 MeV. Data calculated using mass attenuation data provided by NIST [14]. Raw data is shown in Appendix D.

It is clear from Figure 5 (above) that Ra-226 sample thickness has an effect on photon attenuation, thereby playing a role in Ra-225 production efficiency. Therefore, in an effort to account for the fraction of photons attenuated, a correction factor was added to the yield equation. This correction term will be utilized in Equation 2.3 as follows:

$$Correction\ factor \rightarrow (e^{-\mu t})$$

Where, t is the sample thickness in cm, and μ is the linear attenuation coefficient of radium and is dependent on the incident photon energy in MeV.

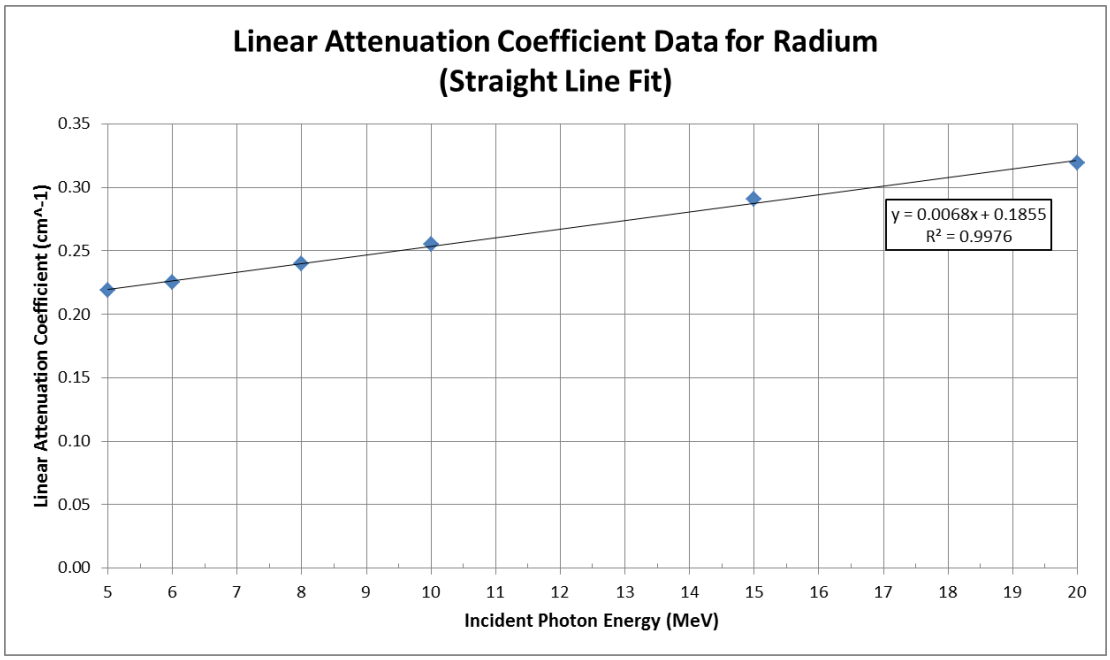

Figure 6 Linear Attenuation Coefficient for Ra-226
Linear Attenuation Coefficient for Ra-226, Over Energies of interest 5 to 20 MeV. Data calculated using mass attenuation data provided by NIST [14]. The full plot is shown in Figure 38 in Appendix D.

A section of the linear attenuation data for radium was plotted over the energies 5 to 20 MeV, and a linear relationship was obtained with a regression fit in Microsoft Excel (Fig 6).
The following equation shows this linear relationship in terms of energy, and was validated by calculating μ for several energies to ensure the equation of this line provided by the trend fit matched the data points.

$$\mu = 0.0068 \cdot E + 0.1855$$

Now μ is substituted into the correction factor above and included in the yield Equation 2.3 as shown in Equation 2.4 below:

$$Y = N \cdot t \cdot \int_{6.4}^{18} \phi(E) \cdot \sigma(E) \cdot \left(e^{-(0.0068 \cdot E + 0.1855)t}\right) dE \qquad (2.4)$$

This equation was adapted from the book *Photonuclear Reactions* [15] and was used throughout the MATLAB® models discussed in section 7. The correction factor was included to account for normally incident photon attenuation effects through the radium sample thickness, assuming thicker samples will be tested during future experiments. A more in-depth explanation for how similar correction factors were utilized can be found in Appendix C. The uncertainty studies discussed later in section 7 evaluate a change in the TENDL Ra-226 photo-neutron cross-section by +/-50%. It is important to note that changes to the total microscopic cross-section of Ra-226 are on the order of 10s of barns, whereas similar changes to the photo-neutron cross-section are on the order of 40 to 50 mb. When converted to cm^2 the change in photo-neutron cross-section is very small, and would not change the linear attenuation term by an applicable about. Therefore it would have little effect on the predicted yield and is ignored in the sensitivity analysis of section 7.5.

2.4. Transient Decay of Ra-225 and Ac-225

Once the yield rate for Ra-225 is obtained, the transient decay characteristics of Ra-225 to Ac-225 can be analyzed. In this decay process the half-life of the parent nuclide Ra-225 (14.9 days) is not significantly longer than the daughter's Ac-225 (10 days), allowing them to decay in transient equilibrium after the daughter reaches some maximum activity.

The following is a decay time calculation for analyzing the timing of chemical separation of Ac-225 from Ra-225, where an initial activity of Ra-225 decays at 14.9 days to Ac-225 whose activity initially builds from zero to a maximum activity. The time at which this maximum occurs can be calculated by Equation 2.5 as shown below [8]. This time calculation can be found in Appendix A.

$$t = \frac{1}{\lambda_2 - \lambda_1} \cdot \ln \frac{\lambda_2}{\lambda_1} \qquad (2.5)$$

Equation 2.6 calculates the activity of Ac-225 (A_2) resulting from the decay of an initial amount of Ra-225 (A_{10}) [8]. Ac-225 will reach a maximum activity of 44.06% of Ra-225

after 17.35 days of Ra-225 decay; this percentage yield is constant given any initial amount of parent Ra-225.

$$A_2 = \frac{A_{10}\lambda_2}{\lambda_2 - \lambda_1} \cdot \left(e^{-\lambda_1 t} - e^{-\lambda_2 t}\right) \tag{2.6}$$

$$\frac{A_2}{A_{10}} = \frac{\lambda_2}{\lambda_2 - \lambda_1} \cdot \left(e^{-\lambda_1 t} - e^{-\lambda_2 t}\right)$$

$$\frac{A_2}{A_{10}} = \frac{8.021}{8.021 - 5.456} \cdot \left(e^{-\left(5.456\times10^{-7}s^{-1}\right)\cdot 1499461} - e^{-\left(8.021\times10^{-7}s^{-1}\right)\cdot 1499461}\right)$$

$$\boxed{\frac{A_2}{A_{10}} = 0.4406 = 44.06\%}$$

An example calculation in Equation 2.7 to demonstrate this relationship uses the yield amount obtained from Melville's first experiment where 40 mCi of radium was irradiated for 3 hours resulting in a Ra-225 yield of ~64 µCi, and an Ac-225 yield of ~29 µCi.

$$A_2 = (A_{10})0.4406 \tag{2.7}$$

$$A_{10} = 64\mu Ci$$
$$A_2 = (64\mu Ci)0.4406$$
$$A_2 = (28.2\mu Ci)$$

The 44.06% yield relationship between these two nuclides provides a quick method to calculate the Ac-225 yield given a starting activity of Ra-225.

3. LINAC Photon Spectra

3.1. Spectrum Curve Fitting

The following calculation shows how LINAC parameters are used to calculate the theoretical number of photons in the spectrum exiting the tungsten target.

LINAC Parameters: E_{max} = *18 MeV, maximum LINAC beam energy*

I_{peak} = *36 mA, peak pulse current*

f = 180 Hz, pulse frequency

t = 4μs, pulse length

$I_{avg} = (36x10^{-3}A)(4x10^{-6}s)(180\ s^{-1}) = 26\ \mu A$

$Z_{tungsten} = 74$

By first calculating the total number of electrons emitted by the beam per second,

$$electrons/_{sec} = (26 \times 10^{-6} A) \cdot \left(\frac{1\ electron}{1.602 \times 10^{-19} coulombs}\right)$$

$$electrons/_{sec}\ in\ Beam\ = 1.618 \times 10^{14}$$

And multiplying that value by the Bremsstrahlung efficiency at 18 MeV of 44.4%, the total estimated number of photons/s emitted from the tungsten target is:

$$Photons/_{sec}\ in\ spectrum\ = (1.618 \times 10^{14}) \cdot 0.444 = 7.187 \times 10^{13}$$

Using a conservative 40% efficiency versus the calculated 44.4% at 18 MeV, the number of photons per second in the spectrum is:

$$Photons/_{sec}\ in\ spectrum\ = (1.618 \times 10^{14}) \cdot 0.40 = 6.5 \times 10^{13}$$

The analysis conducted here assumes the same Bremsstrahlung photon spectrum as the 18 MeV LINAC used by Melville. The photon spectrum data in Melville's work was provided as a plot only; therefore its values were visually interpolated for a recreated photon spectrum. This step was necessary to find the area under the photon spectrum curve over all energies 0 – 18 MeV (Fig 7), which represents the total number of photons/s in the spectrum.

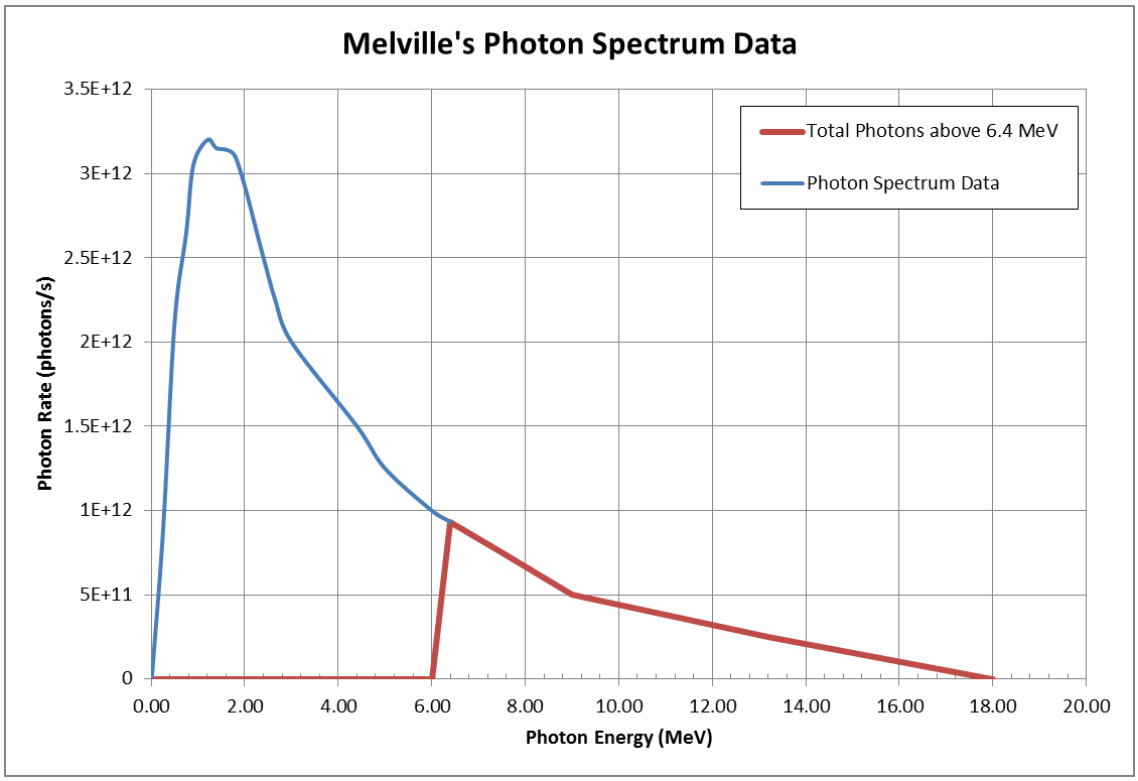

Figure 7 18 MeV LINAC Photon Data Spectrum
Recreation of the photon data spectrum provided by Varian 18 MEV LINAC [1] , where the area under the red line represents the total number of photons in the spectrum above 6.4 MeV.

The area under the curves was calculated by the Trapezoid method. A total of 1.62×10^{13} photons/s was calculated in the entire photon spectrum over all energies (Fig 7, area under both blue and red curve).

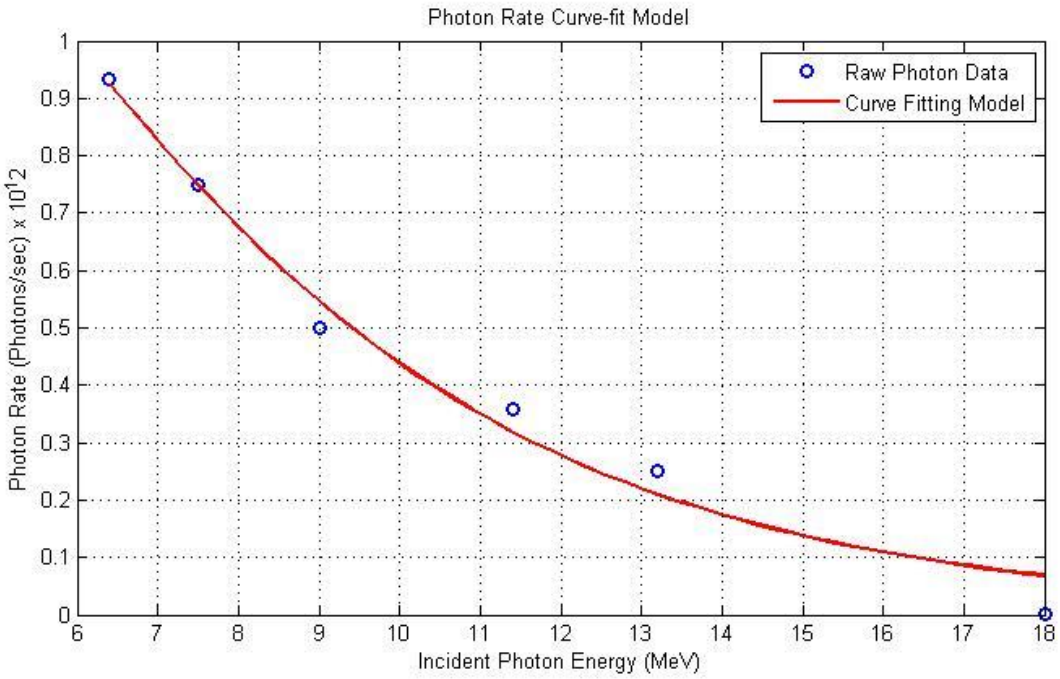

Figure 8 Curve Fitting Model Photon Spectrum Data
MATLAB® Curve fitting model, fitted to the Varian photon spectrum data above 6.4 MeV, represents all photons that can cause a (γ,n) reaction with Ra-226.

If the theoretical value of 6.5 x 10^{13} photons/s using a 40% Bremsstrahlung efficiency is compared to the actual total Varian photon spectrum data of 1.62 x 10^{13} photons/s, there are 75% fewer photons/s in the actual spectrum data. This difference may be accounted for by photon losses in the tungsten target, primary collimator, and flattening filter before the spectrum was measured. Out of the 1.62 x 10^{13} photons/s measured in the whole spectrum, the amount between 6.4 MeV to 18 MeV was calculated at 4.04 x 10^{12} photons/s. This represents the area under the red curve in Figure 7 which is also the area under the curve in Figure 8.

3.2. Various LINAC Spectra

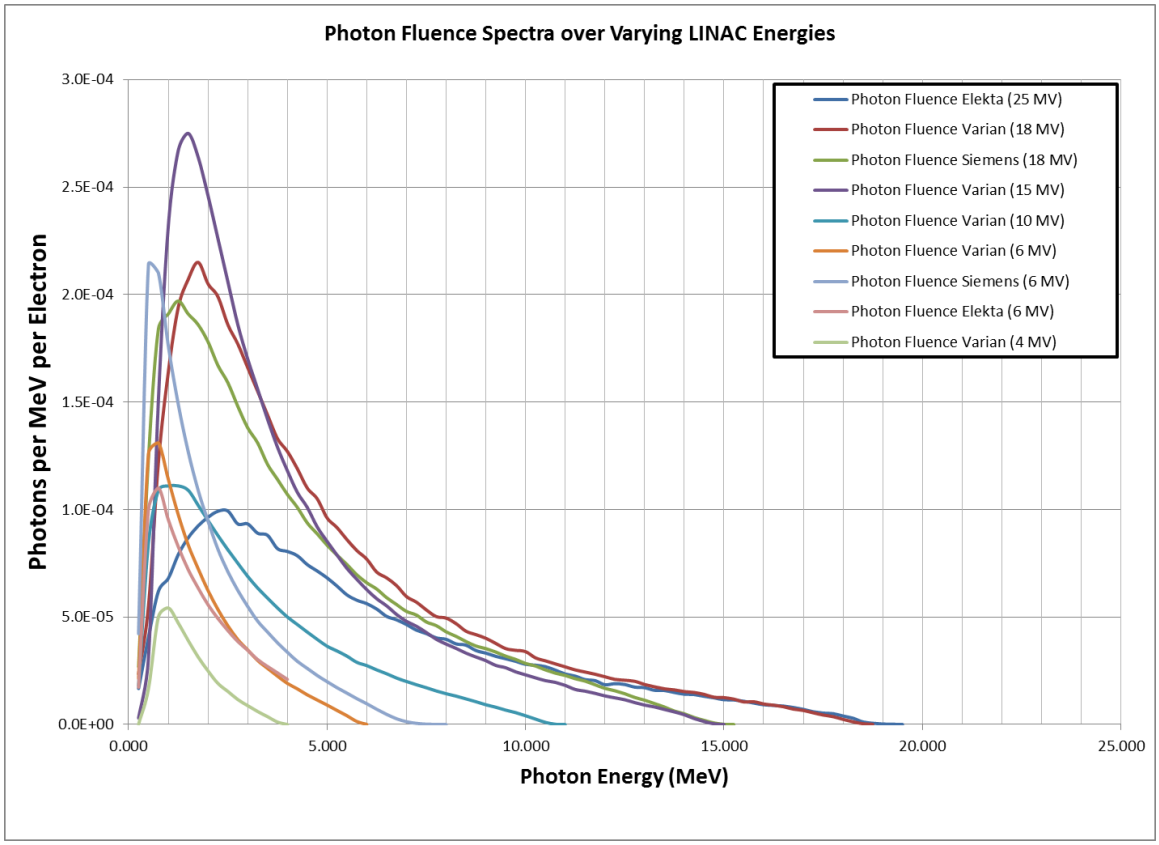

Figure 9 Photon Fluence Spectra from Various LINACs
Photon fluence spectra normalized to the corresponding photon spectrum area from various LINACs of differing energies. This plot was created with raw data reported in and adapted from: [Sheikh-Bageri et al, 2002], [16].

Figure 9 shows various photon beam spectra from different medical LINACs, and was part of an effort to model each spectrum using Monte-Carlo transport calculations [16] [17]. This work and others were explored to determine any noticeable trend in the photon spectra at varying LINAC energies, i.e., 10, 15, 18, or 25 MeV. One clear trend appears to be the nature of the positively-skewed curve representing each spectrum. Most curve peaks, hence the majority of the photons, occur between 1 and 2 MeV, then tail off stopping at their maximum energy. An additional observation from the differing spectra above is the over-lapping photon spectrum values between 6 and 13 MeV for the higher energy LINACs. This indicates little difference in available photon energies beyond ~6 MeV for LINACs with electron beam energies of 15 to 25 MeV. What is not completely clear by a number of LINAC spectrum studies is the relationship between spectrum fluence, LINAC parameters,

and the location (in the LINAC beam spectrum) where the spectrum was measured. There are quite a few areas where losses exist between the origination of the electron beam and the location where the photon fluence is measured. Many losses exist, such as Bremsstrahlung attenuation in the high-Z target thickness, and attenuation effects by the many collimators and flattening filters arranged in the LINAC head. It was found to be rather difficult using plots of various photon spectra or documented raw data spectra (from various papers and various experiments) to establish a framework of consistency for modeling purposes. Some worthwhile details were presented in the various journal articles. However, there was not enough detail to provide a consistent trend of spectral data for accurate curve fitting to be appropriately applied to yield calculations for a particular LINAC. While these curves could be fitted, and yields calculated, it was not possible to link the spectrum data back to the LINAC electron beam parameters due to unknown attenuation affects from the collimators or filters.

There are a number of uncertainties in modeling random LINAC spectra as described above. Therefore, it would be best to first seek out a LINAC company such as Varian, or Siemens, and work with them on understanding what type of LINAC is possible. This step will provide possible LINAC parameter enhancements such as power, frequency, pulse length, pulse current, and estimated photon beam intensity utilized in a custom design. With that knowledge a more accurate Ac-225 yield estimate could be performed, leading to further refinements of LINAC parameters.

In an effort to optimize yield, a relationship was developed between radium sample dimensions and the cross-sectional distribution of a given photon field. In calculating the number of photons incident upon a given sample one must consider the cross-sectional area of the photon spectrum, and its distance from the tungsten target. To better understand this relationship see the schematic in Figure 10 from which Equations 3.1, 3.2, and 3.3 were derived.

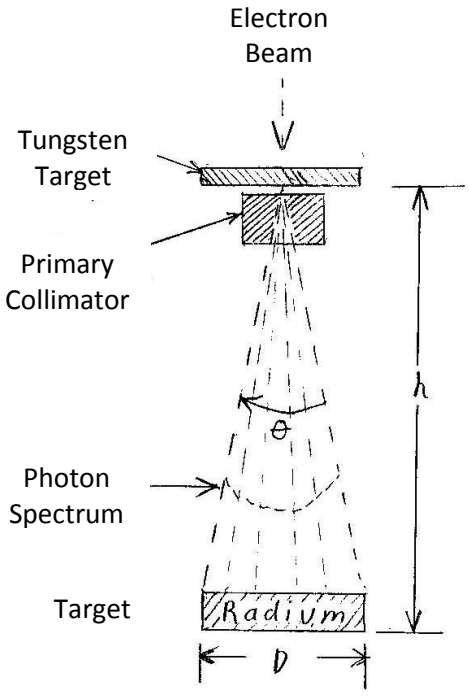

Figure 10 Radium Sample Positioning
LINAC spectrum schematic showing effects of angular distribution of photons on a given radium sample diameter.

There is a relationship between target-to-sample distance *h*, spectrum distribution angle θ, sample diameter *D*, and cross-sectional area of the photon field *A*.

$$D_{sample} = 2 \cdot h \cdot \tan\left(\theta/_2\right) \tag{3.1}$$

$$A_{cross-section} = \frac{1}{4}\pi\left(D_{sample}\right)^2 \tag{3.2}$$

$$h = \frac{\sqrt{A/\pi}}{\tan\left(\theta/_2\right)} \tag{3.3}$$

This equation demonstrates if a spectrum distribution angle θ, and cross-sectional area *A* of a circular disk sample are given, then a distance *h* from the tungsten target can be determined in order to locate the sample to maximize the photon spectrum exposure to the sample area.

3.3. Units of Photon Fluence

Given an absorber of thickness *x*, the following equations express different measures of photon fluence [8].

Incident Fluence, is the number of photons of a given energy passing through a cross-sectional area in a specific time period.

$$\Phi_0 = \frac{\#\ of\ photons}{unit\ area} \tag{3.4}$$

Fluence Rate, is the number of photons passing through a given area per unit time.

$$\dot{\Phi}_0 = \frac{\#\ of\ photons}{unit\ area \cdot unit\ time} = \frac{photons}{m^2 \cdot s} \tag{3.5}$$

Energy Fluence, is the amount of photon energy crossing through a given area.

$$\Psi_0 = \frac{Joules}{m^2} = \Phi_0 \cdot h\nu \tag{3.5}$$

where, $h\nu = photon\ energy,$

$h = 6.6261 \times 10^{-34}\ J \cdot s\ (Planck's\ Const)$

$\nu\ =\ the\ photon\ frequency\ (s^{-1})$

Energy Fluence Rate or photon energy "intensity", is simply the energy fluence per unit time, and is expressed as:

$$\dot{\Psi}_0 = \frac{Joules}{m^2 \cdot s} = \dot{\Phi}_0 \cdot h\nu \tag{3.6}$$

4. Photo-neutron Cross-sections

The Breit-Wigner formula [12] describes the photo-neutron cross-section at a resonance peak, shown below.

$$\sigma(E) = \frac{(\Gamma/2)^2}{(E-E_r)^2+(\Gamma/2)^2} \cdot \left(\frac{E}{E_r}\right) \cdot \left[\sqrt{\frac{E-E_t}{E_r-E_t}}\right] \cdot \sigma_{E_r} \tag{4.1}$$

Where,

E_r = 13.45 MeV	(giant dipole resonance energy)
E_t = 6.4 MeV	(reaction threshold energy)
Γ = 3.97 MeV	(FWHM at resonance)
σ_{Er} = 521 mb	(peak resonance cross-section)

The particle resonance parameters used in Equation 4.1 above are shown for Bi-209, which were chosen by Melville under the assumption that similar nuclide mass numbers yield similar resonance cross-section parameters [2]. The assumption is that since the cross-sections for Bi-209 and Th-232 were in close agreement and were the only two nuclides of similar atomic mass to Ra-226 in which the photo-neutron cross-sections were known, the Bi-209 photo-neutron cross-section data would be suitable as a substitute for that of Ra-226.

In the process of seeking out a potential source for photo-neutron cross-section data for Ra-226, all major nuclear data libraries were searched. The National Nuclear Data Center (NNDC) was searched, which uses the Experimental Nuclear Reaction Data (EXFOR) library. EXFOR draws data from many major databases such as ENDF, CINDA, and IBANDL [18]. In addition, the Korean Atomic Energy Research Institute was searched, as well as the Centre for Photonuclear Experiments Data, from Lomonosov Moscow State University [19]. All above sites revealed no photonuclear cross-section data for Ra-226. Then, the TALYS-based Evaluated Nuclear Data Library (TENDL) was discovered. TENDL is provided through the Nuclear Research and Consultancy Group (NRG) in the Netherlands [20].

In addition to this newly found photo-neutron cross-section data for radium, another photonuclear data resource was found in the Handbook of Photonuclear Data for Applications, Cross-sections and Spectra [21]. Within this reference an atlas of Giant Dipole Resonances (GDR) was tabulated, listing the various GDR parameters such as peak energy and peak cross-section for over 220 isotopes. Various reaction parameters were tabulated for each isotope by experimentally measured values, such as photo-absorption, neutron yield, single, double, and triple neutron production, as well as fission and charged particle emission [21]. In an effort to find a trend in this data, for further confirming the TENDL Ra-226 cross-section data, the single neutron cross-section data were manually extracted from this atlas for all available nuclides and plotted against the nuclide atomic mass (Fig 11).

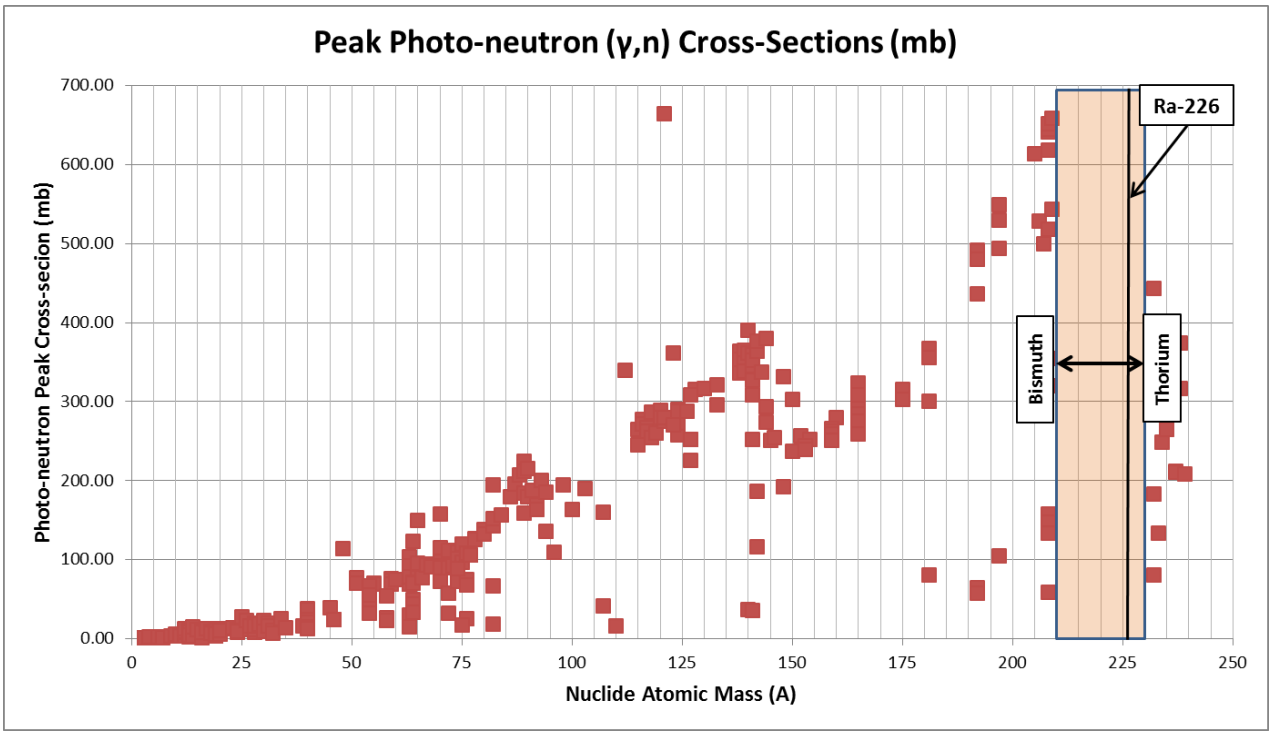

Figure 11 Peak (γ,n) Reaction Cross-section Data
Single neutron (γ,n) reaction cross-section data recreated from the tabulated photonuclear resonance data, Adapted data from: (*Handbook of Photonuclear Data for Applications, Cross-sections and Spectra*), *[IAEA TECDOC-1178, 1999]*, [21].

It is apparent a gap is present between the isotopes of Bi-209 and Th-232 where no experimental data exist. The main reason for this is due to the many short-lived isotopes between bismuth and thorium, which are not easy to experimentally evaluate. As a result of the lack of data in this area, and lack of trending behavior from the peaks beyond bismuth, the peak resonance cross-section of radium could not be confirmed by this data.

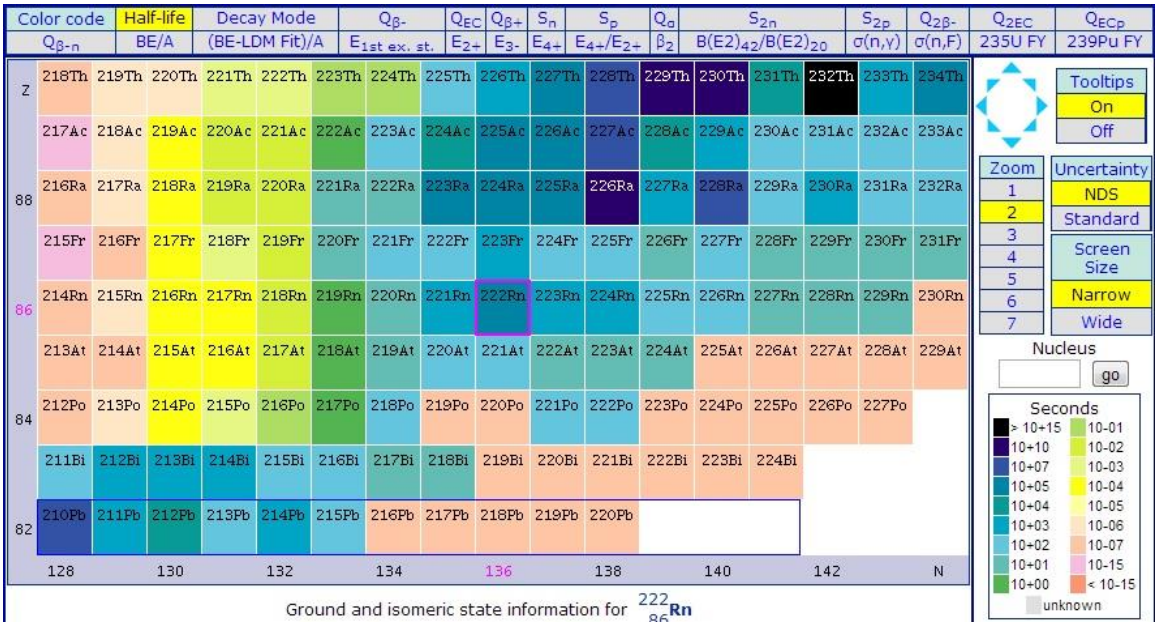

Figure 12 Chart of Nuclides Half-Lives
Chart of nuclides section capturing color codes half-lives of isotopes above stable Bi-209 and below Th-232, Adapted from Public Domain [9].

To further understand the shortness of half-lives for isotopes residing between Bi-209 and Th-232 see Figure 12 above. The vast majority of half-lives in this range of isotopes are shorter than a day, with only several in the year range. Ra-226 is the longest in this range at 1600 yrs, but no experimental results were listed for this isotope.

4.1. TALYS Background

In the past several years the International Atomic Energy Agency (IAEA) has developed a photonuclear database called TENDL comprising of a large collection of photonuclear reaction data for most nuclides. While some reaction data sets are experimentally derived others are generated by a program called TALYS. It is similar to the general purpose Monte Carlo N-Particle code (MCNP). TENDL has recently released its latest 2012 version, and has provided photonuclear data for Ra-226 covering the many potential reaction types. This thesis has utilized this newly available data set to perform additional calculations of Ra-225 yield rates.

The TENDL database was initiated in 1998 by the Nuclear Research and Consultancy Group (NRG) in Petten, The Netherlands and at CEA Bruyeres-le-Chatel, France [22]. TALYS is a nuclear reaction program that was developed to provide a comprehensive

resource of nuclear reaction types in the 1 keV to 200 MeV energy range [22]. TALYS was designed as a coding tool for the analysis and prediction of nuclear reactions, and meant to be used for scientific experiments, in addition to generating nuclear data for applications. It draws on a number of different nuclear reaction models tied into this one code. It uses a combination of experimental data and theoretical models to establish relationships between particle and nuclei interactions. When no experimental measurements are available for a certain nuclide TALYS can generate reaction data for all open reaction channels by user-defined energies and angular grids [22]. Much more can be gained by fully exploring the TENDL site and reviewing the detailed TALYS 1.4 user manual [22]. With no other information available, this photo-neutron reaction cross-section data provided for Ra-226 will be applied to the simulated LINAC production models in section 7, until which time future experiments can be conducted to validate the TALYS data.

Cross-section data obtained from TENDL-2012 for all major photonuclear reactions with Ra-226 is shown below (Fig 13). It is apparent from Figure 13, that the (γ,n) and (γ,2n) reaction cross-sections greatly dominate over all other photonuclear reaction types.

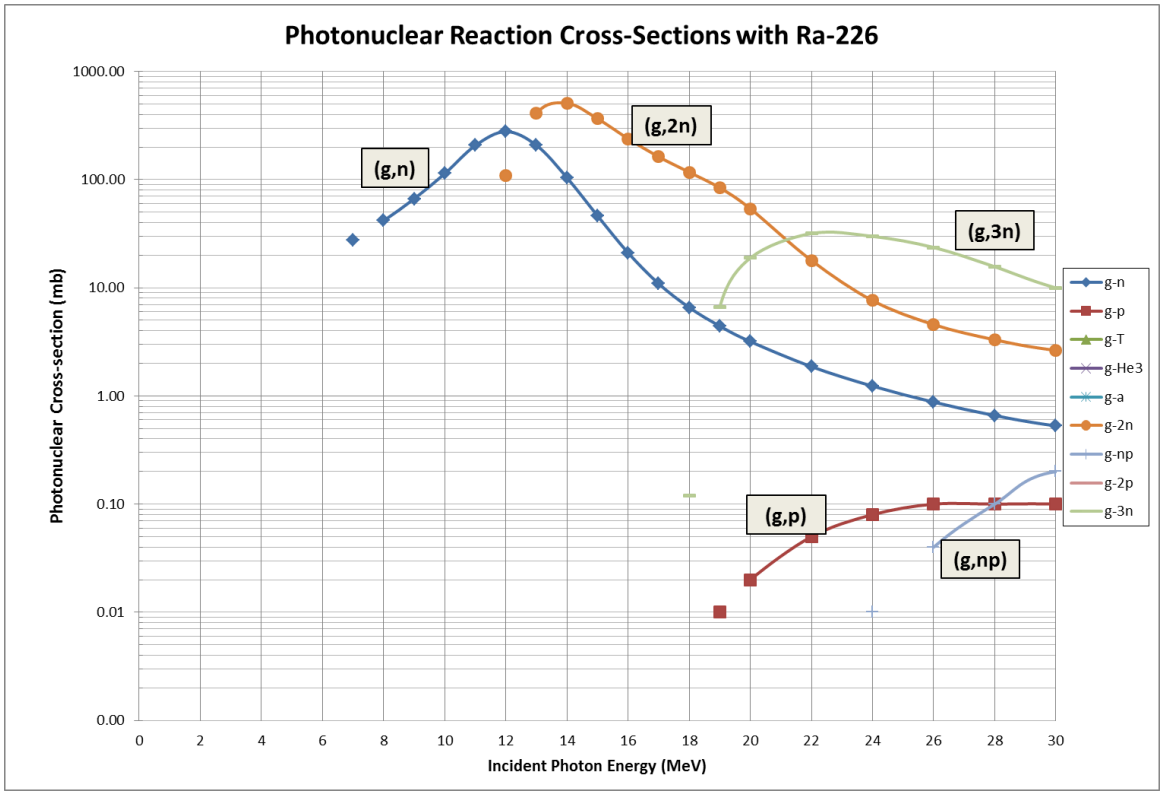

Figure 13 Ra-226 Reaction Cross-sections
Photonuclear cross-section data for all major reactions with Ra-226,
Adapted from Public Domain [20].

The reaction energy threshold to liberate 1-neutron and 2-neutrons is 6.4 MeV and 11.4 MeV, respectively as seen in Table 1. The (γ,2n) cross-section data was not considered in the yield calculations performed in section 7 below. The (γ,n) reaction cross-section already accounts for the probability of a 2-n reaction occurring above 11.4 MeV, where the 1-n cross-section curve responds accordingly by decreasing to lower cross-section values as photon energies increase.

Table 1 Resultant Nuclides of Photonuclear Reaction with Ra-226
Resultant nuclides from the most likely photonuclear reactions with Ra-226, Adapted from Public Domain [20].

Reaction Type	Threshold Energy (MeV)	Resultant Nuclide	Residual Particle
(γ,n)	6.4	Ra-225	1-neutron
(γ,P)	7.5	Fr-225	1-proton
(γ,T)	9.7	Fr-223	1-triton
(γ,He3)	8.5	Rn-223	1-He3
(γ,A)	-4.9	Rn-222	1-Alpha
(γ,2n)	11.4	Ra-224	2-neutrons
(γ,np)	13.4	Fr-224	1-n, 1-p
(γ,2P)	11.3	Rn-224	2-proton

Table 2 Resultant Decay Chains

Decay chains of the resultant isotopes from photonuclear reactions with Ra-226, Adapted from Public Domain [9].

Various Isotopes Resulting from Photonuclear Reactions with Ra-226 with their Decay Chains							
	Nuclide	Decay Method	Half-Life		Nuclide	Decay Method	Half-Life
Parent	Fr-225	β-	3.95m	*Parent*	Rn-222	α	3.8d
Daughter	Ra-225	β-	14.9d	*Daughter*	Po-218	α	3.1m
Daughter	Ac-225	α	10d	*Daughter*	Pb-214	β-	26.8m
Daughter	Fr-221	α	4.9m	*Daughter*	Bi-214	β-	19.9m
Daughter	At-217	α	32.3ms	*Daughter*	Po-214	α	164us
Daughter	Bi-213	β-	45.6m	*Daughter*	Pb-210	β-	22.3y
Daughter	Po-213	α	4.2us	*Daughter*	Bi-210	β-	5.01d
Daughter	Pb-209	B-	3.25h	*Daughter*	Po-210	α	138.37d
Daughter	Stable Bi-209			*Daughter*	Stable Pb-206		
	Nuclide	Decay Method	Half-Life		Nuclide	Decay Method	Half-Life
Parent	Fr-223	β-	22m	*Parent*	Rn-224	β-	107m
Daughter	Ra-223	α	11.43d	*Daughter*	Fr-224	β-	3.3m
Daughter	Rn-219	α	3.96s	*Daughter*	Ra-224	α	3.6d
Daughter	Po-215	α	1.78ms	*Daughter*	Rn-220	α	55.6s
Daughter	Pb-211	β-	36.1m	*Daughter*	Po-216	α	0.145s
Daughter	Bi-211	α	2.14m	*Daughter*	Pb-212	β-	10.64h
Daughter	Tl-207	β-	4.77m	*Daughter*	Bi-212	β-	60.5m
Daughter	Stable Pb-207			*Daughter*	Po-212	α	0.3us
				Daughter	Tl-208	β-	3.05m
				Daughter	Stable Pb-208		

Tables 1 and 2 provided above offer a quick reference to the decay chains of radionuclides resulting from the various photonuclear reactions of Ra-226.

4.2. Cross-section Comparison

To evaluate the predictions of the new TENDL cross-section data for Ra-226, a comparison of surrounding nuclide cross-sections was performed between data from NNDC (ENDF data) and TENDL-2012 data.

As can be seen in Figure 14, there is good agreement between ENDF data and TENDL data for Bi-209 and U-233. However, it is noted that there is some difference in the TENDL data over-predicting the EXFOR data for Th-232. It is also clear from this plot that the

Ra-226 photo-neutron cross-section is considerably less than Bi-209, with the peak resonance shifted from 13.5 MeV (Bi-209) to 12 MeV (Ra-226). In addition the peak photo-neutron cross-section value of ~280 mb for Ra-226 is significantly smaller than the ~520 mb peak of Bi-209. A comparison was simply made visually to ascertain how well the TENDL data overlaid the ENDF data. Given that there is some agreement between cross-section data of the surrounding nuclides with known experimental data, Figure 14 provides a reasonable assurance that the TENDL predictions for Ra-226 may be accurate. A sensitivity analysis of how the yield amounts vary with the Ra-226 photo-neutron cross-sections will be performed in section 7. But, until such time an experiment can be performed to determine the actual Ra-225 sample activity yields following irradiation, the TENDL data is all that currently exists.

In addition, several other nuclide cross-sections (Pb-206, Pb-208, and U-238) were plotted in Figure 15, again showing reasonable agreement between the experimental data and TENDL data. Figure 15 shows that TENDL provides some overestimation in the peak resonance values beyond the EXFOR data. If nothing else, that may indicate that the peak resonance for Ra-226 as predicted by the TENDL data may be an over-prediction in the worst case and not as likely to be an under-prediction.

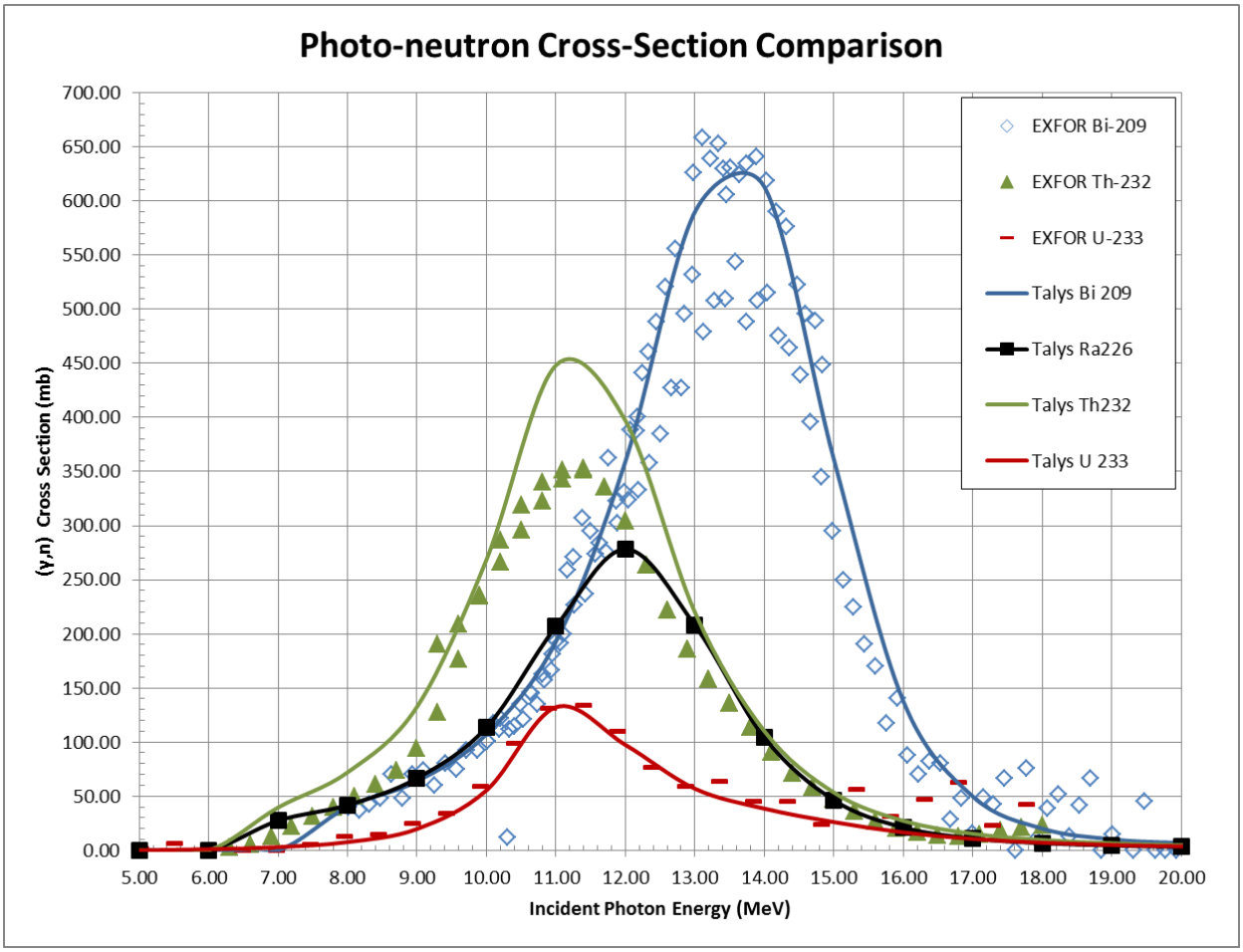

Figure 14 Photo-neutron (γ,n) Cross-sections Comparison A
Photonuclear (γ,n) cross-sections for select nuclides compared to Ra-226; comparison is between TALYS code data and EXFOR data, Adapted from Public Domain [20] and [18].

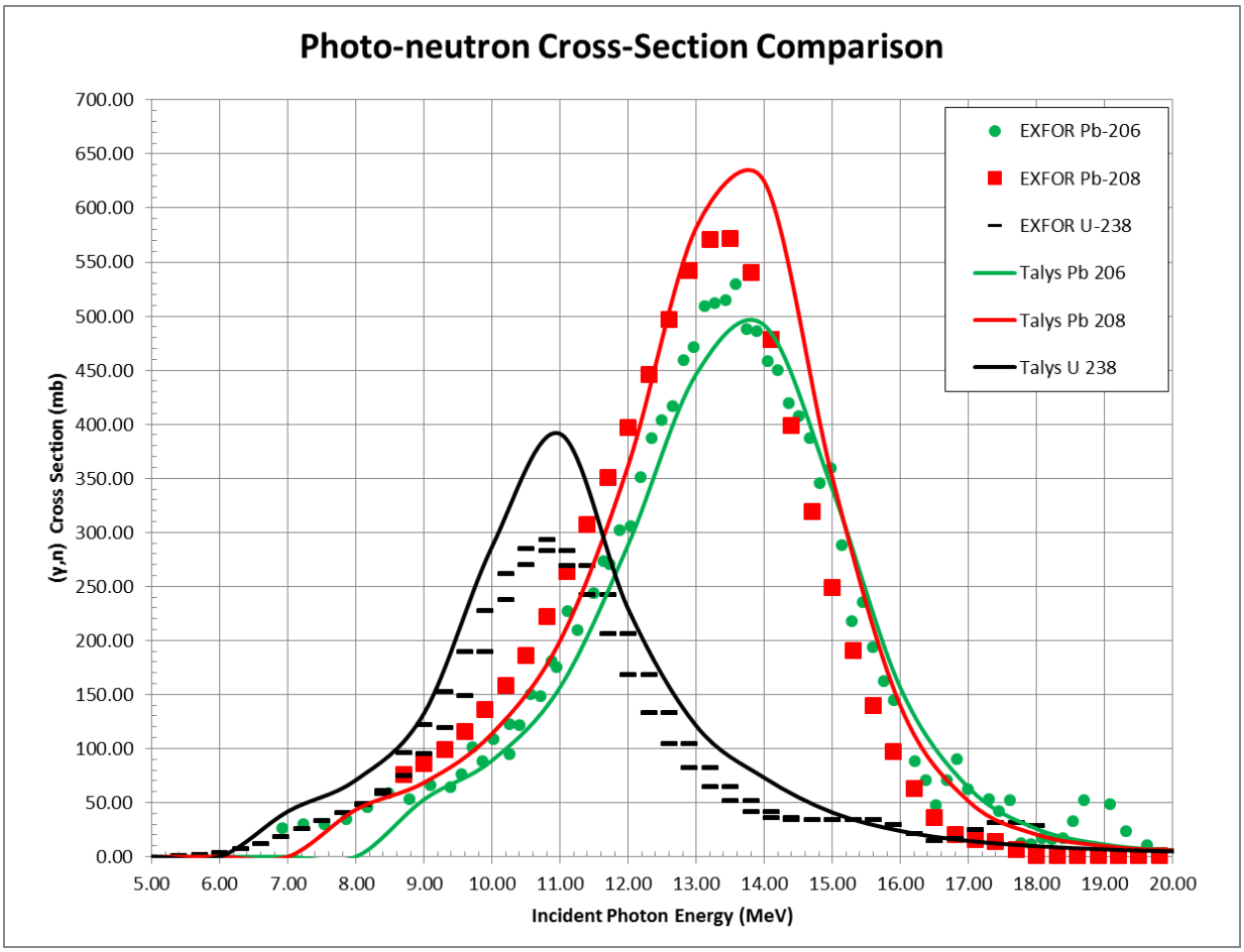

Figure 15 Photo-neutron (γ,n) Cross-section Comparison B
Photo-neutron (γ,n) cross-sections for other select nuclides compared to Ra-226.
Comparison is between TENDL data and EXFOR data, Adapted from Public Domain [20] [18].

4.3. Cross-section Data Curve Fitting

It was necessary to develop a curve fitting model for both the photon spectrum data and cross-section data to allow easier yield calculation within MATLAB®. Yield calculations are done by multiplying the photon data with cross-section data at each energy (Equation 2.3 or 2.4). However, it becomes rather arduous to perform yield calculations on a per energy basis if a number of varying photon spectrum data sets are modeled with data on differing energy intervals. One would need to perform many linear interpolations of one data set to match the other. For that reason a curve fitting model was designed to fit a known distribution over given energy ranges, allowing most data sets to be fitted.

Figure 16 shows cross-section resonance plots for each of the potential photo-neutron reaction products (1-n, 2-n reactions) over typical LINAC photon energies (4 – 20 MeV).

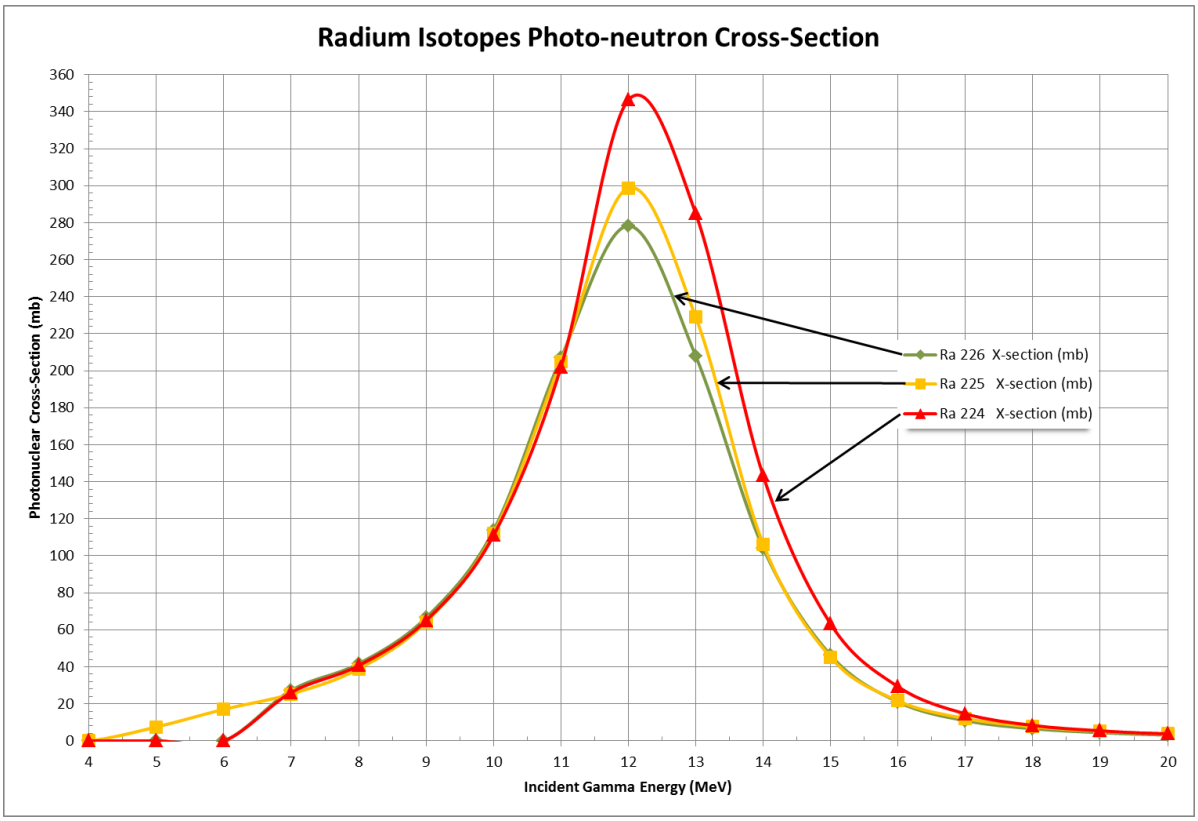

Figure 16 Radium's Photo-neutron (γ,n) Cross-sections
Photo-neutron (γ,n) cross-sections for radium isotope resulting from a (γ,n) and a (γ,2n) reactions, Adapted from Public Domain [20].

The Ra-226 photo-neutron cross-section curve from Melville's work was reproduced and overlaid with the TENDL Ra-226 cross section data (Fig 17) with their corresponding fitted curves. The TENDL Ra-226 peak resonance cross-section occurs at ~280 mb which is nearly half the magnitude of the 520 mb peak as shown by Melville's curve. The affect this has on the atom yield will be evident in chapter 7.

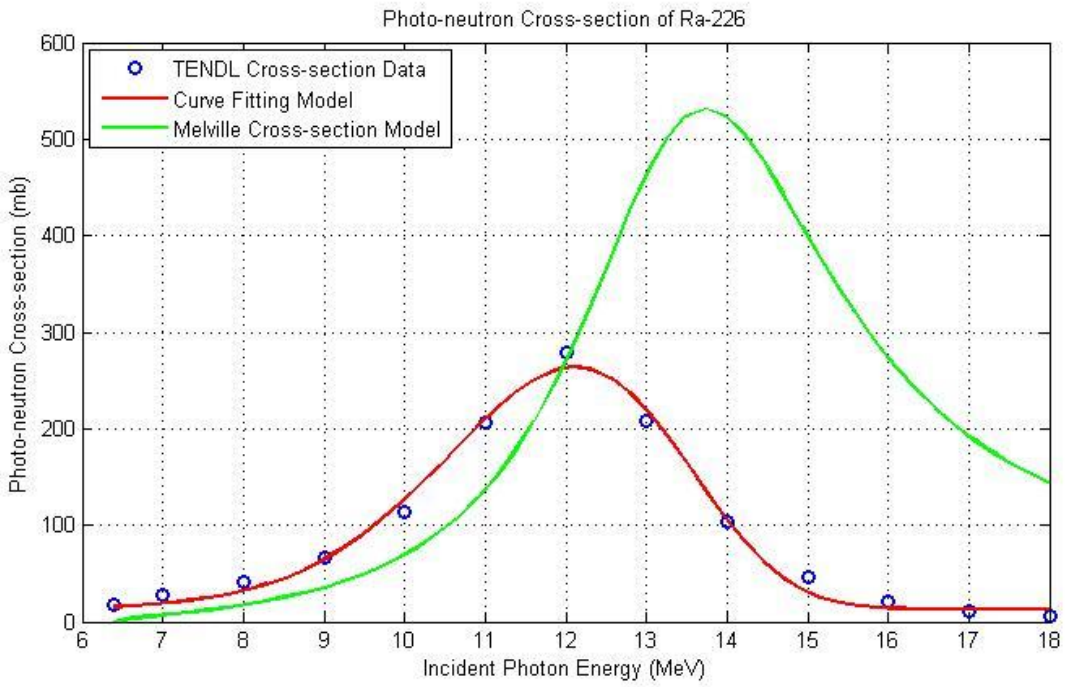

Figure 17 Photo-neutron (γ,n) Cross-sections Ra-226 vs Bi-209
MATLAB® generated, Photo-neutron (γ,n) cross-sections for Ra-226 'red' (TENDL), compared to Bi-209 'green' cross-section formula, Public Domain [2].

The data shown in *Appendix E* was used in MATLAB® to generate both cross-section curves (Fig 17), in addition to the photon spectrum curve in Figure 8. Melville used photon rate data for the Varian 2100C 18 MeV LINAC in his experiments. However, since the raw data was not tabulated for re-plotting, a number of data points had to be visually interpolated from the photon spectrum plot provided in his thesis. The data was carefully interpolated and a spectrum recreated for further curve fitting. Photon data and Ra-226 cross-section data were imported from Microsoft Excel by MATLAB®, to be utilized for curve fitting.
A modified Weibull distribution function (see Appendix A) was used in MATLAB® to fit a curve to both the cross-section and photon rate data. These two curves were then multiplied together at each energy to obtain an atom yield rate over the energy range of interest as previously discussed in section 2.3.

5. Radium 226

Prior to discussing the availability of radium, it is important to first understand some of its characteristics such as compounds, decay chain, radioactivity, and history of uses.

5.1. Production and Chemical Compounds

Radium occurs naturally and was first discovered in "pitch-blend" or uranium ore, existing in secular equilibrium with the U-238 decay chain. Due to radium's very reactive nature with air and rapid decomposition in water, it is generally manufactured in the form of radium salts, such as radium bromide $RaBr_2$ and radium chloride $RaCl_2$ [23]. The production of radium bromide involves a number of chemical processes, such as dissolution of uranium ore with barium salt and sulfuric acid, separation of radium from the many other components, and finally the drying and crystalizing process that leads to the end product. $RaBr_2$ has a material density of 5.79 g/cm^3, and a molecular mass of 386 g/mol, with the potential to extract 257 mg of radium per ton of U_3O_8 [23] [24].

5.2. Ra-226 Radioactive Characteristics

Table 3 Radioactive Properties of Radium-226
Radioactive properties of Radium-226 and daughters. Adapted from [25].

Radioactive Properties of Radium 226 and its Daughters							
Isotope	Half-Life	Natural Abundance *(%)*	Specific Activity *(Ci/g)*	Decay Mode	Radiation Energy *(MeV)*		
					Alpha *(α)*	Beta *(β)*	Gamma *(γ)*
Ra-226	1600 *yr*	>99	1.0	α	4.8	0.036	0.0067
Rn-222	3.8 *days*	-	160,000	α	5.5	<	<
Po-218	3.1 *min*	-	290 *million*	α	6	<	<
Pb-214	27 *min*	-	33 *million*	β	-	0.29	0.25
Bi-214	20 *min*	-	45 *million*	β	-	0.66	1.5
Po-214	0.00016 *sec*	-	330 *trillion*	α	7.7	<	<
Pb-210	22 *yr*	-	77	β	-	0.038	0.0048
Bi-210	5.0 *days*	-	130,000	β	-	0.39	-
Po-210	140 *days*	-	4500	α	5.3	<	<

5.3. Ra-226 Decay Chain

Ra-226 is part of the U-238 decay chain (Fig 18), and is an alpha emitter decaying to Rn-222 (radon gas). The half-life of Ra-226 is 1600 years, and is highly radioactive due to the decay specific activity of its many daughters as shown in *Table 3* above. This high radioactivity requires proper source management and significant shielding. Radium's decay chain leads to stable lead Pb-206. However, along the way there are five alpha emitting isotopes and 4 beta emitters that result in an array of betas and gammas of varying energy.

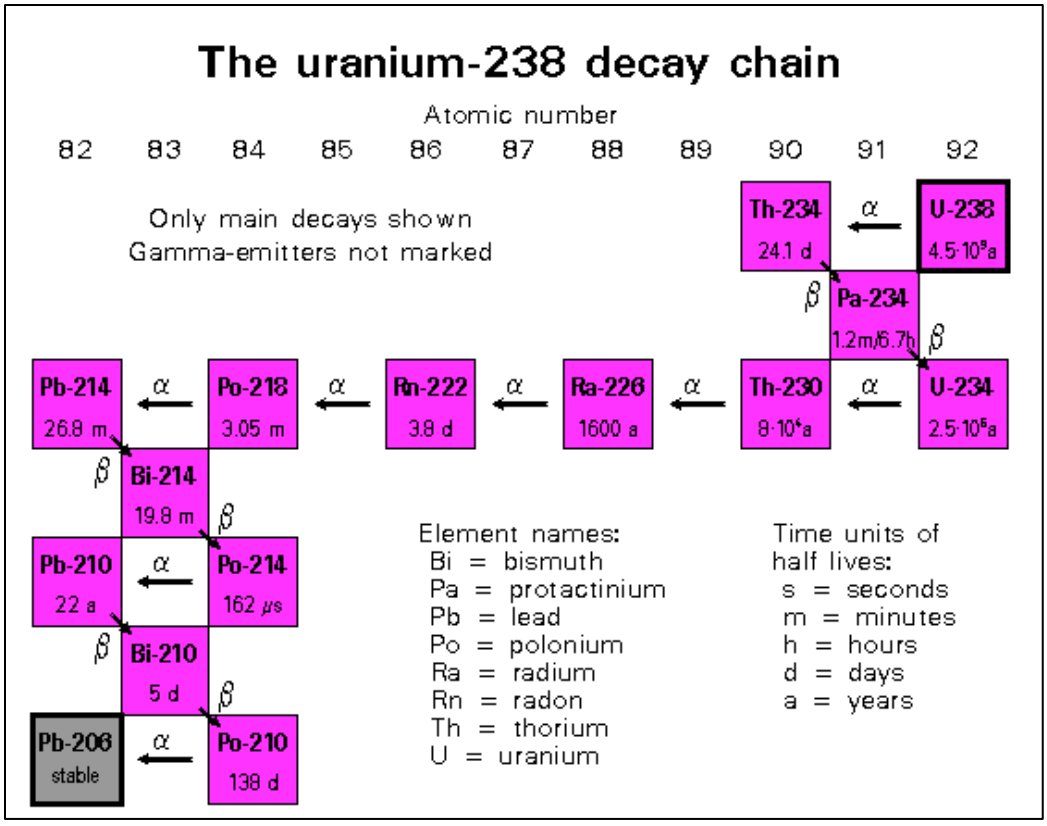

Figure 18 U-238 Decay Series
The U-238 decay series, of which Ra-226 and its daughters are a part, Public Domain [26].

5.4. National Inventory

Due to its importance to this research it is necessary to explore the availability and supply of Ra-226. Ra-226 was the first radioactive material discovered and was produced and used in a number of differing applications throughout the 1930s, 40s and 50s. The birth of nuclear reactors in the late 1950s led to a number of other radioactive sources that served a similar purpose as Ra-226, but were far less hazardous. With the discovery of the many new 'reactor

bred' isotopes, Ra-226 production was stopped in the 1960s. Even though radium production was halted, its use remained for a short time throughout the medical world, industry, and research.

Ever since the use of radium was stopped, many sources that existed were simply left at their locations of use and in many cases stored in inadequate conditions. These conditions remained so for many decades until the IAEA began an initiative to establish some standards for the proper maintenance and storage of these radioactive sources [27] [28]. Several technical reports throughout the early 1990s led to a 1996 report for the conditioning and interim storage of spent radium sources [29]. It provides some worth-while information on the current state of worldwide (mostly USA) radium sources. More precisely it shares some estimates as to the gross amount of radium that still resides within medial facilities, industrial locations, and research labs. The IAEA also proposes methods and guidance for waste management operators and regulators within many Member States where radium sources exist [30]. It additionally provides useful information for the collection of and proper storage and conditioning of these sources to eventually be disposed of in a deep geological repository, or temporary interim storage.

When production of radium stopped at refineries in the 1960s, the estimated total amount of radium refined and placed into circulation was approximately a few kilograms [29]. There were a number of different radium sources that were manufactured at that time. However the IAEA was only concerned with those sources that were sealed and used in medical treatments and industry (Table 5). The unsealed sources such as various consumer products, and luminescent paints were not considered for collection and disposal in a repository. There was also a number of radium sources used in radium-beryllium (Ra-Be) neutron generators for research. Most sealed radium sources were in the form of salts (powders) to be used in luminescent materials, silver foils, and radium bromide solutions. In industrial sources, radium was used in items such as instrumentation dials, instrument calibrations, moisture detectors, fire detectors, lightning preventers, and static preventers [29]. Hospitals were one of the largest users of sealed radium capsules or radium needles for various cancer therapies, see Table 4 for capsule dimensions.

Due to radium's high chemical reactivity in air (as an alkaline earth metal), it was mixed with other compounds such as chlorides, bromides, sulfates, and carbonates, which led to a

mixture that was less chemically reactive. Table 4 indicates the most common types of medical radium sources used throughout the 1940s and 50s in various cancer treatments.

Table 4 Radium Needles

Radium needles used in medical brachytherapy. Adapted from [29].

Typical Dimensions of Medical Radium Sources									
	Platinum-Iridium Needles		Platinum-Iridium Tubes			Low -Content Platinum-Iridium Needles			Monel Metal Nasopharyngeal Applicator
Amount Ra-226 (mg)	5	10	5	15	25	1	2	3	50
Diameter (mm)	1.7	1.7	2.55	2.9	3.25	1.65	1.65	1.65	2.3
Length (mm)	14.5	19	21.7	22.5	29	27.7	44	60	21.5
Wall Thickness (mm)	0.5	0.5	1	1	1	0.5	0.5	0.5	0.3
Active length (mm)	7	12	15	15	15	15	30	45	-

Table 5 below indicates that the total estimated amount of radium sources within the U.S. is approximately 151 g. To look at that amount another way, it would take approximately 600 tons of U_3O_8 to extract 151 g of radium. Identified quantities in developing countries around the world as of the mid 1990s were about 4.5 TBq equating to 122 g, with an estimated total quantity of between 8 – 10 TBq (200 g – 250 g). The estimated number of sources in total is between 25,000 – 30,000 worldwide, or roughly a few kilograms [29].

Table 5 U.S. Radium Sources
Inventory of known sealed U.S. Radium sources.
Recreated data Adapted from [29].

This is a regeneration of the tables provided in the IAEA-TECDOC-886 report												
Medical Radium Sources									Non-Medical Radium Sources			
Activity Range GBq (mg)	**Needles % of Tot**	**Needles (mg)**	**Cells % of Tot**	**Cells (mg)**	**Plaques % of Tot**	**Plaques (mg)**	**Nasopharyngeal Appl. % of Tot**	**Nasopharyngeal Appl. (mg)**	**Ra - Be sources % of Tot**	**Ra - Be sources (mg)**	**Other sources % of Tot**	**Other sources (mg)**
≤ 0.004 (≤ 0.1)	0.01	0.01	-	-	0.6	0.007	-	-	10.5	0.36	38.4	6.13E-04
0.004 - 0.02 (0.1-0.5)	0.14	0.45	0.3	0.46			-	-	14	3.75	36	4.09E-03
0.02 - 0.04 (0.5-1)	2.2	0.73	5.4	0.61	0.6	0.89	-	-	11.6	9.49	3.5	4.87E-02
0.04 - 0.2 (1-5)	52.1	3.05	40.9	3.2	30.6	3.42	3.1	3.28	14	18.6	9.7	0.49
0.2 -0.4 (5-10)	40	7.72	37.4	7.57	41.9	8.18	4.6	9.44	2.3	100	10.2	3.17
0.4 - 2 (10-50)	5.3	15.4	15.8	17.6	24.1	17.5	81.5	44.7	17.4	302	0.4	54.90
2 - 4 (50-100)	0.13	71.7	0.2	66.9	2.2	61	10.8	67.4	4.7	678	1.3	464.00
>4 (>100)	0.04	118	-	-	-	-	-	-	25.5	1431.5	0.5	3210.00
Weighted Ave. (mg)	5.65		7.09		10.01		44.2		457		22.7	
Est. Total no. of Sources	7669		3355		320		65		86		1703	
Grand Tot.	151,153	*mg*										

5.5. Available Ra-226 Sources

There are two known sources of radium, one is the national inventory of spent radium sources as just discussed, and the other is the numerous waste tailing ponds from uranium mining / milling operations [31]. However, the old radium source material was also extracted from uranium mines, now existing as refined material in sealed sources.

The locations of these many spent radium sources are unknown. They would most likely reside at interim storage locations within the US or sources contained at the many individual locations of original use. If any radium sources were to be used for Ac-225 production methods, it may be necessary to arrange material transfer through a national regulatory body who is aware of these sources and their locations. When this production method is developed it will be the perfect outlet for the many facilities that maintain this material. The hazardous source material could be donated for research, testing, and ultimate consumption. A proposal for this is warranted and could incorporate a more developed production method.

The second source of Ra-226 resides within waste tailings of uranium milling operations. Following the milling of uranium ore stockpiles, waste material (that is not uranium) is pumped into specially prepared storage ponds for safe environmental management due to the

radioactivity levels of the waste slurry [32]. Much of this radioactivity is due in large part to the radium and its short-lived daughters as seen in (Fig 19).

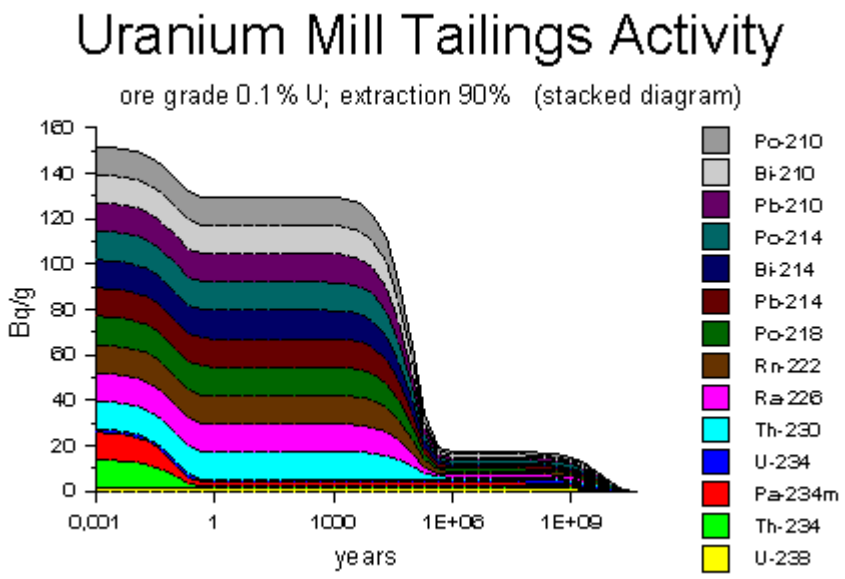

Figure 19 Uranium Mill Tailings Activity
Uranium Mill Tailings Activity of Ra-226 and Daughters of its Decay Chain, Public Domain [32]

If information about the total amount of uranium extracted from ore was available, it is possible to calculate an estimated amount of radium that could be extracted from waste ponds. A simple calculation of uranium activity from the tonnage of uranium (in U_3O_8 produced) provides the estimated activity of Ra-226, since it is in secular equilibrium with U-238.

5.6. Estimated Amount of Radium in Uranium Waste Tailings

This is a method for estimating the amount of Ra-226 that potentially exists within the waste tailings of uranium mining within the US. By knowing the total amount of U_3O_8 that has been recovered from mines in the US, one can calculate the estimated amount of radium residing within the tailings. As an example, the reported amount of U_3O_8 that was mined in the US spanning from 1993 – 2011 was 68,100,000 lbs [33]. The following calculations will show an activity and amount of radium for this reported amount of U_3O_8.

Weight percent of uranium in U_3O_8:

$$w_U = \frac{3\cdot(M_U)}{3\cdot(M_U)+8\cdot(M_O)} = \frac{3\cdot(238)}{3\cdot(238)+8\cdot(16)} \tag{5.1}$$

$$w_U = 0.848$$

$$Total\ Uranium\ Amount = (68{,}100{,}000\ lbs\ U_3O_8) \times (0.848) = 57{,}748{,}800\ lbs\ U$$

$$Total\ Est.\ Uranium\ Atoms$$

$$= 57{,}748{,}800\ lbs \cdot \left(\frac{453.59\ g}{1\ lb}\right) \cdot \left(\frac{0.6022 \times 10^{24}\ atoms/_{mol}}{238\ g/_{mol}}\right)$$

$$Total\ Est.\ Uranium\ Atoms, N_U = 6.628\ \times 10^{31} atoms$$

Since Ra-226 is in the decay chain of U-238, and U-238 has a significantly longer half-life, Ra-226 is in secular equilibrium with U-238. Therefore, the radium activity can be considered the same as that of U-238. Since this is a rough estimate, the weight percent of U-238 (~99.28%) in natural uranium was not accounted for in these calculations. Hence the activity of uranium is:

$$\alpha_U = \lambda_U N_U \tag{5.2}$$

$$\alpha_U = \lambda_U N_U = \left(\frac{0.693}{T_{\frac{1}{2},U}}\right) \cdot N_U = \left(\frac{0.693}{4.5 \times 10^9 yrs}\right) \cdot 6.627\ \times 10^{31} atoms$$

$$\alpha_U = \left(\frac{0.693}{4.5 \times 10^9 yrs}\right)\left(\frac{1yr}{3.156 \times 10^7 s}\right) \cdot 6.627\ \times 10^{31} atoms$$

$$\alpha_U = 3.2337 \times 10^{14}\ dis/_S = 323{,}700\ GBq$$

$$\alpha_U = 3.2337 \times 10^{14}\ dis/_S \left(\frac{1\ Ci}{3.7 \times 10^{10}\ dis/_S}\right) = 8739.7\ Ci$$

It is established that the specific activity of Ra-226 is 1.0 (Ci/g). Therefore, by the activity of uranium, the estimated amount of Ra-226 present is ~8740 g.

Estimates for the cost of extracting radium from waste ponds would need to be made in determining if this method is cost effective, given the current and future demand for Ac-225/Bi213 in research and medical uses. However, rather than radium extraction from

waste ponds, the most likely continuous source of radium in the future will be to extract radium directly from uranium mines. Current uranium milling facilities could be back-fitted to accommodate this additional extraction process, and new mills could simply have this included with their full scope of construction. The underground mining proposed in Chatham, Virginia would be the perfect fit for this.

6. Alpha and Gamma Attenuation

6.1. Alpha Particle Range

The range of alpha particles materials such as water, muscle, bone, and lead can be seen Figure 20. This provides a good picture as to the range of alphas in different areas of the human body in relation to Targeted Alpha Therapy (TAT). Therefore, if one is analyzing the effectiveness of alpha particles at killing a certain type of cancer in a certain tissue of the body, the Ac-225 alpha energy of 5.8 MeV can be used with this chart to obtain an estimated range in g/cm^2. If the range value is divided by the material density in g/cm^3, the linear range in cm can be calculated. This linear range can then be compared to the dimensions of various cancer cells that are targeted, to obtain a rough idea as to the extent of damage in surrounding cells.

A typical human cell size ranges from 2 – 120 microns in diameter or length [34].

The following conversion helps put these sizes in perspective.

$$1\ micron = 1\ \mu m = 10^{-4} cm$$

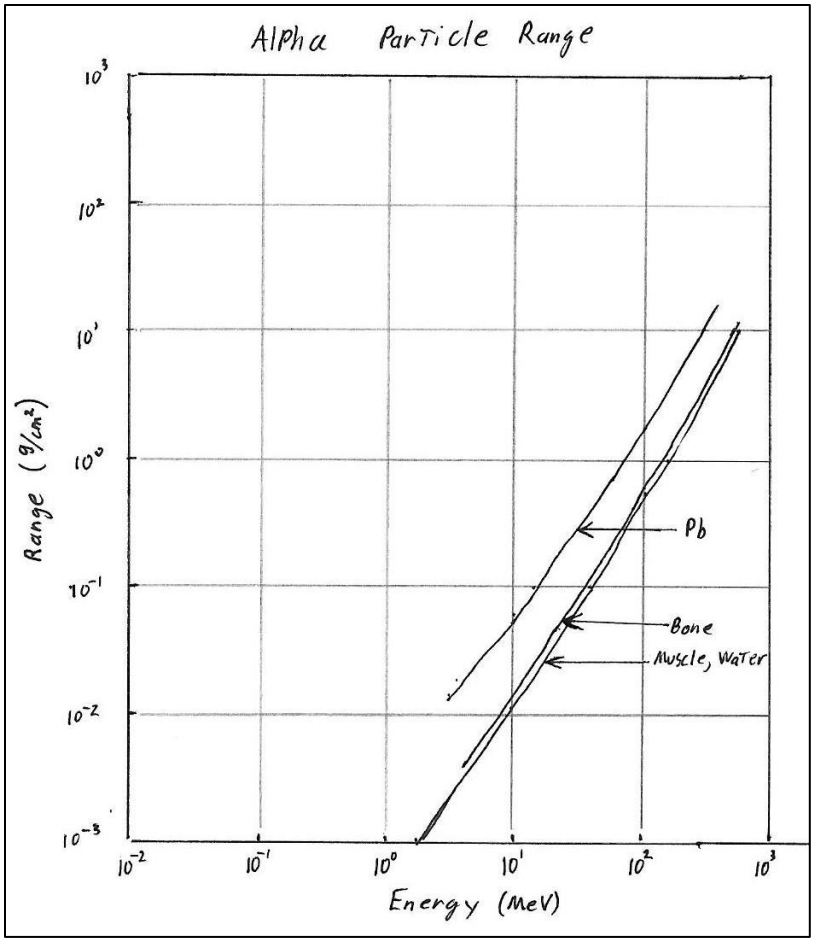

Figure 20 Ranges of Alpha Particles
Ranges of alpha particles in water, muscle, bone, and lead, expressed in g/cm^2.
Adapted by, [Turner, et. al. 2007, pg 129] [8].

The effectiveness of alpha therapy can be better understood by Figure 20 and Table 6, where the decay alpha energy of 5.8 MeV was used to interpolate the alpha-particle range (g/cm^2) in human body tissues. The range density estimates were divided by the material density to obtain the linear range (cm) traversed across each medium. The upper and lower range of typical cell diameters were divided by the linear range to obtain an estimate of how far 5.8 MeV alpha particles travel while delivering their energy to the surrounding cells. It appears that the majority of energy is deposited within the immediate cell area, with a number of the surrounding cells being affected in tissues of smaller cell diameter less that ~60 microns. Other radioisotopes within the Ac-225 decay chain would be similar in their (LET) and range with alpha energies for Francium-221 (Fr-221), Astatine-217 (At-217), and Bi-213 at 4.9, 7.1, and 5.9 MeV respectively. However, Bi-213 decays by giving off 5.9 MeV alphas only 2% of the time, where 98% of the time it undergoes β^- decay to

Polonium-213 (Po-213). Po-213 emits 8.4 MeV alphas 100% of the time, hence this is the isotope utilized in TAT. A new company, Actinium Pharmaceuticals Inc. has also been developing the appropriate delivery methods for using a number of medical isotopes to include use of Ac-225 directly in the body [6].

Table 6 Alpha Particle Range in Cells

Alpha particle range comparison in typical human tissue cells to their diameters. These values were calculated by interpolation of Figure 18 with material densities and typical cell diameters obtained from, [34].

	Cell Diameters Traversed				
				Ac-225 α 5.8 (MeV)	
	Density, ρ (g/cm3)	Est. Range (g/cm2)	Linear Range (cm)	(LOW)	(HIGH)
H20	1	0.005	0.00500	0.42	25
Muscle	1	0.0055	0.00550	0.46	28
Bone	1.9	0.007	0.00368	0.31	18
Pb	11.3	0.02	0.00177	0.15	9

6.2. Photon Attenuation In Matter

There are several interaction mechanisms by which photons are attenuated in matter, photoelectric absorption, Rayleigh scattering, Compton scattering, and pair production. Additionally, there are a host of other interaction methods at higher photon energies to include photo-fission (γ,f), photo-neutron reactions for single (γ,n), double (γ,2n) type, and photo-proton reactions (γ,p) to name just a few. As previously discussed the photo-neutron reaction is used for this production method, and is accounted for by the photo-neutron cross-section of Ra-226. While this was considered in the yield equation (Equation 2.3), the other interaction mechanisms were not accounted for due to the thin sample size that was assumed for this equation. The following plot in Figure 20 indicates the total mass attenuation coefficient for radium, which is simply the sum of the individual interaction probabilities as shown in the following formula, considering photoelectric absorption, Rayleigh scattering, Compton scattering, and pair production.

$$\frac{\mu}{\rho} = \frac{\tau}{\rho} + \frac{\sigma_R}{\rho} + \frac{\sigma}{\rho} + \frac{\pi}{\rho}$$

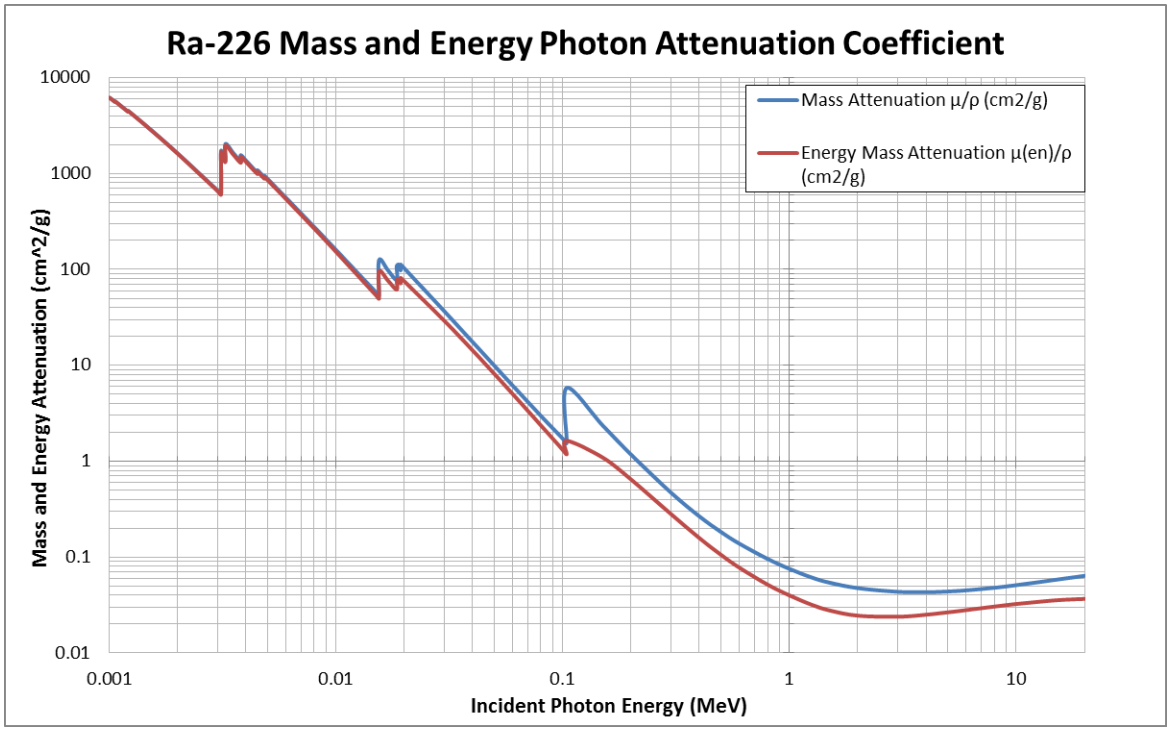

Figure 20 Mass and Energy Attenuation of Photons in Radium
Mass and Energy Attenuation Coefficients of Photons in Radium. This plot was generation from tabulated data from NIST and Adapted by [14].

Table 7 Radium Attenuation Data

This data was adapted from, public domain [14].

Photon Attenuation Results for Radium											
Photon Energy (MeV)	Mass Attenuation (cm2/g)	Linear Attenuation (cm-1)	Mean Free Path (cm)	Fraction of Normally Incident Photons Available for Photo-neutron Interactions in Varying Radium Target Thicknesses (cm)							
				0.1	0.5	1	2	3	5	10	20
0.1000	1.712	8.56000	0.11682	0.42486	0.01384	0.00019	0.00000	0.00000	0.00000	0.00000	0.00000
0.1039	1.560	7.80000	0.12821	0.45841	0.02024	0.00041	0.00000	0.00000	0.00000	0.00000	0.00000
0.1039	5.826	29.13000	0.03433	0.05431	0.00000	0.00000	0.00000	0.00000	0.00000	0.00000	0.00000
0.1500	2.355	11.77500	0.08493	0.30805	0.00277	0.00001	0.00000	0.00000	0.00000	0.00000	0.00000
0.2000	1.172	5.86000	0.17065	0.55655	0.05340	0.00285	0.00001	0.00000	0.00000	0.00000	0.00000
0.3000	0.470	2.34800	0.42589	0.79073	0.30913	0.09556	0.00913	0.00087	0.00001	0.00000	0.00000
0.4000	0.266	1.33100	0.75131	0.87538	0.51402	0.26421	0.06981	0.01844	0.00129	0.00000	0.00000
0.5000	0.182	0.90850	1.10072	0.91315	0.63492	0.40313	0.16251	0.06551	0.01065	0.00011	0.00000
0.6000	0.138	0.69150	1.44613	0.93319	0.70769	0.50082	0.25082	0.12562	0.03151	0.00099	0.00000
0.8000	0.096	0.47895	2.08790	0.95323	0.78704	0.61943	0.38370	0.23768	0.09120	0.00832	0.00007
1.0000	0.075	0.37675	2.65428	0.96303	0.82830	0.68609	0.47072	0.32295	0.15202	0.02311	0.00053
1.2500	0.061	0.30705	3.25680	0.96976	0.85768	0.73561	0.54113	0.39806	0.21540	0.04640	0.00215
1.5000	0.054	0.27075	3.69344	0.97329	0.87339	0.76281	0.58187	0.44386	0.25827	0.06670	0.00445
2.0000	0.048	0.23750	4.21053	0.97653	0.88803	0.78860	0.62189	0.49042	0.30498	0.09301	0.00865
3.0000	0.043	0.21700	4.60829	0.97853	0.89718	0.80493	0.64791	0.52152	0.33790	0.11418	0.01304
4.0000	0.043	0.21500	4.65116	0.97873	0.89808	0.80654	0.65051	0.52466	0.34130	0.11648	0.01357
5.0000	0.044	0.21895	4.56725	0.97834	0.89630	0.80336	0.64539	0.51848	0.33462	0.11197	0.01254
6.0000	0.045	0.22500	4.44444	0.97775	0.89360	0.79852	0.63763	0.50916	0.32465	0.10540	0.01111
8.0000	0.048	0.23950	4.17537	0.97633	0.88714	0.78702	0.61940	0.48748	0.30195	0.09117	0.00831
10.0000	0.051	0.25500	3.92157	0.97482	0.88029	0.77492	0.60050	0.46533	0.27943	0.07808	0.00610
15.0000	0.058	0.29050	3.44234	0.97137	0.86481	0.74789	0.55934	0.41832	0.23398	0.05475	0.00300
20.0000	0.064	0.31915	3.13332	0.96859	0.85251	0.72677	0.52819	0.38387	0.20276	0.04111	0.00169

The data shown above in Table 7 was calculated from mass attenuation μ/ρ (cm^2/g) data for Ra-226 supplied by the National Institute of Standards and Technology (NIST) [14]. The following calculations show how the linear attenuation μ, mean free path λ, and fraction of attenuated photons are calculated from the given mass attenuation data and varying sample thicknesses.

Linear Attenuation μ: Example Calculation at *8 MeV*, see Table 7 above.

$$\mu = \left(\frac{\mu}{\rho}\right) \cdot \rho_{Ra-226} = \left(0.048\ \frac{cm^2}{g}\right) \cdot \left(5\ \frac{g}{cm^3}\right) = 0.24\ cm^{-1}$$

Mean Free Path λ: Example Calculation at *8 MeV*, see Figure 21 below.

$$\lambda = \frac{1}{\mu} = \frac{1}{0.24\ cm^{-1}} = 4.17\ cm$$

Fraction of attenuated photons $e^{-\mu x}$: Example Calculation at *8 MeV* with *1 cm* thick target, see Table 7 above.

$$\frac{N(x)}{N_o} \textit{ is the fraction of normally incident uncollided photons passing through an absorber material of thickness } x.$$

$$\frac{N(x)}{N_o} = e^{-\mu x} = e^{-(0.24\ cm^{-1})\cdot 1cm} = 0.787$$

Therefore, this calculations shows that ~78.7% of 8 MeV photons are un-attenuated by a 1 cm thick radium sample, and are therefore available for photo-neutron interactions.

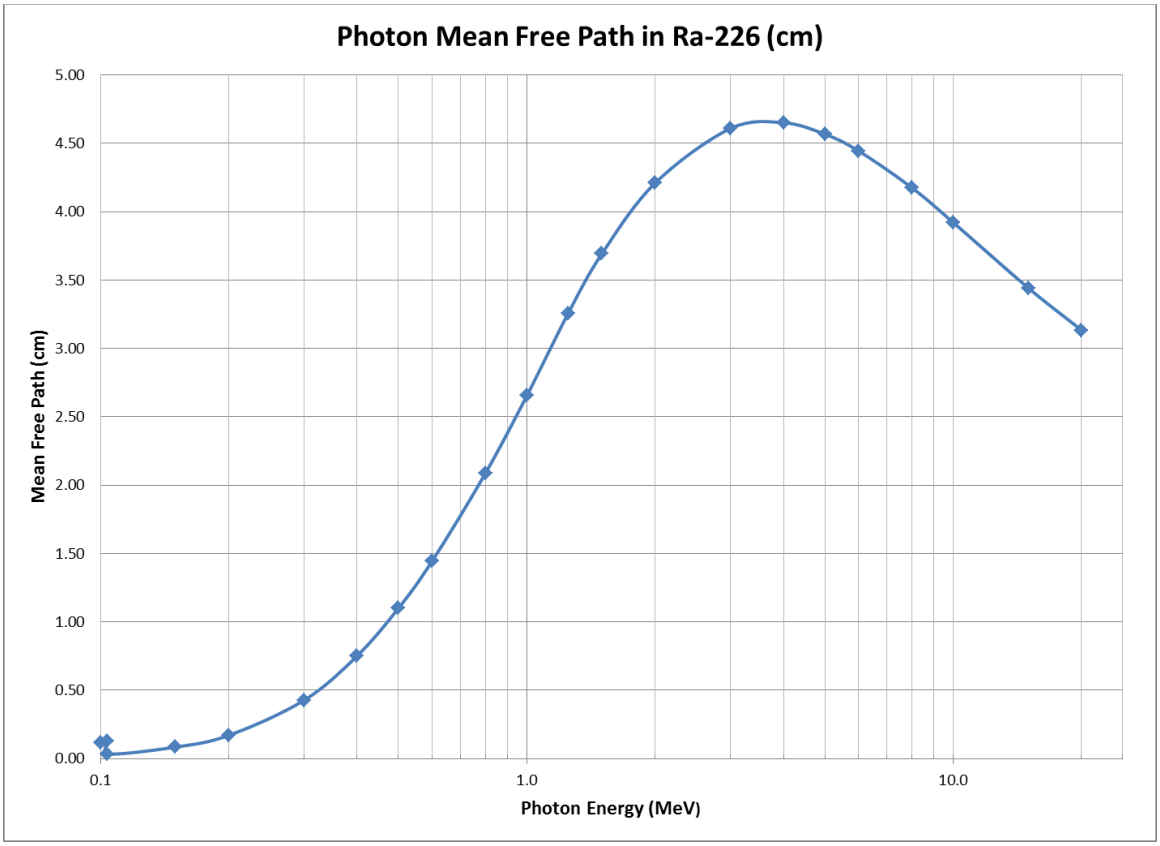

Figure 21 Mean Free Path of Photons in Radium
Mean Free Path due to total attenuation effects, of Photons in Radium over varying energies. Data converted from mass attenuation data from NIST [14].

It is easier to understand the interaction effects of high energy photons on a radium sample thickness by examining their mean free path λ. As can be seen from Figure 21 above, the mean free path of photons due to total attenuation effects in radium ranges from ~4.5cm (at 6 MeV) to ~3.3 cm (at 18 MeV). More precise values can be found in Table 7.

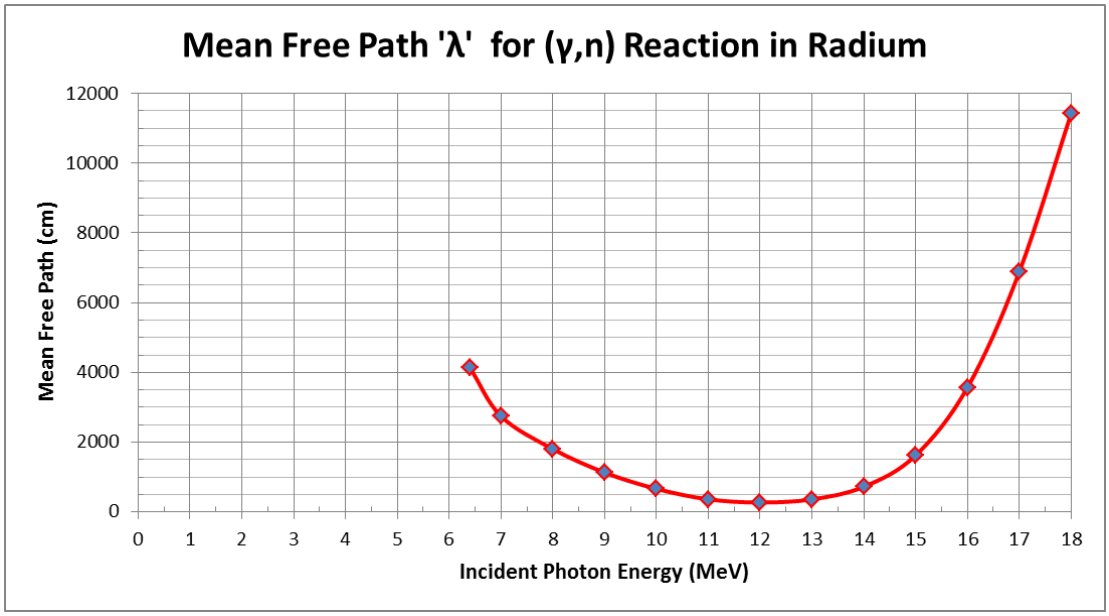

Figure 22 Mean Free Path of Photons in Radium
Mean Free Path due to ONLY Photon-neutron reactions in Radium over varying energies. Plot generated using the atom density of pure radium and its' photo-neutron cross-section.

By comparison, Figure 22 (above) indicates the mean free path $\lambda = {}^{1}/_{N_{Ra}\sigma_{(\gamma,n)}}$ of photons through radium by only considering photo-neutron interactions. As can been seen, the path length for this reaction type is several orders of magnitude larger than the mean free path for total attenuations. Figure 22 further indicates that the optimal energy range for Ra-225 production is between 11 and 13 MeV, where the mean free path is at a minimum of ~270 cm at 12 MeV.

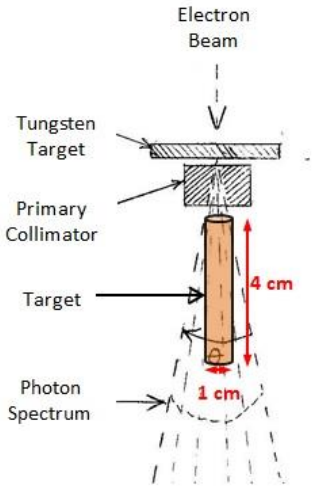

Figure 23 Arrangement of a 20 Ci 4 cm thick Radium Sample

It is also important to note that this attenuation study was performed with mass attenuation data for pure radium, versus radium compounds such as radium-bromide and radium-chloride, which were discussed in chapter 5. Since the atom densities of radium compounds are slightly less than pure radium, a slightly larger sample thickness would be required to achieve the same fraction of attenuation as that of pure radium. However, for consistency, pure radium samples were simulated as will be discussed in section 7. It is apparent from the mean free path and attenuation characteristics of photons in radium, that a sample of considerable thickness would be necessary for efficient production. However, a study must be performed to find the optimal sample thickness at which production is most efficient. This was evaluated in Scenario 4 of section 7. For a sample of extended thickness, it would most likely be a right cylinder arranged in the photon spectrum as depicted in figure 23 above. However, a sample size like the one depicted above could be in the 10 to 20 Ci range of activity, raising concerns over the available amounts of radium, not to mention the much larger radiation hazard it would pose. The production facility would most likely need to have hot-cells to properly manage radium targets this large.

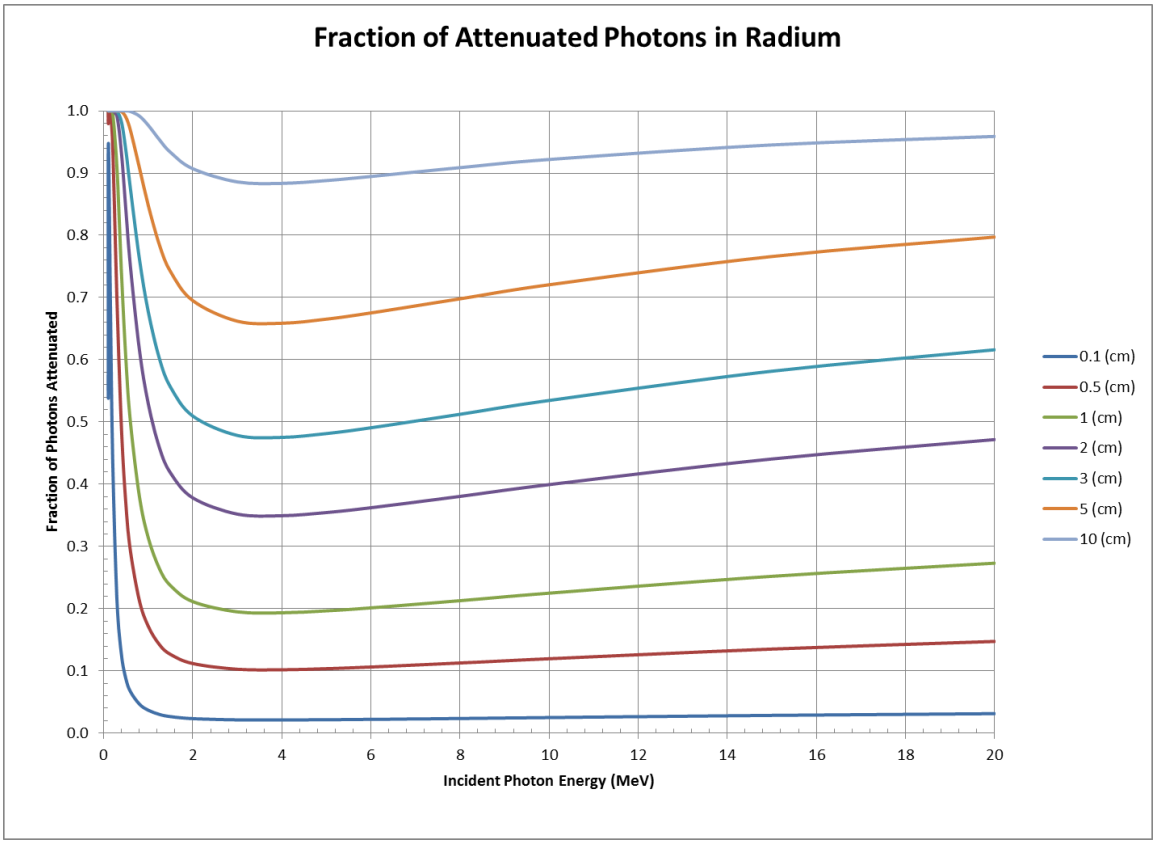

Figure 24 Fraction of Attenuated Photons in Ra-226
Fraction of Attenuated Photons in Varying Ra-226 Sample Thicknesses, Over Energies of 0.1 to 20 MeV. Data calculated using mass attenuation data provided by NIST, adapted by [14]. Raw data is tabulated in Appendix D.

Figure 24 is simply the inverse of Figure 5, showing the fraction of incident photons that are attenuated by the radium sample thickness, where the remaining photons then have the likelihood of interacting by photo-neutron reaction to produce Ra-225 atoms.

Evaluation of Tungsten Target Attenuation

Given the energy range of 6 – 18 MeV, and with a tungsten density of

$$\rho = 19.25\ {}^{g}/_{cm^3}$$

The following attenuation behavior was found:

- For a 1mm thick tungsten LINAC target, the fraction of attenuated photons ranges between approximately 7.7% and 10%.
- For a 5mm thick tungsten LINAC target, the fraction of attenuated photons ranges between approximately 33% and 42%.

  Considering most LINACs have a tungsten target thickness on the order of a few millimeters, it is clear that the thickness would play an important role in the photon intensity of the Bremsstrahlung spectrum. In this research the photon data being used was most likely measured below the tungsten target and already considers these attenuation effects induced by the tungsten target, whatever its thickness may have been. Therefore, these attenuation effects will not be considered in the yield model discussed in section 7. A precise knowledge of LINAC target thickness would need to be known to perform back calculations of electron beam current from photon spectrum data, as was first intended by this research. A full set of attenuation data for tungsten can be found in Table 10 of Appendix D.

Evaluation of Platinum Attenuation

Given the energy range of 6 – 18 MeV, and with a platinum density of

$$\rho = 21.45\ {}^{g}/_{cm^3}$$

The following attenuation behavior was found:

- For a *1mm* thickness of platinum (used in most radium needle cladding), the fraction of attenuated photons ranges between approximately *8.8%* and *12%*.
- For a *5mm* thickness of platinum, the fraction of attenuated photons ranges between approximately *37%* and *46%*.

  This attenuation information can be used to provide a correction factor to the photon rate data incident upon radium needles. With a needle shell thickness of approximately 1 mm, it could be said that on average ~11% of the photons (above 6.4 MeV) striking the

radium needle, are no longer available for photo-neutron interactions with the radium inside. This correction factor was applied to the yield calculation in scenario 1 discussed in section 7. This platinum attenuation data can be utilized for future experiments to appropriately account for photon losses in the paricular sample being irradiated, that is of course if it has platinum as a containment material and its thickness in known. The full set of attenuation data for platinum can be found in Table 11 of Appendix D.

7. Yield Results

Using the TENDL photo-neutron cross-section data for Ra-226 calculations were made to determine the impact on the yield calculations due to the different cross-sections and to account for attenuation in thicker radium targets. Throughout this section four yield scenarios and a parametric uncertainty study will be presented. The first compares yields using Melville's first experiment criteria. Where a 40 mCi radium sample was irradiated for 175 minutes, with a sample thickness of ~1mm, and an area correction accounting for the small cross sectional area of the radium needle (0.132 cm^2) placed in the 9.3 cm^2 photon field. The second scenario irradiates a 1 cm^3 (5 Ci) pure radium sample for 1 hour. This scenario assumes the sample is placed in the photon field such that all photons are normally incident upon the sample, with the sample thickness set to 1 cm. The third scenario compares Ra-225 yields by irradiation of a 2 Ci radium sample for 10 hours. A factor of 8 is also applied to the Ra-225 yield rate results to account for a doubling effect of the three LINAC parameters. A comparison is made to Melville's model that irradiates 100 (20 mCi) needles, which would account for a total sample of 2 Ci. Therefore, a 2 Ci sample was specified for scenario three with a sample thickness set to 1 cm. The assumption is again that the sample is located such that all photons intersect with the sample area. The fourth scenario involved numerous MATLAB® iterations to evaluate the relationship between sample thickness and Ra-225 yield, using the base case values for photon flux and cross-section. This scenario predicts the Ra-225 yield for a 20 Ci Ra-226 sample that is 4 cm thick, with a 1 cm^2 cross-sectional area normal to the photon field. The final part of this section is a parametric study of the yield equation parameters, in an effort to show Ra-225 yield effects of upper and lower uncertainty limits applied to each parameter.

7.1 Yield Scenario 1

This scenario was performed to evaluate the change in Ra-225 yield predicted by this model to that reported by Melville in his first experiment. The first experiment used an 18 MeV LINAC to irradiate two 20 mCi radium needles at a distance of 49 cm from the tungsten target for a time of 175 minutes. From dimensional knowledge of the photon spectrum, as previously shown in Figure 10 of section 3.2, it was determined that at 49 cm the cross-sectional area of the photon field is ~9.3 cm^2. The active radium needle dimensions were also known for the 20 mCi needles (see Table 4). The active radium in the needle was ~1 mm thick while the active cross-sectional area of radium presented by both needles was ~0.264 cm^2. Therefore, a ratio of sample area to photon field area was used as a correction factor to estimate the photon flux (photons/cm^2/s) on the needle. The yield for Melville's experiment was calculated in a couple ways. First by measurement of the Ra-225 spectra over a number of weeks following irradiaton, and also by geometrical considerations using the measured count rate of Ra-225 and detector dimensions. Doing so resulted in an average yield of 64 +/- 17 µCi of Ra-225. Further details for how Melville arrived at this yield can be found in the following published articles [2] [3]. His model produced results that were also consistent with the 64 µCi measured yield.

The MATLAB® model used in this research incorportated the same criteria. The irradiation time was set to 175 min, with a 40 mCi sample specified, and a sample thickness set to 1 mm. The ratio of sample area to photon field area was applied to the yield results and will be shown below. In addition to these criteria, a modified yield equation was utilized in this scenario and all following scenarios to account for photon attenuation effects due to varying radium thickness. The cross-section term $\sigma_{TENDL}(E)$ represents the TENDL Ra-226 Photo-neutron cross-section data.

$$Y = N \cdot t \cdot \int_{6.4}^{18} \phi(E) \cdot \sigma_{TENDL}(E) \cdot \left(e^{-(0.0068 \cdot E + 0.1855)t}\right) dE$$

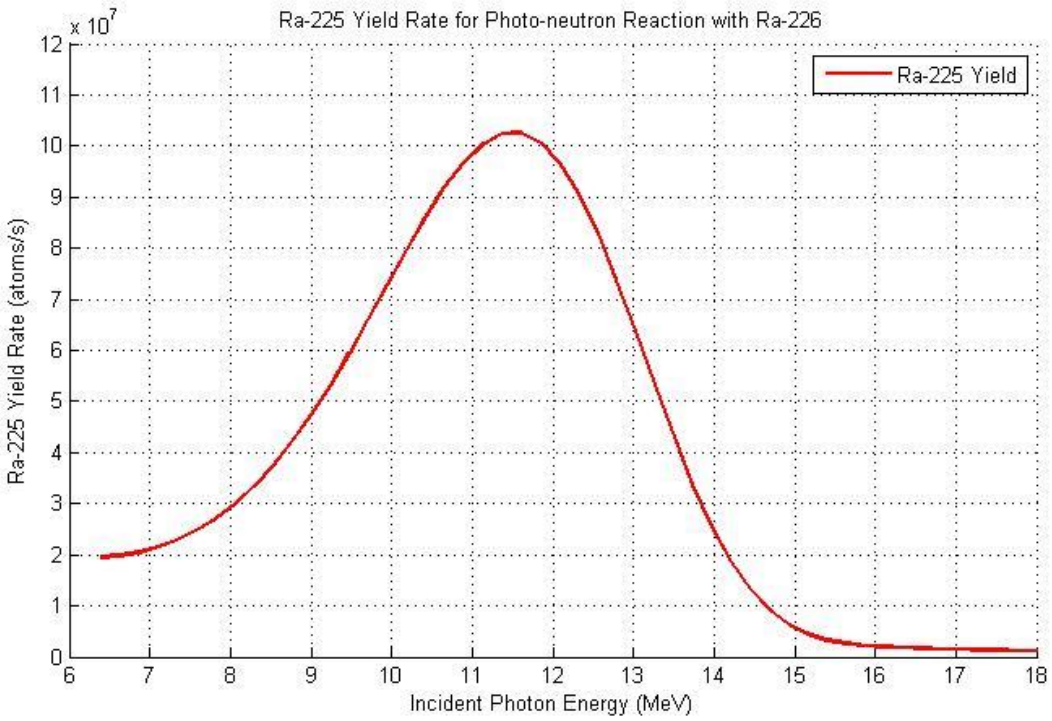

Figure 25 Scenario 1 Ra-225 Yield Rate
Calculation of a 40mCi sample for 175 min, thickness set to 0.1 cm to mimic the radium diameter within a 20 mCi radium needle.

The resulting Ra-225 yield (obtained from the area under the curve in Figure 25 above) is 72.7 µCi, however, the 11% photon attenuation due to the 1 mm platinum needle shell should be applied. This reduces the yield to 64.7 µCi. The area ratio correction factor can additionally be applied as shown here,

$$\frac{Sample\ area\ (cm^2)}{Photon\ Field\ area\ (cm^2)} = \frac{0.264}{9.3} = 0.084$$

$$64.7\ \mu Ci\ \times 0.084 = 5.4\ \mu Ci$$

Giving a total estimated Ra-225 yield of 5.4 µCi, with a potential to extract 2.4 µCi Ac-225 following an 18 day decay of Ra-225. This small yield of 5.4 µCi is 91.5% less than the 64 +/- 17 µCi yield presented in Melville's work. However, one must address the question of why the model used here reports a much lower yield, given what is believed to be a similar model setup. While Melville did measure the count rates of Ra-225's 40 keV gamma peak, there was a 34% uncertainty associated with that measurement. He additionally mentions that a good count rate for Ac-225, and its daughter Fr-221 could not be measured due to the high radium background. There are also three main differences between Melville's model

and this model. The first is that there is a 75% difference between the total number of photons/s in the spectrum that Melville used, versus the total photon rate calculated using the given photon spectrum curve, see Figure 7. The second model difference is derived from the reduced magnitude of the TENDL Ra-226 cross-section data as compared to Bi-209 data (half the magnitude), see Figure 17. TENDL data is from the predictive model code TALYS that may also have some inherent uncertainty. The third model difference is the radium attenuation term incorporated into the yield equation (see section 3.2 and Appendix A), further reducing yields. All of these contributors leading to a reduced yield must ultimately be experimentally evaluated to determine their impact. It will also be necessary to irradiate much larger samples, to produce a significant amount of Ra-225 so that an Ac-225 count rate can be accurately measured.

7.2 Yield Scenario 2

This scenario was conducted as a comparison to one performed in Melville's work. A 1 cm^3 radium sample representing 5 Ci worth of Ra-226 was irradiated for 1 hour. An assumption was also made that the sample is located such that all photons above 6.4 MeV in the Bremsstrahlung spectrum intersect with the cross-sectional area of the radium. The sample thickness was set to 1 cm in this research model. With this set of criteria, the following yield rate comparison was obtained in Figure 26.

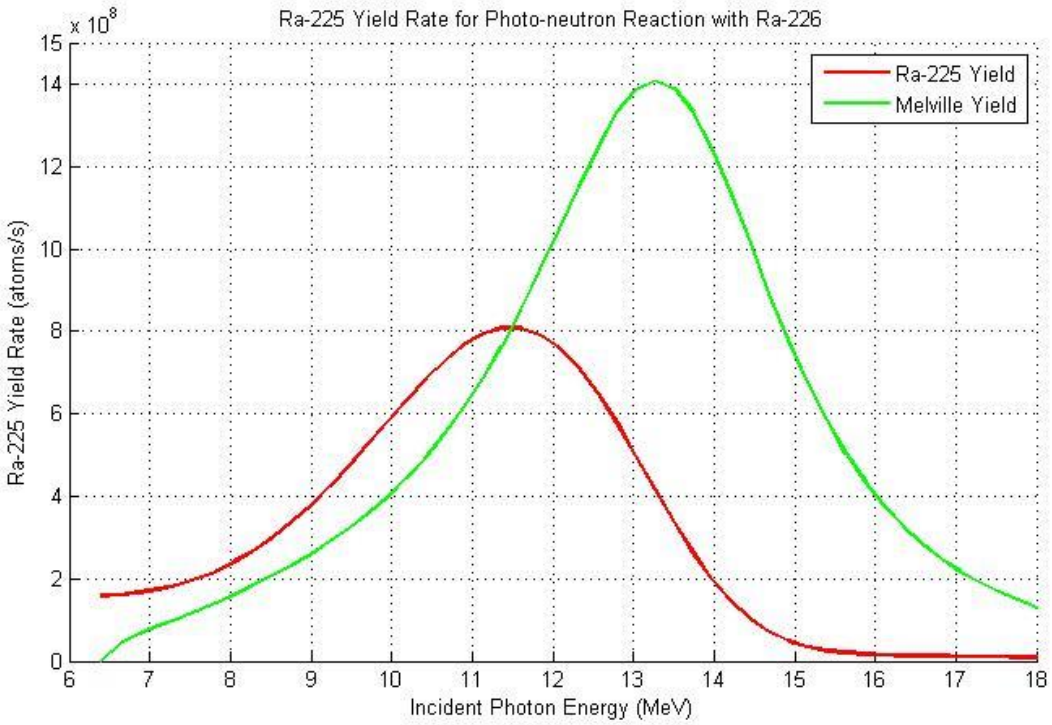

Figure 26 Scenario 2 Ra-225 Yield Comparison
Ra-225 Yield comparison between Melville's Cross-section data and TENDL Ra-226 Cross-section data, above 6.4 MeV.

The Ra-225 yield rate obtained from Melville's model was 1.45 mCi/hr, where this model calculated a yield rate of 0.197 mCi/hr (area under red curve, Fig 26). The yield of 0.197 mCi is 86.4% less than the 1.45 mCi yield produced by Melville's model. This reduction in yield is most likely due to using the smaller TENDL photo-neutron cross-section data, and the addition of sample thickness attenuation effects. A total yield rate for each curve shown above was calculated within MATLAB® using a definite integral function over the energy range 6.4 – 18 MeV. A manual calculation to validate the MATLAB® curves and output values is shown in Appendix A, and were found to be valid, given the TENDL data and model criteria. Figure 27 below shows an expanded view of the red curve of Figure 26 above.

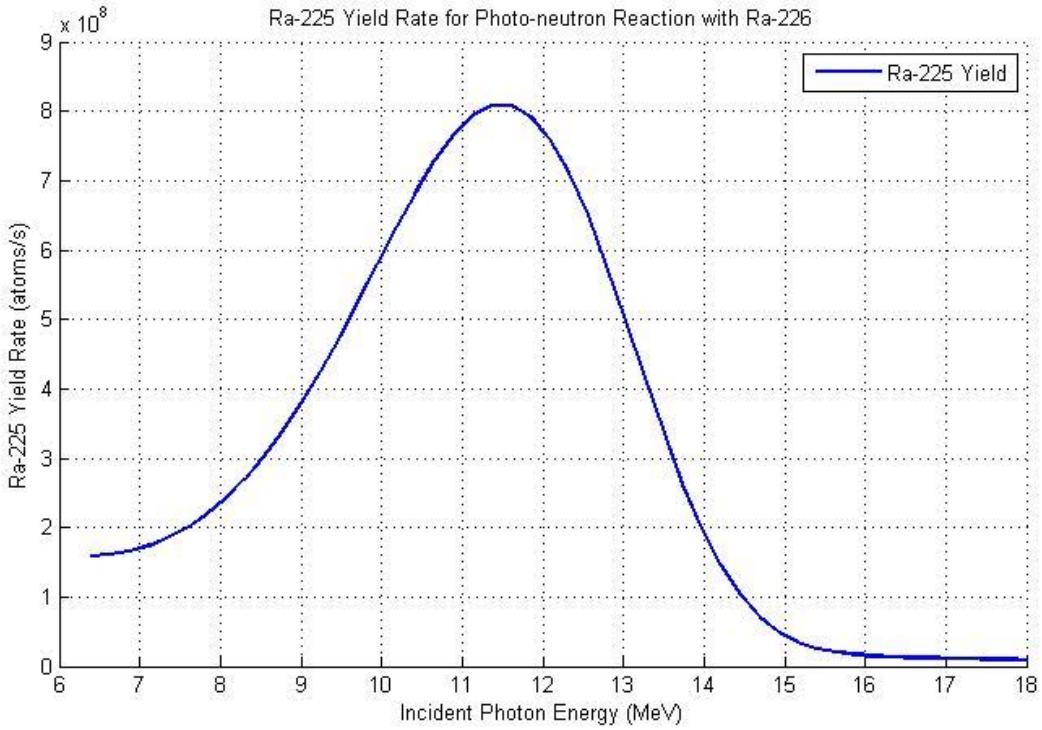

Figure 27 Scenario 2 Ra-225 Yield
Irradiation of a 5 Ci sample for 1 hour 1 cm^3, thickness set to 1 cm. Same as Red curve in the Figure 26 yield comparison. Ra-225 yield is 0.197 mCi, while after 18 day decay the Ac-225 Yield extraction potential is 0.0868 mCi.

7.3 Yield Scenario 3

This scenario was intended to estimate the potential yield gained from increasing the LINAC electron beam parameters, and by lengthening irradiation time from 1 hr to 10 hours. The sample size proposed in Melville's model was 100 (20 mCi) radium needles, making a total sample amount of 2 Ci. The sample specified in this model is set at 2 Ci with a thickness of 1 cm. The important consideration in this model is the dimensional layout of 100 (20 mCi) radium needles referred to by Melville [1]. A solid 2 Ci pure radium sample would make up a much smaller volume than 100 stacked needles. Additionally, the three electron beam parameters, average beam current, pulse length, and pulse frequency were hypothetically doubled, equating to a potential factor of 8 increase in photon yield rate. With these criteria, and the assumption once again that all photons in the spectrum are incident upon the sample, the predicted Ra-225 yields were as follows.

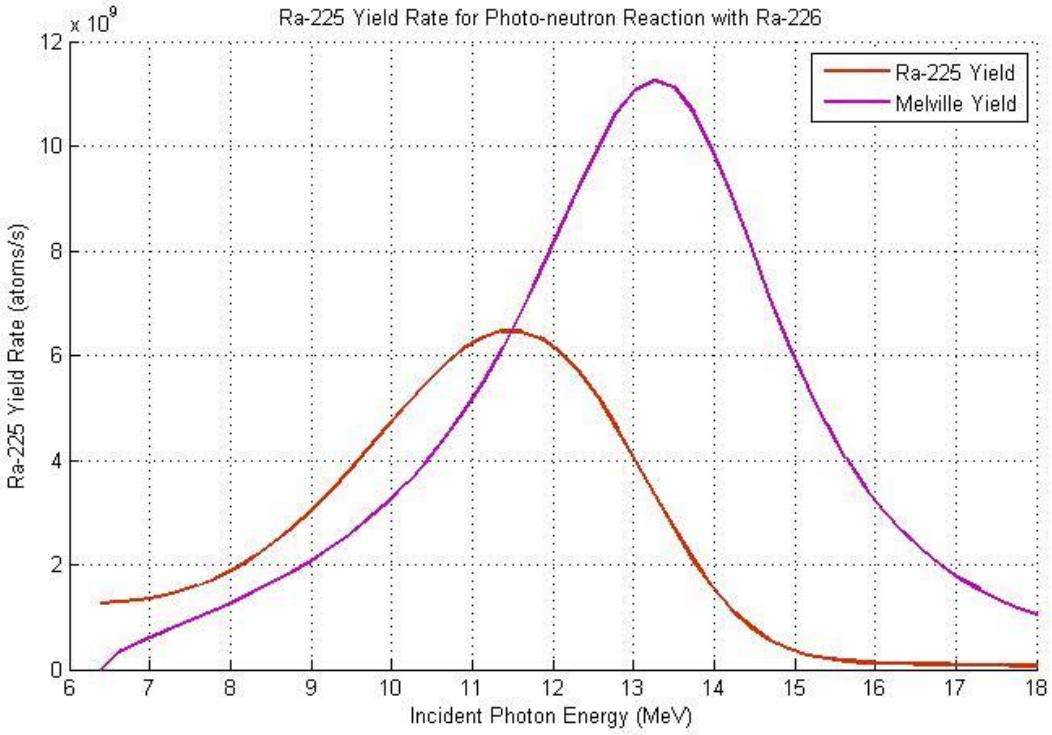

Figure 28 Scenario 3 Ra-225 Yield Comparison
Irradiation of a 2 Ci sample for 10 hours, with a thickness set to 1 cm, and a factor 8 increase in LINAC parameters.

Melville's Model (Purple Curve, Fig 28):

Ra-225 Atom Yield Rate – 5.289 x 10^{10} atoms/s

Ra-225 Yield – 28.07 mCi

Ac-225 Yield – 12.35 mCi

Predicted Yield Model (Maroon Curve, Fig 28):

Ra-225 Atom Yield Rate – 2.9726 x 10^{10} atoms/s

Ra-225 Yield – 15.78 mCi

Ac-225 Yield – 6.9432 mCi

The predicted Ra-225 yield of 15.78 mCi (area under maroon curve, Fig 28) is 43.78% less than the re-simulated Melville yield of 28.07 mCi (area under purple curve, Fig 28). However, Melville presented a resulting yield of 88 mCi for this model. This is approximately 82% more than the 15.78 mCi yield obtained here using TENDL Ra-226 cross-section data. There is an additional loss factor that is not included in this model, and that is the attenuation affects from the 100 platinum needles. Given the yields from this type

of production run, it is clear that additional enhancements in LINAC beam current and sample thickness would be required to make this production method as efficient as possible.

7.4 Yield Scenario 4

In this scenario a number of iterations were performed in MATLAB® in an effort to find a correlation between sample thickness and Ra-225 yield, given the newly applied attenuation correction factor. Estimated yields were obtained by maintaining a consistent set of model criteria while adjusting sample thickness and sample activity. The irradiation time was set to 10 hours, with no enhancement in LINAC parameters applied. The sample thickness and thus sample activity was varied over a range of thicknesses, as shown in Table 8 below.

Table 8 Ra-226 Sample Thickness to Yield Evaluation Data

Ra-226 Sample Activity (mCi)	Ra-226 Sample Thickness (cm)	Ra-225 Yield (mCi)	Ra-225 atoms/s	# of Ra-225 atoms generated
500	0.1	0.2493	4.696E+08	1.691E+13
2500	0.5	1.1233	2.116E+09	7.618E+13
5000	1	1.9725	3.716E+09	1.338E+14
10000	2	3.0417	5.729E+09	2.062E+14
15000	3	3.5184	6.620E+09	2.383E+14
20000	4	3.6182	6.816E+09	2.454E+14
25000	5	3.4889	6.572E+09	2.366E+14
30000	6	3.2302	6.084E+09	2.190E+14
35000	7	2.9080	5.478E+09	1.972E+14
40000	8	2.5650	4.832E+09	1.740E+14
45000	9	2.2270	4.196E+09	1.511E+14
50000	10	1.9100	3.599E+09	1.296E+14

Ra-225 yield results were plotted against sample thickness; this is shown in Figure 29 below. This correlation between thickness and yield indicates a sample thickness of ~4 cm would provide the optimal yield efficiency. Thicknesses beyond 4 cm do not appreciably contribute to the overall yield due to the attenuation effects at higher thicknesses. In the same fashion, thicknesses below 4 cm do not offer enough radium atoms per cm^2 for the incident photons to interact with, given the large photo-neutron mean free path at energies

between 6 and 18 MeV (see Figure 22). An optimized sample arrangement of 4 cm is depicted in Figure 30.

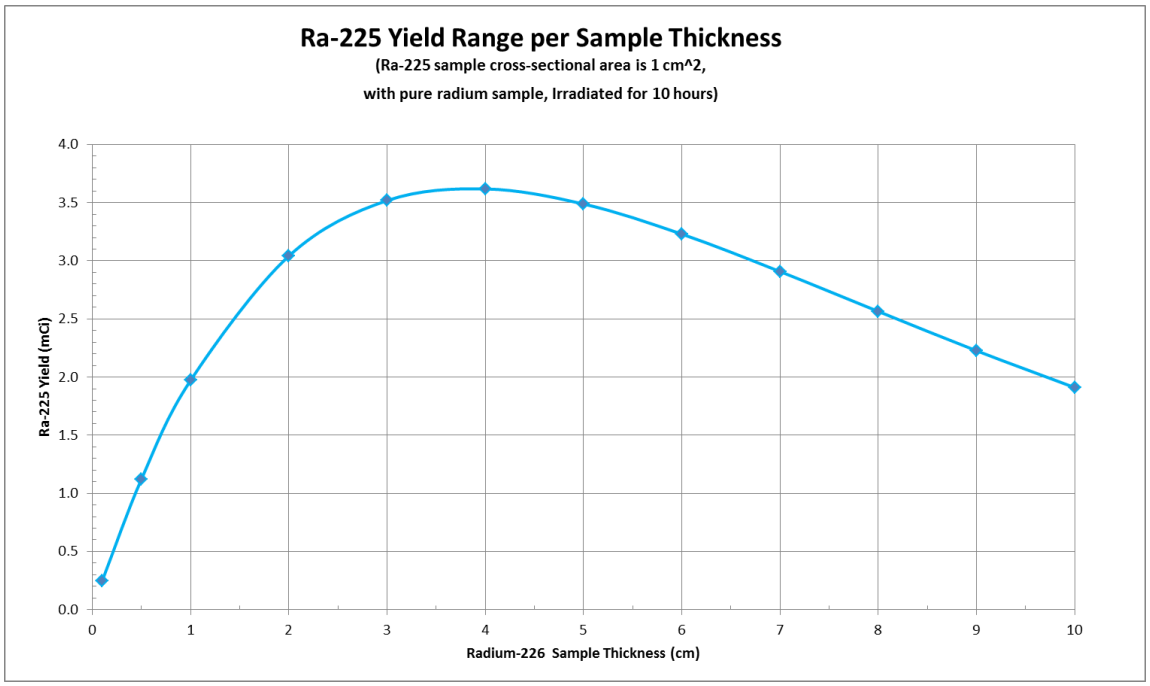

Figure 29 Ra-225 Yield to Sample Thickness
Ra-225 yield, given varying sample thicknesses, a 10 hour irradiation time, and no LINAC parameter enhancements.

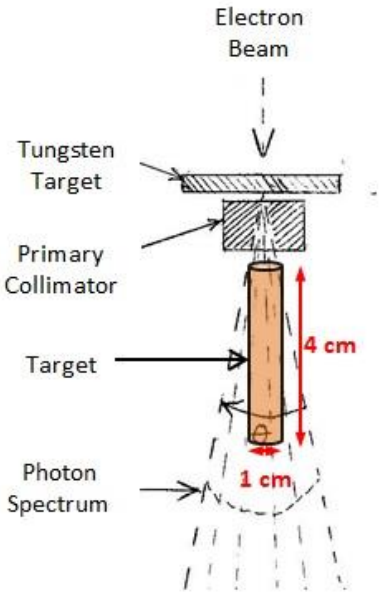

Figure 30 Scenario 4 Ra-226 Sample Schematic
Sample Arrangement for the Irradiation of a 20 Ci Sample.
Sample and LINAC schematic are not to scale.

7.5 Parametric Study of Yield Equation Parameters

This study will focus on evaluating the yield equation parameters such as thickness *t*, photon flux ϕ, and photo-neutron cross-section σ, to determine a best case yield and worst case yield given arbitrary uncertainty bounds for each. Refer to equation 2.4 for these parameters. The thickness term is both present with the atom density term and within the photon attenuation term. Therefore the uncertainty limits of both photon flux and photo-neutron cross-section parameters will be evaluated over a range of thicknesses.

An arbitrary uncertainty range of +/-15% was applied to the photon flux ϕ data. This range is meant to account for any uncertainty that may exist in the high energy approximation formula (Equation 2.2) used to calculate Bremsstrahlung efficiency. The baseline efficiency was evaluated at 40 +/-15%. A number of MATLAB iterations were made to calculate the upper and lower yield bounds on a per thickness basis. The photon flux uncertainty is shown in Figure 31 below. It was found that there is a linear relationship between photon flux and Ra-225 yield, such that a +15% uncertainty equates to a +15% yield increase.

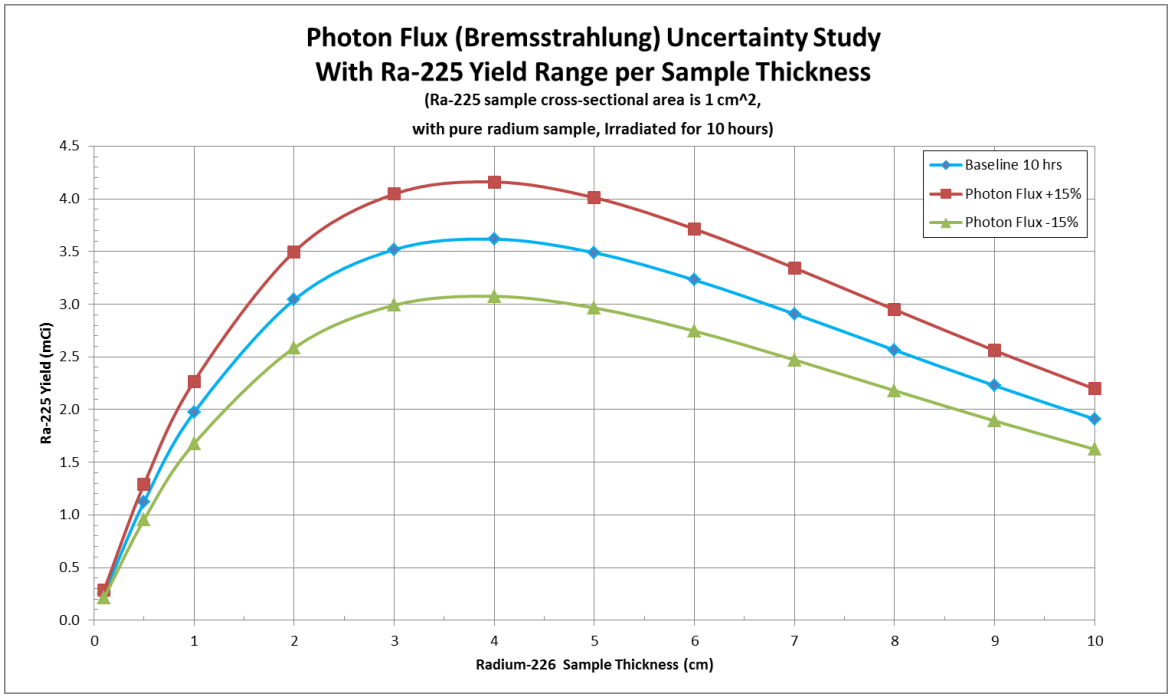

Figure 31 Bremsstrahlung Uncertainty Study
Photon Flux uncertainty study, considering a +/-15% uncertainty to the 40% Bremsstrahlung efficiency.

Since there are no error ranges reported with the TENDL cross-section data, an arbitrary uncertainty range of +/-50% was applied to the TENDL Ra-226 photo-neutron cross-section data to account for the over-predictions of TENDL data as compared to ENDF data (discussed in section 4.2). This broad uncertainty band can also be used to account for the slight differences associated with the MATLAB® curve fitting model. The uncertainty to yield relationship for cross-section is also linear, hence the arbitrary +50% uncertainty equates to a model prediction of +50% yield increase. This yield error band is in relation to the baseline parameter study, and shown in Figure 32 below.

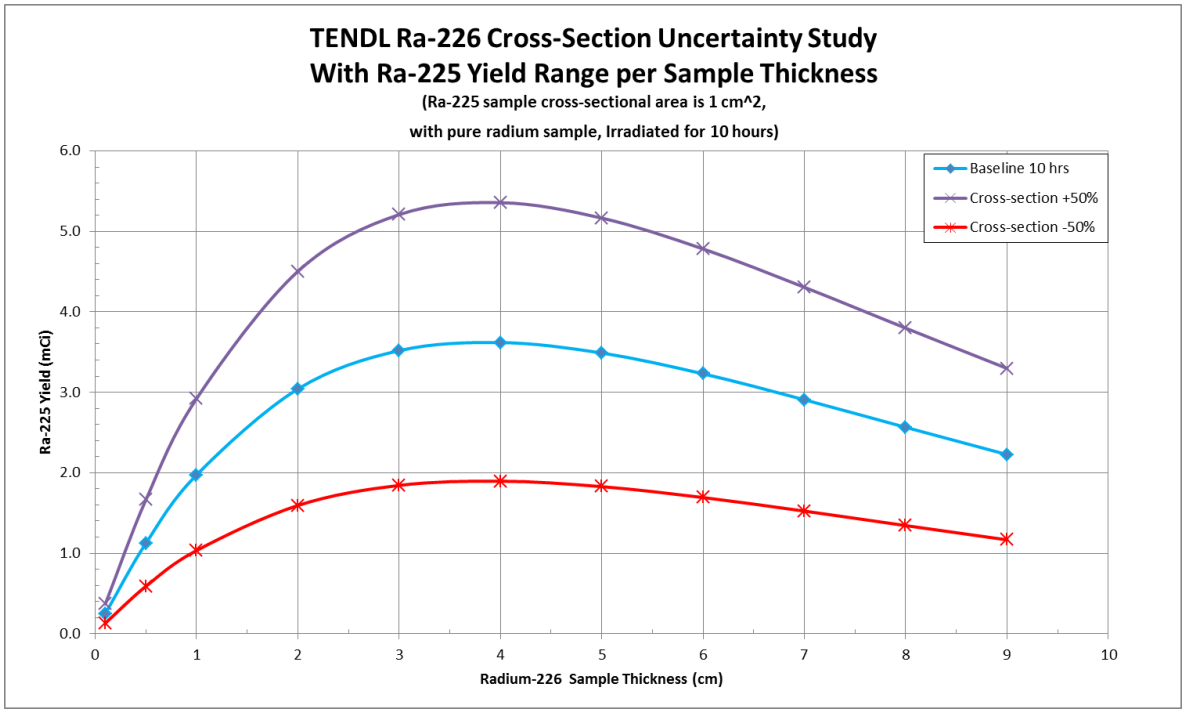

Figure 32 Ra-226 Cross-Section Uncertainty Study
Ra-225 yield study of arbitrarily uncertainty limits applied to TENDL Ra-226 photo-neutron cross-section data.

Figure 33 below shows the yield model results with uncertainty limits applied to each parameter, further expanding upon the thickness to yield study presented in Figure 29. The upper and lower bounds of yield uncertainty range (in relation to the baseline curve) are shown for the combination of parameter uncertainties with targets from 0.1 to 10 cm thick.

With a 10 hour irradiation time using an 18 MeV Varian LINAC, and with the sample located as depicted in figure 30 (above), the following yield results were calculated.

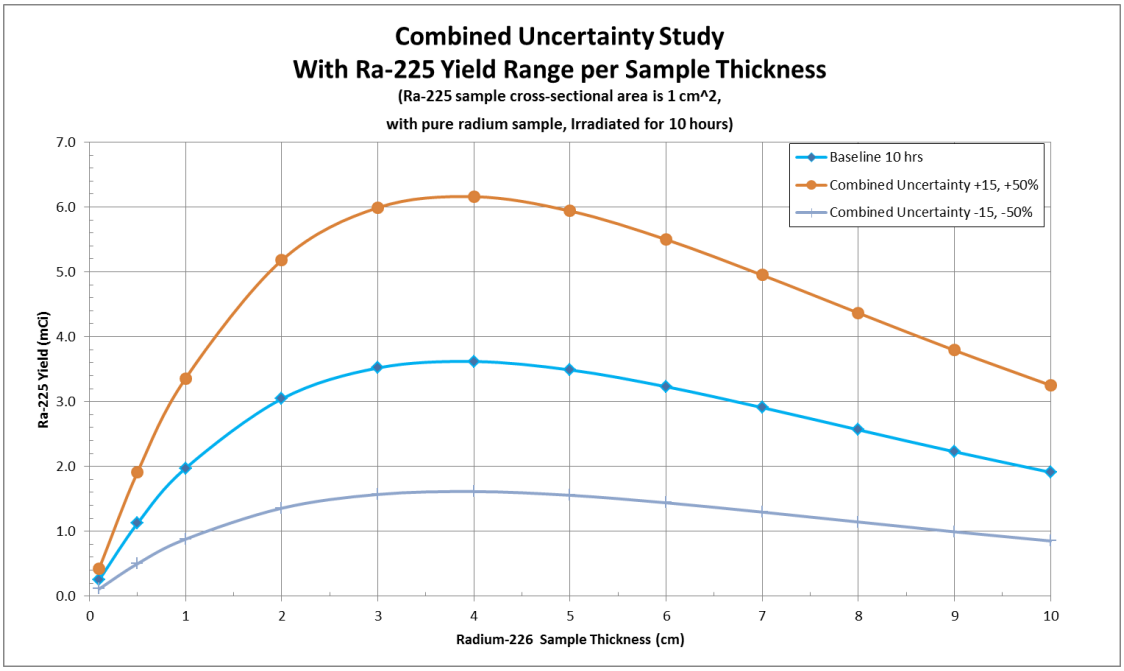

Figure 33 Combined Parameter Uncertainties
Ra-225 yield study considering arbitrary uncertainty limits assigned to yield equation parameters, photon flux and cross-section.

For comparative purposes, if a 1 cm^3 sample (1 cm thick) is irradiated for only 1 hour (as discussed in Scenario 2), the yield range resulting from the combined parameter uncertainties is 0.336 to 0.088 mCi/hr, with the baseline yielding 0.197 mCi. This range is still well below the 1.45 mCi/hr as reported by Melville. In an effort to force the model to yield the same 1.45 mCi/hr as Melville's C++ model, a 400% increase would need to be applied to the baseline photon flux data (see Figure 7 for baseline amount).

A sensitivity analysis was also performed to determine which parameter affects the yield the most by applying a +/-15% uncertainty to each baseline parameter. It was found that a +/-15% adjustment in the photon flux data and cross-section data correspond to a ~+/-15% variation in Ra-225 yield. The baseline conditions were set to a 1 hr irradiation time, and thickness set to the optimal 4 cm (20 Ci sample). With these conditions the sample thickness was also varied by +/- 15% of the nominal 4 cm to determine yield effects. In this case however, only a ~1.5% reduction in yield was observed. Concluding that minor variation in sample thickness would not appreciably affect the yield outcome.

A MATLAB® calculation was also performed using the same Bi-209 cross-section model as presented by Melville, in an effort to determine if the yield of 1.45 mCi/hr can be matched.

This calculation used the same photon flux data as was reported by Melville in the photon spectrum plot (Figure 7). However, a yield of only 0.35 mCi/hr was predicted, which is 76% less than 1.45 mCi/hr.

7.6 Scenario Conclusions

The Ra-225 yields calculated with this model are optimistic, given the assumption that all photons above 6.4 MeV would be incident upon the radium sample. This would most likely not be the case unless a specially prepared circular sample size was located at the interface of the tungsten LINAC target. Another loss not considered here is the separation efficiency of Ac-225 from the Ra-226 sample. It is unclear at this time how efficient the separation process will be, however, if it were 80% efficient, this would translate to a 20% reduction in the predicted yield values..

The photon attenuation study performed in section 6.2, along with the yield calculations just presented, shows that the main optimization to consider is sample thickness, if much larger thicknesses are used. It is also important to realize that the atom densities of the radium compounds $RaBr_2$ and $RaCl_2$ were not considered in the calculations of this chapter, to maintain a one to one comparison with Melville's model. In reality pure radium would probably not be used, so radium compound samples would need to be made slightly thicker to maintain the same attenuation characteristics and hence offer the same yield.

A parametric uncertainty study was also performed with the yield equation parameters to evaluate how a set of error limits affects the predicted yield. It was found that the yield changes linearly as the uncertainty of photon flux data and cross-section data change. Since the yield is directly proportional to these two variables in the yield equation for a given thickness. However, the predicted yield changes non-linearly with thickness, but it was found that small variations is sample thickness have little effect on the yield near the nominal 4 cm thickness.

Finally, a number of MATLAB® iterations were performed to show a relationship between increased LINAC parameters and predicted yields, where a doubling effect in three LINAC parameters (electron beam pulse current, pulse frequency, and pulse length) would equate to a potential factor of 8 increase applied to the yield. Once LINAC beam current

enhancements are fully explored, the scenario presented in Figure 33 could potentially provide a quick yield estimate, given the specified scenario parameters.

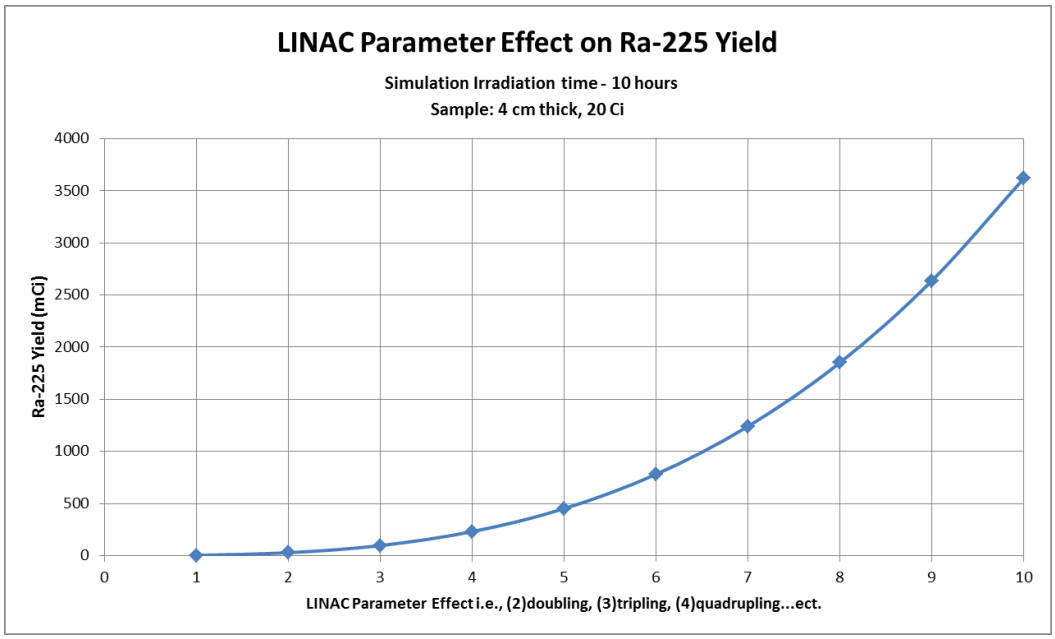

Figure 34 Scenario 4 LINAC Parameter Effect on Ra-225 Yield
A 10 hour irradiation of a 20 Ci, 4 cm thick Sample placed in photon an 18 MeV photon spectrum. This shows a predicted yield from a doubling, tripling and so forth of the three LINAC beam parameters (pulse frequency, pulse length, pulse current).

Table 9 LINAC Parameter Factors

LINAC Parameter Factor (Powers)	Ra-225 Yield (mCi)	Number of times yield is increased
1	3.6182	1
2	28.9456	8
3	97.6914	27
4	231.5648	64
5	452.2750	125
6	781.5312	216
7	1241.0426	343
8	1852.5184	512
9	2637.6678	729
10	3618.2000	1000

Table 9 shows the actual multiple that would be applied to the photon flux (hence yield) given a doubling or tripling effect of three LINAC parameters. For example the quadrupling effect of the three LINAC parameters would equate to the photon flux increasing by 64 times.

8. Future Objectives

8.1. LINAC proposal

The following general setup would be desired to achieve the most effective and efficient Ac-225 production system. First a Ra-226 sample should be designed that not only is sized for the LINAC beam, but additionally sized to maximize the photo-nuclear reaction. Next, one should determine the most efficient LINAC parameters that are within the bounds of what current LINAC technology is capable of providing. It is uncertain at this time what potential there is for modifying a LINAC electron beam, e.g., increasing the electron beam pulse frequency by a factor of 10, or increasing the pulse length. Increasing the average beam current is what is desired, therefore, a pulsed electron beam must be enhanced to approach a continuous beam flux of electrons. A 25 MeV LINAC would be chosen with an increase in its power to the limits of what is feasible. It may be advantageous to either irradiate multiple samples simultaneously on an array of LINACs or use two or three LINACs with their photon beams coinciding on one radium sample through an iso-center.

The tungsten target within the LINAC head would also need to be optimized for thickness to maximize the Bremsstrahlung output at maximum electron beam energy. Cooling of the tungsten target is also of high importance, and a thermal analysis should be performed. Due to the simplicity of the desired photon field for this production method, many of the parts and functionality present on most medical LINACS could be done away with. These parts include the primary collimator, flattening filter, or any other multi-leaf collimators (MLCs) for beam shaping and control, thereby greatly simplifying the design and minimizing cost.

Depending on the LINAC setup, it would also be desired to construct a proper localized shield that would absorb the vast majority of gamma and neutron radiation, in the immediate vicinity of the site of irradiation. The photons below the neutron separation threshold energy will have little effect on the sample and will simply be absorbed, scattered, or passed through and be absorbed in the surrounding shielding material. Localized shielding such as lead and boron coatings could be used to absorb the radiation leaving the sample area: the lead to shield a certain percentage of gamma rays and the boron coating to absorb photo-neutrons.

The cooling of the tungsten target used to produce Bremsstrahlung is another important area that requires further examination. A large portion of the electron beam energy that is not given up as Bremsstrahlung is transferred to the tungsten target in the form of heat. A thermal analysis is required if higher power LINACs with higher average beam currents are used. This would need to be done by the LINAC manufacturer.

8.2. Radium Sample Parameters

At this time the sample parameters such as type of compound (radium bromide or radium chloride), atom density, and sample dimensions are yet to be determined. It is assumed that if a collection of old radium sources such as radium needles are initially utilized, the only way to know how much is being irradiated would be to obtain a measured activity. If a significant amount of old radium sources do become available, it may be advantageous to recover the radium compounds from their sealed capsules, reforming them into desired target shapes. If radium material is eventually extracted from uranium mines, it would already be in raw form making it easier to manufacture a desired target size.

Similar to the thermal analysis of the LINAC tungsten target, the Ra-226 target will also require a thermal analysis, to determine if the radium sample composition can withstand the heat generated by a significant increase in photon flux. If it is determined there is significant heat build-up in the radium target, a cooling system to dissipate that heat should be explored. The radium target will most likely consist of a radium compound encapsulated in a metal sealed case to prevent leakage, and made strong enough to not rupture as internal gas pressures increase over long irradiations. This gas build-up should be evaluated over varying irradiation times, to ensure capsule integrity is maintained.

8.3. Experiments to Perform

The purpose of future experiments will be to validate the MATLAB® yield model and, in particular, the Ra-226 photo-neutron cross-sections, as well as to explore the potential yield increases by varying sample location. The quickest approach for performing experiments would most likely be to find a medical facility with a high energy LINAC (15 MeV or higher) that would be willing to render it for experimental use. There are also a number of Labs with high energy continuous photon sources that should also be explored. If

possible, a number of radium sources should be obtained, preferably Ra-Be (neutron generator) sources because these have significantly more radium per source as Table 5 indicates. It may also be beneficial to find a medical research group that is in the process of advancing their work with targeted alpha therapy like Actinium Pharmaceuticals Inc. [6], so experiments can be coordinated with them, so the Ac-225 is not wasted in decay.

- The first series of experiments should study the yields produced to verify Ra-226 photo-neutron cross-sections. It may even be desirable to conduct actual cross-section experiments.
- Further experiments should examine the effects of varying irradiation times on sample yield in addition to studying the doubling effect of a LINAC's electron beam parameters to see if the actual yields match the model whose values were also doubled. Finally, a sample thickness experiment should be conducted to also validate the photon attenuation estimates of the model.

8.4. Cost Benefit Analysis

Before this production method can be proposed, a cost benefit analysis must be made. The confirmatory experiments that validate the yield model should provide a high degree of certainty of this production method's feasibility in supplying significant quantities of Ac-225. At this time however, it is uncertain what is or is not an appreciable quantity, so this will need to be gained from the medical community. Therefore, in the process of determining if this method will be cost effective, a source of radium must first be established. The cost of obtaining old radium sources and the cost involved in extracting new radium from uranium mines should both be assessed. There will also be a cost associated with sample preparation, and the Ac-225 chemical separation process from the radium target.

9. Conclusions

A MATLAB® model was successfully created for calculating Ac-225 yield estimates. Even though a lower limit for an appreciable quantity of Ac-225 is not known, it is felt that this LINAC production method has enough versatility to vary the production amounts in the low mCi range. Variability is achieved in part from adjustable irradiation times, along with more variability yet to be realized as LINAC parameters are explored. Findings from future irradiation experiments using an optimized sample location and sample thickness, will aid in the development of a high-power LINAC to maximize yield. If found later that one LINAC is not sufficient in producing enough Ac-225 for the demand, a new LINAC arrangement can be designed to focus several LINAC photons beams onto one sample, or an array of LINACs can be used to irradiate multiple samples.

Ra-225 yields were simulated using TENDL Ra-226 cross-section data, along with photon attenuation considerations. A significant reduction in yield was observed from this model as compared to similar models discussed in Melville's work. A parametric study of estimated model uncertainties provides a predicted yield range that can be used with future experiments to help determine the accuracy of the model. Again, it is important to realize that the yield results presented herein still uncertain until experimental data can be obtained to evaluate Ra-226 photo-neutron cross-sections. Separation inefficiencies and losses due to sample location within the photon beam are not accounted for in these predictive models. To further this research, and confirm predicted yields a series of experiments will be the next step for model validation.

References

[1] G. Melville, "Production of Ac-225 for Cancer Therapy by Photon Induced Transmutation of Ra-226," UWS, Sydney, Australia, 2007.

[2] G. Melville, H. Mariarty, P. Metcalfe, T. Knittel and B. J. Allen, "Production of Ac-225 for cancer therapy by photon-induced transmutation of Ra-226," *Applied Radiation and Isotopes*, vol. 65, no. 9, pp. 1014-1022, 2007.

[3] G. Melville, S. F. Lui and B. J. Allen, "A theoretical model for the produciton of Ac-225 for cancer therapy by photon-induced transmutation of Ra-226," *Applied Radiation and Isotopes*, vol. 64, no. 9, pp. 979-988, 2006.

[4] INL, "Medical Actinium for Theraputic Treatment (MATT)," [Online]. Available: http://www.inl.gov/factsheets/docs/matt.pdf. [Accessed 12 February 2013].

[5] J. W. Krueger, "Oak Ridge DOE Presentation, U-233 Disposition Program Updated," 11 April 2012. [Online]. Available: http://www.oakridge.doe.gov/em/ssab/Minutes/FY2012/Presentations/SSABPresentation4-11-12.pdf. [Accessed 2 March 2013].

[6] Actinium Pharmaceuticals, "Actinium Pharmaceuticals," Actinium Pharmaceuticals, Inc., 17 July 2012. [Online]. Available: http://www.actiniumpharmaceuticals.com/investors.html. [Accessed 17 July 2013].

[7] J. R. Lamarsh and A. J. Baratta, Introduction to Nuclear Engineering, 3rd Ed, Upper Saddle River, NJ: Prentice-Hall, Inc., 2001.

[8] J. E. Turner, Atoms, Radiation, and Radiation Protection, Oak Ridge, TN: WILEY-VCH, 2007.

[9] A. Sonzogni, "Chart of Nuclides NNDC," Brookhaven National Laboratory, November 2012. [Online]. Available: http://www.nndc.bnl.gov/chart/. [Accessed 2 April 2013].

[10] D. Lawless, "Pediatric Oncology Enducation Materials," Varian, 2008. [Online]. Available: http://www.pedsoncologyeducation.com/RadiotherapyBasicsWhatisXRT.asp. [Accessed 2 April 2013].

[11] W. Strydom and W. Parker, "Electron Beams: Physical and Clinical Aspects," *Department of Medical Physics Chapter 8*, pp. 273 - 299.

[12] E. Hayward, *Photonuclear Reactions*, Washington, D.C.: Nationa Bureau of Standards Monograph 118, 1970.

[13] W. Scharf, Particle Accelerators, Applications in Technology and Research, Tauton, Somerset, England: Research Studies Press LTD., 1989.

[14] NIST, "X-Ray Mass Attenuation Coefficients," National Institute of Standards and Technology, [Online]. Available: http://physics.nist.gov/PhysRefData/XrayMassCoef/ElemTab/z88.html. [Accessed 1 May 2013].

[15] E. G. Fuller and E. Hayward, Photonuclear Reactions, Benchmark Papers in Nuclear Physics, National Bureau of Standards: Dowden, Hutchinson & Ross, Inc., 1976.

[16] D. Sheikh-Bagheri and D. W. Rogers, "Monte Carlo calculation of nine megavoltage photon beam spectra using the BEAM code," *Medical Physics,* vol. 29, no. 3, pp. 391-402, 2002.

[17] D. Sheikh-Bagheri and D. W. Rogers, "Sensitivity of megavoltage photon beam Monte Carlo simulations to electron beam and other parameters," *Medical Physics,* vol. 29, no. 3, pp. 379-390, 2002.

[18] V. Zerkin, "Experimental Nuclear Reaction Data (EXFOR)," IAEA, 28 March 2013. [Online]. Available: http://www-nds.iaea.org/exfor/exfor.htm. [Accessed 5 January 2013].

[19] V. V. Varlamov, "Centre For Photonuclear Experiments Data," Lomonosov Moscow State University, 2003. [Online]. Available: http://cdfe.sinp.msu.ru/. [Accessed 10 February 2013].

[20] A. J. Koning and D. Rochman, "TENDL-2012," NRG, Petten, 11 January 2013. [Online]. Available: ftp://ftp.nrg.eu/pub/www/talys/tendl2012/tendl2012.html. [Accessed 15 February 2013].

[21] IAEA, "Handbook on photonucleardata for applications Cross-sections and spectra," IAEA, VIENNA, 2000.

[22] A. Koning, S. Hilaire and S. Goriely, TALYS 1.4, A Nuclear Reaction Program User Manual, Petten, The Netherlands: Nuclear Research and Consultancy Group (NRG), 2011.

[23] WIKIPEDIA Foundation, "Radium Bromide," Wikipedia, 27 February 2013. [Online]. Available: http://en.wikipedia.org/wiki/Radium_bromide. [Accessed 18 March 2013].

[24] EIA, "Domestic Uranium Production Report," US Energy Information Administration, 9 May 2012. [Online]. Available: http://www.eia.gov/uranium/production/annual/. [Accessed 8 Feb 2013].

[25] EPA, "Radiation Protection," US Environmental Protection Agency, 8 July 2011. [Online]. Available: http://www.epa.gov/radiation/docs/radwaste/402-k-94-001-umt.html. [Accessed 8 March 2013].

[26] J. M. Watson, "Uranium," USGS, 12 January 2013. [Online]. Available: http://pubs.usgs.gov/of/2004/1050/uranium.htm. [Accessed 18 March 2013].

[27] Program Office of Federal and State Materials , "United States Nuclear Regulatory Commission," [Online]. Available: http://nrc-stp.ornl.gov/narmtoolbox/radium%20faq102008.pdf. [Accessed 2 March 2013].

[28] IAEA, "AQ-19 Analytical Methodology for the Determination of Radium Isotopes in Environmental Samples," International Atomic Energy Agency, VIENNA, 2010.

[29] IAEA, "IAEA-TECDOC-886 Conditioning and interim storage of spent radium sources," The IAEA, Austria, 1996.

[30] I. A. E. Agency, "IAEA-TECDOC-886 Conditioning and interim storage of spent radium sources," The IAEA, Austria, 1996.

[31] IAEA, "IAEA-TECDOC-1403 The long term stabilization of uranium mill tailings," International Atomic Energy Agency, Austria, 2004.

[32] P. Diehl, "Wise Uranium Project," 18 May 2011. [Online]. Available: http://www.wise-uranium.org/uwai.html#TAILHAZ. [Accessed 5 April 2013].

[33] Energy Information Administration, "2011 Domestic Uranium Production Report," U.S. Energy Information Administration, Washington D.C., 2012.

[34] R. A. Frietas Jr., "Nano Medicine Book Site," Landes Bioscience, 1999. [Online]. Available: http://www.nanomedicine.com/NMI/8.5.1.htm. [Accessed 2 April 2013].

[35] N. T. Khai and et al., "Monte-Carlo Calculations for Neutron Yield from photonuclear reaction Following Bremsstrahlung in Tungsten Target," *Physics of Particles in Nuclei Letters,* vol. 7, no. 1, pp. 17 - 20, 2010.

[36] M. G. Davydov, "Calculation of Photo Nuclear Reaction Yields," *Atomic Energy,* vol. 77, no. 2, pp. 641 - 645, 1994.

[37] B. S. Ishkhanov and V. V. Varlamov, "Photonuclear Reactions: Modern Status of the Data," *Physics of Atomic Nuclei,* vol. 67, no. 9, pp. 1664-1673, 2004.

[38] H. J. Hubbell and M. S. Seltzer, "Physical Measurement Laboratory," NIST, 9 December 2011. [Online]. Available: http://physics.nist.gov/PhysRefData/XrayMassCoef/ElemTab/z82.html. [Accessed 2 April 2013].

[39] G. F. Knoll, Radiation Detection and Measurement, 4th ed, Hoboken, NJ: John Wiley & Sons, Inc., 2010.

[40] F. H. Attix, INTRODUCTION TO RADIOLOGICAL PHYSICS AND RADIATION DOSIMETRY, Madison, WI: John Wiley & Sons, 1986.

[41] H. R. Vega-Carrillo, S. A. Martinez-Ovalle, A. M. Lallena, G. A. Mercado and J. L. Benites-Rengifo, "Neutron and photon spectra in LINACs," *Applied Radiation and Isotopes,* vol. 71, pp. 75-80, 2012.

[42] H. R. Vega-Carrillo and A. Baltazar-Raigosa, "Photoneutron spectra around an 18 MV LINAC," *Journal of Radioanalytical and Nuclear Chemistry,* vol. 287, pp. 323-327, 2011.

[43] G. Tosi, S. Agosteo and et al., "Monte Carlo simulations of neutron transport in a linac radiotherapy room," *Nuclear Instruments and Methods in Physics Research,* vol. B72, pp. 84-90, 1992.

[44] K. Van Laere and W. Mondelaers, "DESIGN OF FIELD FLATTENING FILTERS FOR A HIGH-POWER BREMSSTRAHLUNG CONVERTER BY FULL MONTE CARLO SIMULATION," *Radiation Physics and Chemistry,* vol. 49, no. 3, pp. 307-317, 1997.

[45] R. Mohan and C. Chui, "Energy and angular distributions of photons from medical linear accelerators," *Medical Physics,* vol. 12, no. 5, pp. 592-597, 1985.

[46] G. Tosi, A. Torresin and et al. , "Neutron measurements around medical electron accelerators by active and passive detection techniques," *Medical Physics,* vol. 18, no. 1, pp. 54-60, 1991.

[47] A. Mesbahi and et al, "Monte Carlo calculation of Varian 2300C/D Linac photon beam characteristics: a comparison between MCNP4C, GEANT3 and measurements," *Applied Radiation and Isotopes,* vol. 62, pp. 469-477, 2005.

[48] B. Juste, R. Miro and et al, "Uncertainty and sensitivity analysis of the effect of the mean energy and FWHM of the initial electron fluence on the Bremsstrahlung photon spectra of linear accelerators," *Applied Radiation and Isotopes,* vol. 70, pp. 1267-1271, 2012.

[49] F. Rahmani and M. Shahriari, "Hybrid photonuclear source optimization for electron accelerator-based BNCT," *Nuclear Instruments and Methods in Physics Research A,* vol. 618, pp. 48-53, 2010.

[50] X. Mao, K. Kase and W. Nelson, "SLAC-PUB-6628 Giant Dipole Resonance Neutron

Yields Produced By Electrons As A Function Of Target Material And Thickness," Stanford Linear Accelerator Center, Stanford, 1996.

[51] M. Miederer, D. Scheinberg and M. McDevitt, "Realizing the potential of the Actinium-225 radionuclide generator in targeted alpha particle therapy applications," *Advanced Drug Delivery Reviews,* vol. 60, pp. 1371-1382, 2008.

[52] R. Boll, D. Malkemus and S. Mirzadeh, "Production of actinium-225 for alpha particle mediated radioimmunotherapy," *Applied Radiation and Isotopes,* vol. 62, pp. 667-679, 2005.

[53] F. Ruddy and et al, "Separation of the alpha-emitting radioisotopes actinium-225 and bismuth-213 from thorium-229 using alpha recoil methods," *Nuclear Instruments and Methods in Physics Research B,* vol. 213, pp. 351-356, 2004.

[54] K. J. Shultis and R. E. Faw, Radiation Shielding, La Grande Park, IL: Prentice-Hall, Inc., 2000.

[55] Federation of American Scientists, "Processes and Characteristics of Major Isotopes Handled at Mound," 2013. [Online]. Available: http://www.fas.org/nuke/space/mound.pdf. [Accessed 1 May 2013].

[56] J. A. Seibert and J. M. Boone, "X-Ray Imaging Physics for Nuclear Medicine Technology. Part 2: X-Ray Interactions and Image Formations," *Journal of Nuclear Med Technology,* vol. 33, pp. 3 - 18, 2005.

[57] A. Ma, "Monte Carlo study of photoneutron production in the Varian Clinac 2100C linac," *Journal of Radioanalytical and Nuclear Chemistry,* vol. 276, no. 1, pp. 119-123, 2008.

Appendix A – Summary of Equations and Examples

Transient Decay Time of Ra-225 to Maximum Activity of Ac-225

$$t = \frac{1}{\lambda_2 - \lambda_1} \cdot \ln \frac{\lambda_2}{\lambda_1}$$

$\lambda_1 = 5.456 \times 10^{-7} s^{-1}$, $^{225}_{88}Ra$ (Decay constant)

$\lambda_2 = 8.021 \times 10^{-7} s^{-1}$, $^{225}_{89}Ac$ (Decay constant)

$$t = \frac{1}{8.021 \times 10^{-7} - 5.456 \times 10^{-7}} \cdot \ln \frac{8.021 \times 10^{-7}}{5.456 \times 10^{-7}}$$

$$t = 1{,}499{,}461\ seconds\ or\ 17.35\ days$$

Number of Atoms in a given Sample

The number of atoms **n** in a given sample can be calculated by knowing its activity **α** and half-life $\mathbf{T_{1/2}}$:

$$n = \frac{\alpha}{\left(\ln 2 / T_{1/2}\right)} = \frac{\alpha}{\lambda}, \qquad number\ of\ atoms$$

Example calculation for the number of atoms in a 15 mCi sample of Ra-226.

$$\alpha = 15\ mCi = 15\ mCi \cdot \left(\frac{3.7 \times 10^7\ dis/s}{1 mCi}\right)$$

$$\alpha = 5.55 \times 10^8 \frac{disintegrations}{sec}\ or\ 555\ MBq$$

$$\lambda = \frac{\ln 2}{T_{1/2}} = \frac{0.693}{1600 yr} \cdot \left(\frac{1 yr}{3.156 \times 10^7 s}\right) = 1.372 \times 10^{-11} s^{-1}$$

$$n = \frac{5.55 \times 10^8}{1.372 \times 10^{-11} s^{-1}} = 4.045 \times 10^{19}\ atoms$$

Atom Density of Radium Compounds

The two most common forms of radium are produced as radium-bromide $RaBr_2$ and radium-chloride $RaCl_2$. The following is a sample calculation of the atom density for each:

Atom density of the i^{th} isotope in the mixture,

$$N_i = \frac{(w_i)(\rho_{mix})(N_A)}{M_i}$$

Weight percent of the i^{th} isotope in the mixture,

$$w_i = \frac{M_{Ra}}{M_{Ra} + 2 \cdot M_{Br}}$$

Calculate the weight percent of Ra-226 in $RaBr_2$.

$$w_{Ra/Br} = \frac{M_{Ra}}{M_{Ra} + 2 \cdot M_{Br}} = \frac{226\,{}^{g}/_{mol}}{226\,{}^{g}/_{mol} + 2 \cdot 79.9\,{}^{g}/_{mol}} = 0.5858$$

$$N_{Ra/Br} = \frac{\left(w_{Ra/Br}\right)\left(\rho_{RaBr_2}\,{}^{g}/_{cm^3}\right)\left(0.6022 \times 10^{24}\,atoms/_{mol}\right)}{M_{Ra}\,{}^{g}/_{mol}}$$

$$N_{Ra/Br} = \frac{(0.5858)\left(5.79\,{}^{g}/_{cm^3}\right)\left(0.6022 \times 10^{24}\,atoms/_{mol}\right)}{226\,{}^{g}/_{mol}}$$

$$N_{Ra/Br} = 9.037 \times 10^{21}\ atoms/_{cm^3}$$

The calculation for the atom density of Ra-226 in $RaCl_2$ is similar and yields the following:

$$N_{Ra/Cl} = 1.128 \times 10^{22}\ atoms/_{cm^3}$$

Table 10 Radium Compound Properties

Radium Compounds and their Properties					
	Radium	Bromine	Chlorine	RaBr2	RaCl2
Density (g/cm3)				5.79	4.9
GAW (g/mol)	226	79.9	35.4	386	296.1

Weight Percent of Ra in RaBr2	0.5858
Weight Percent of Ra in RaBr2	0.8646
Ra 226 Atom Density in RaBr2	9.0377E+21
Ra 226 Atom Density in RaCl2	1.1288E+22
Percent increase in atom density that RaCl2 has over RaBr2	20

As can be seen by Table 10 above, there is a 20% increase in the atom density with a radium-chloride compound versus radium-bromide. This indicates that a LINAC-based production method may prove more efficient if radium samples are produced in the form of $RaCl_2$.

Sample Volume of Radium Compounds

Volume of a $RaBr_2$ sample, given a radium source activity:

$$\alpha = 15\ mCi$$

$$N_{Ra/Br} = 9.037 \times 10^{21}\ {}^{atoms}/_{cm^3}$$

$$\lambda = 1.372 \times 10^{-11} s^{-1}$$

$$V = \frac{\alpha \cdot \left(\frac{3.7 \times 10^7\ dis/s}{1mCi}\right)}{(1.372 \times 10^{-11} s^{-1}) \cdot N_{Ra/Br}}$$

$$V = \frac{15\ mCi \cdot \left(\frac{3.7 \times 10^7\ dis/s}{1mCi}\right)}{(1.372 \times 10^{-11} s^{-1}) \cdot 9.037 \times 10^{21}\ {}^{atoms}/_{cm^3}} = 4.476 \times 10^{-3} cm^3$$

Validation of MATLAB® Model Results

The following calculation will be used to demonstrate functionality of the MATLAB® model code. It will confirm the correct output in Ra-225 yield rate from scenario 2 shown in Figure 27 in section 7. An example calculation will be performed using the

yield equation discussed in section 2.3 that includes a photon attenuation correction term. The curve fitting functions, their parameters, and model criteria will be used in these calculations to show validity to this particular model.

Curve Fitting Functions – Using a Modified Weibull Distribution

The following modified Weibull Distribution used for curve fitting both photon rate data and cross-section data, was provided by MATLABs curve fitting tutorial. While the equation coefficients P_1, P_2, and P_3, represent curve shifting along the x-axis, shape parameter, and amplitude adjustments, respectively.

Photon Rate (photons/s): Function was Evaluated at *E = 12 MeV*

$$\phi(E) = P_3 \cdot \left(\frac{E}{P_1}\right)^{(P_2+1)} \cdot e^{-\left(\frac{E}{P_1}\right)^{P_2}}$$

Where the MATLAB calculated function coefficients are,

$P_1 = 0.8615$
$P_2 = 0.7026$
$P_3 = 1.8208$

$$\phi(12) = 1.8208 \cdot \left(\frac{12}{0.8615}\right)^{(0.7026+1)} \cdot e^{-\left(\frac{12}{0.8615}\right)^{0.7026}} = 2.78 \times 10^{11}\, photons/_s$$

$$\boxed{\phi(12) = 2.78 \times 10^{11}\, photons/_s}$$

See Figure 6, indicating agreement between this value and the accelerator data.

Photo-neutron Cross-section (mb): Function was Evaluated at *E = 12 MeV*

$$\sigma(E) = \left[C_3 \cdot \left(\frac{E}{C_1}\right)^{(C_2+2)} \cdot e^{-\left(\frac{E}{C_1}\right)^{C_2}}\right] + 13$$

Where the MATLAB calculated function coefficients are,

$C_1 = 11.6998$
$C_2 = 7.1417$
$C_3 = 657.7149$

$$\sigma(12) = \left[657.7149 \cdot \left(\frac{12}{11.6998}\right)^{(7.1417+2)} \cdot e^{-\left(\frac{12}{11.6998}\right)^{7.1417}}\right] + 13$$

$$\sigma(12) = 263.14\ mb = 2.6314 \times 10^{-25} cm^2$$

See Figure 15, indicating agreement between this value and the TENDL Ra-226 photo-neutron cross-section data.

Yield Rate Model Validation

Ra-225 Atom Rate Yield (atoms/s): Function was Evaluated at *E = 12 MeV*

$$Y(E) = \left(N_{pure} \cdot t\right) \cdot \sigma(E) \cdot \ \phi(E) \cdot \left(e^{-(0.0068E + 0.1855)}\right)$$

Where the yield equation parameters are,

N_{Pure} = 1.33 x 10^{22} atoms/cm^3	*Atom Density*
t = 1 cm	*Sample Thickness*

$$Y(E) = 7.45 \times 10^{8}\ {}^{atoms}/_{s}$$

This example validates both curve fitting plots for photon rate data and cross-section data, shown in Figures 6 and 15, respectively. The Ra-225 yield rate value calculated above validates scenario 2 curve in Figure 27. This process therefore gives a high degree of certainty, that the remaining calculations performed by this MATLAB® program are also valid, by producing expected results.

Appendix B – Nuclide Decay Mode and Separation Energy

Figure 35 Decay Modes
For nuclides residing between Bi-209 and Th-232, Public Domain [9].

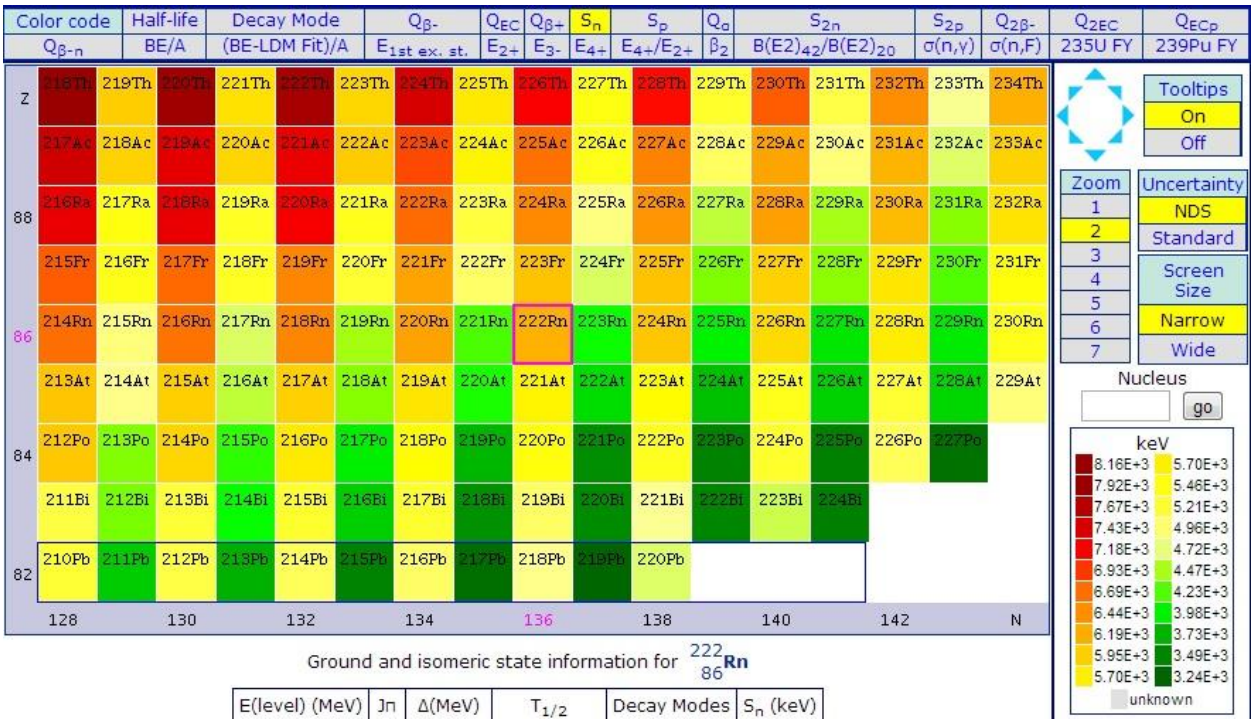

Figure 36 Single Neutron Separation Energy
For nuclides residing between Bi-209 and Th-232, Public Domain [9].

Appendix C – Photo-neutron Yield Equation Usage

Source 1: *W H Scharf, "Particle Accelerators Applied in Technology and Research", Research Studies Press Ltd., 1989. Pg 164.* [13].

This source expresses the *yield W* of a neutron reaction as the probability of a neutron being emitted from the target under the influence of a bombarding particle.

For thin targets *yield W* is given by

$$W = N \cdot \sigma_n \cdot (E_k) \cdot d$$

Where, E_k – incident Particle Energy
σ_n – given reaction cross-section
d – target thickness
N – atom density of target material

It mentions the advantage of thin targets is that they can generate neutrons with a small energy distribution.

For thick targets the incident particle can be completely stopped until they have zero energy, hence the *yield* W_g for thick targets is given by

$$W_g = \int_0^{E_k} N d\sigma_n \cdot (E_k)\,(dE)$$

It further demonstrates the use of this equation in calculating the total neutron yield for a number of different reactions to include photo-neutron reactions. It also discussed the electron-to-bremsstrahlung neutron yield produced in tungsten and uranium targets of large thicknesses on the order of a few millimeters. For this method of neutron production an incident electron beam of energy greater than 30 MeV can attain a high neutron flux.

Source 2: *Everett G Fuller, E Hayward. " Photonuclear Reactions, Benchmark Papers in Nuclear Physics", Edited by. Dowden, Hutchinson & Ross Inc. Vol. 2. pg 84-85, 1976* [12].

This book includes a research paper that uses a similar equation to *source 1* for neutron yield. They used this equation in a number of experiments to calculate photo-neutron yield curves for various elements. Samples were irradiated by photons emitted from a betatron target, where the betatron beam was 18 MeV, and the sample was situated 30 feet from the betatron target. The paper mentions that before the curves can be analyzed for photo-neutron cross-section, a correction factor is needed to account for the absorption of bremsstrahlung photons in

the sample. It indicates that 'small' samples are typically used in residual activity experiments so this correction factor is negligible. However, to obtain a significant neutron flux with the sample located 30 feet from the photon source, a much larger sample was used. The photon absorption in the larger sample was no longer negligible; hence, the correction factor was applied by the following equation [12]:

$$\frac{\alpha' A}{\rho a l} = N \int_0^{E_0} \sigma(E) P(E, E_0) dE \int_0^t \frac{e^{-\mu \rho t}}{l} dx,$$

The activity per mole α is,

$$\alpha = \frac{\alpha' A}{\rho a l}$$

Where, *l – sample length (cm)*
ρ – sample density (g/cm^3)
a – sample cross sectional area (cm^2)
α' – activity from sample
σ€ – reaction cross-section (mb)
P(E,E$_0$) – photons per cm^2 per 100$_\gamma$ / min per MeV interval of energy E
E$_0$ – betatron energy (MeV)
μ - total absorption coefficient (cm^2/g) or mass attenuation coefficient
N – Avogadro's number (atoms/mol)

Integrating the above equation with respect to x gives,

$$\alpha = N \int_0^{E_0} \sigma(E) P(E, E_0) \left[\frac{1 - e^{-\mu \rho l}}{\mu \rho l} \right] dE$$

This paper states that the variation in energy in the bracketed term was the calculated sample size used. The energy variation was found to be 1% over an energy range of 10 – 22 MeV. Given this low variation the bracketed term was taken outside the integral giving the basic equation for the photon difference method:

$$\frac{\alpha' A \mu}{a(1 - e^{-\mu \rho l})} = N \int_0^{E_0} \sigma(E) P(E, E_0) dE$$

This equation has now been corrected for sample size and photon absorption.

Even though the variables shown in the above equation are not of the same nomenclature as used in this research, they represent similar parameters. The term ($1 - e^{-\mu \rho l}$) is the same as ($1 - e^{-\mu t}$), where $e^{-\mu t}$ represents the fraction of un-attenuated photons normally incident through a sample thickness t. This is the fraction of photons that are not attenuated by means of Compton

scattering and pair-production, and represent the available photons for potential photo-neutron reactions. Therefore, the correction factor ($e^{-\mu t}$) will be implemented in the MATLAB® yield model to account for photon attenuation in varying radium sample thicknesses. One can additionally see the following source [35], which used the exact yield equation used in Melville's work but without the attenuation correction term. Other similar usages of this yield equation can be found in the following sources, [36], [35], [37].

Appendix D – Photon Attenuation Data

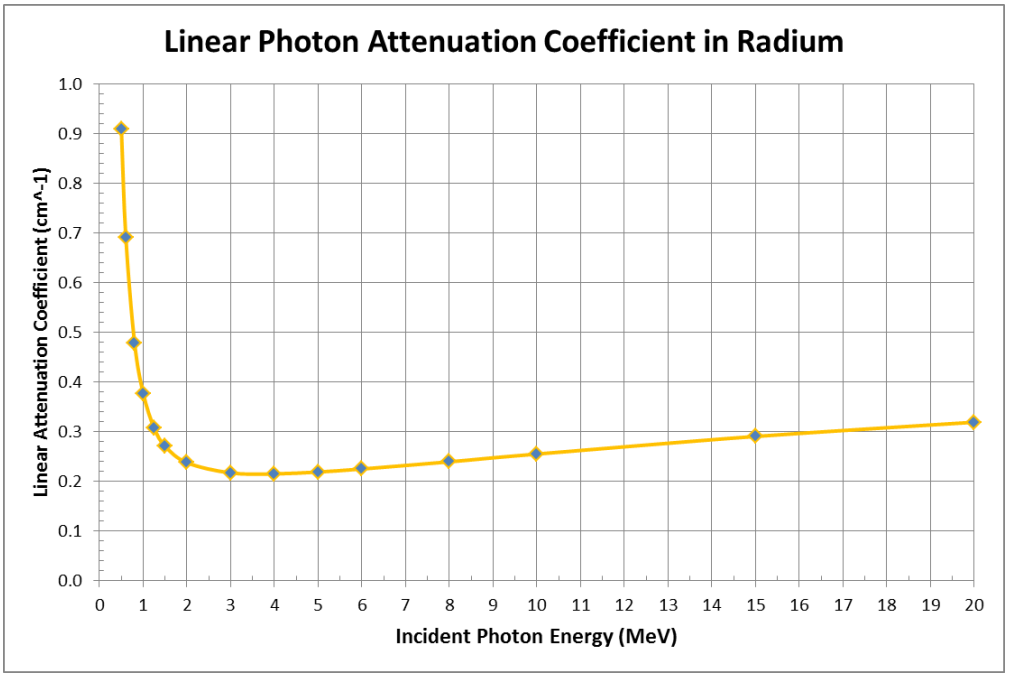

Figure 37 Photon Linear Attenuation in Radium

Table 11 Tungsten Attenuation Data
This data was adapted from, public domain [14].

Fraction of Attenuated Photons in Tungsten											
Photon Energy (MeV)	Mass Attenuation (cm2/g)	Linear Attenuation (cm-1)	Mean Free Path (cm)	Fraction of normally incident photons attenuated in Varying Tungsten Target Thicknesses (cm)							
				0.1	0.5	1	2	3	5	10	20
0.10	4.438	85.43150	0.01171	0.99981	1.00000	1.00000	1.00000	1.00000	1.00000	1.00000	1.00000
0.15	1.581	30.43425	0.03286	0.95233	1.00000	1.00000	1.00000	1.00000	1.00000	1.00000	1.00000
0.20	0.7844	15.09970	0.06623	0.77908	0.99947	1.00000	1.00000	1.00000	1.00000	1.00000	1.00000
0.30	0.3238	6.23315	0.16043	0.46384	0.95569	0.99804	1.00000	1.00000	1.00000	1.00000	1.00000
0.40	0.1925	3.70563	0.26986	0.30965	0.84320	0.97542	0.99940	0.99999	1.00000	1.00000	1.00000
0.50	0.1378	2.65265	0.37698	0.23300	0.73455	0.92954	0.99503	0.99965	1.00000	1.00000	1.00000
0.60	0.1093	2.10403	0.47528	0.18974	0.65077	0.87804	0.98512	0.99819	0.99997	1.00000	1.00000
0.80	0.08066	1.55271	0.64404	0.14382	0.53992	0.78833	0.95519	0.99052	0.99958	1.00000	1.00000
1.00	0.06618	1.27397	0.78495	0.11962	0.47111	0.72028	0.92176	0.97811	0.99829	1.00000	1.00000
1.25	0.05577	1.07357	0.93147	0.10180	0.41538	0.65821	0.88318	0.96007	0.99534	0.99998	1.00000
1.50	0.05	0.96250	1.03896	0.09176	0.38199	0.61806	0.85412	0.94428	0.99187	0.99993	1.00000
2.00	0.04433	0.85335	1.17185	0.08180	0.34733	0.57402	0.81854	0.92270	0.98597	0.99980	1.00000
3.00	0.04075	0.78444	1.27480	0.07545	0.32444	0.54362	0.79172	0.90495	0.98020	0.99961	1.00000
4.00	0.04038	0.77732	1.28648	0.07479	0.32203	0.54036	0.78873	0.90289	0.97948	0.99958	1.00000
5.00	0.04103	0.78983	1.26610	0.07594	0.32626	0.54608	0.79395	0.90647	0.98073	0.99963	1.00000
6.00	0.0421	0.81043	1.23392	0.07785	0.33316	0.55533	0.80227	0.91208	0.98261	0.99970	1.00000
8.00	0.04472	0.86086	1.16163	0.08248	0.34977	0.57720	0.82124	0.92442	0.98649	0.99982	1.00000
10.00	0.04747	0.91380	1.09433	0.08733	0.36676	0.59900	0.83920	0.93552	0.98963	0.99989	1.00000
15.00	0.05384	1.03642	0.96486	0.09845	0.40441	0.64528	0.87417	0.95537	0.99438	0.99997	1.00000
20.00	0.05893	1.13440	0.88152	0.10724	0.43289	0.67839	0.89656	0.96673	0.99656	0.99999	1.00000

Table 12 Platinum Attenuation Data

This data was adapted from, public domain [14].

Fraction of Attenuated Photons in Platinum											
Photon Energy (MeV)	Mass Attenuation (cm2/g)	Linear Attenuation (cm-1)	Mean Free Path (cm)	Fraction of normally incident photons attenuated in Varying platinum material Thicknesses (cm)							
				0.1	0.5	1	2	3	5	10	20
0.10	4.993	107.09985	0.00934	0.99998	1.00000	1.00000	1.00000	1.00000	1.00000	1.00000	1.00000
0.15	1.795	38.50275	0.02597	0.97873	1.00000	1.00000	1.00000	1.00000	1.00000	1.00000	1.00000
0.20	0.8896	19.08192	0.05241	0.85165	0.99993	1.00000	1.00000	1.00000	1.00000	1.00000	1.00000
0.30	0.3625	7.77563	0.12861	0.54048	0.97951	0.99958	1.00000	1.00000	1.00000	1.00000	1.00000
0.40	0.2118	4.54311	0.22011	0.36511	0.89685	0.98936	0.99989	1.00000	1.00000	1.00000	1.00000
0.50	0.1492	3.20034	0.31247	0.27388	0.79814	0.95925	0.99834	0.99993	1.00000	1.00000	1.00000
0.60	0.1168	2.50536	0.39914	0.22162	0.71426	0.91835	0.99333	0.99946	1.00000	1.00000	1.00000
0.80	0.08456	1.81381	0.55133	0.16588	0.59623	0.83697	0.97342	0.99567	0.99988	1.00000	1.00000
1.00	0.06857	1.47083	0.67989	0.13678	0.52069	0.77026	0.94722	0.98787	0.99936	1.00000	1.00000
1.25	0.05727	1.22844	0.81404	0.11560	0.45894	0.70725	0.91430	0.97491	0.99785	1.00000	1.00000
1.50	0.05112	1.09652	0.91197	0.10385	0.42205	0.66597	0.88842	0.96273	0.99584	0.99998	1.00000
2.00	0.04522	0.96997	1.03096	0.09244	0.38429	0.62091	0.85629	0.94552	0.99217	0.99994	1.00000
3.00	0.0416	0.89232	1.12067	0.08537	0.35992	0.59030	0.83214	0.93123	0.98846	0.99987	1.00000
4.00	0.04124	0.88460	1.13046	0.08466	0.35744	0.58712	0.82953	0.92962	0.98800	0.99986	1.00000
5.00	0.04196	0.90004	1.11106	0.08607	0.36239	0.59345	0.83471	0.93280	0.98889	0.99988	1.00000
6.00	0.0431	0.92450	1.08167	0.08830	0.37013	0.60327	0.84260	0.93756	0.99017	0.99990	1.00000
8.00	0.04584	0.98327	1.01702	0.09365	0.38837	0.62591	0.86006	0.94765	0.99267	0.99995	1.00000
10.00	0.04872	1.04504	0.95690	0.09923	0.40698	0.64832	0.87632	0.95651	0.99462	0.99997	1.00000
15.00	0.05537	1.18769	0.84197	0.11199	0.44780	0.69507	0.90702	0.97165	0.99736	0.99999	1.00000
20.00	0.06064	1.30073	0.76880	0.12197	0.47814	0.72767	0.92583	0.97980	0.99850	1.00000	1.00000

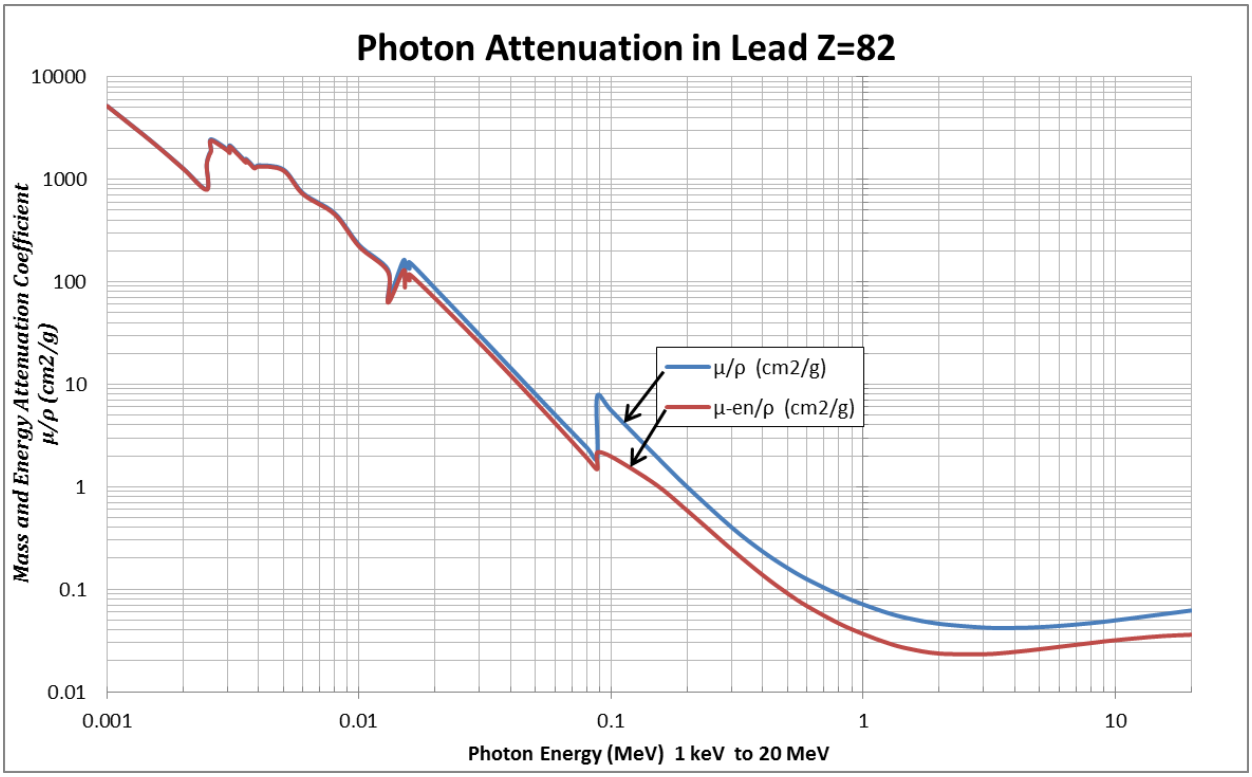

Figure 38 Mass and Energy Attenuation of Photons in Lead

Mass and Energy Attenuation of Photons in Lead. This plot was generation from tabulated data, Adapted by [38].

Appendix E – Microsoft Excel Data

Table 13 MATLAB® Photon and Cross-section Data

This data was imported into MATLAB® to be curve fitted for a yield model. The Ra-226 cross-section data was obtained from TENDL [20], while the following photon spectrum data was interpolated from the Melville's plot for the Varian 18 MeV medical LINAC used in the experiments [1].

Energy (MeV)	Photon Rate (photons/s) x10^12	Incident Gamma Energy (MeV)	Ra 226 X-section (mb)
0.01	1E-15	6.4	18.1536
0.25	0.87	7.0	27.3839
0.50	2.12	8.0	41.7100
0.75	2.65	9.0	66.6047
0.90	3.05	10.0	113.6840
1.20	3.20	11.0	206.8700
1.40	3.15	12.0	278.2610
1.80	3.10	13.0	207.8580
2.40	2.50	14.0	104.1750
2.65	2.25	15.0	46.2876
3.00	2.00	16.0	21.0588
4.40	1.50	17.0	10.9147
5.00	1.25	18.0	6.5794
6.00	1.00		
6.40	0.93		
7.50	0.75		
9.00	0.50		
11.40	0.36		
13.20	0.25		
18.00	1E-15		

Appendix F - MATLAB® Code Instructions

For proper utilization of the program model, a number of criteria must be met.

1. The photon spectrum data must be entered into the appropriate Microsoft Excel worksheet.
2. Photon data must be in the Unit of photons/s.
3. Cross-section data must be entered into the appropriate Microsoft Excel worksheet.
4. Cross-section data must be in the Units of (mb).
5. This program uses functions to automatically import data from specific Microsoft Excel files, worksheets, and cells within that file.
6. The Microsoft Excel files that this program imports from must be located in the same directory as the m.file. This will allow the code to compile and import properly.
7. Once imported and compiled, there are a number of trial and error adjustments to the curve fitting model that should be made to obtain a better fit. These details are discussed within the code documentation.
8. It will be most helpful for the next researcher to view the code, read the documentation, compare the Microsoft Excel data files to the code to see how they interact and simply understand what is happening in the code.
9. Once an understanding of the code is established, its use for yield calculation will be apparent.